Blanton, Michael R. and Bershady, Matthew A. and Abolfathi, Bela and Albareti, Franco D. and Prieto, Carlos Allende and Almeida, Andres and Alonso-García, Javier and Anders, Friedrich and Anderson, Scott F. and Andrews, Brett and Aquino-Ortíz, Erik and Aragón-Salamanca, Alfonso and Argudo-Fernandez, Maria and Armengaud, Eric and Aubourg, Eric and Avila-Reese, Vladimir and Badenes, Carles and Bailey, Stephen and Barger, Kathleen A. and Barrera-Ballesteros, Jorge and Bartosz, Curtis and Bates, Dominic and Baumgarten, Falk and Bautista, Julian and Beaton, Rachael and Beers, Timothy C. and Belfiore, Francesco and Bender, Chad F. and Berlind, Andreas A. and Bernardi, Mariangela and Beutler, Florian and Bird, Jonathan C. and Bizyaev, Dmitry and Blanc, Guillermo A. and Blomqvist, Michael and Bolton, Adam S. and Boquien, Médéric and Borissova, Jura and van den Bosch, Remco and Bovy, Jo and Brandt, William N. and Brinkmann, Jonathan and Brownstein, Joel R. and Bundy, Kevin and Burgasser, Adam J. and Burtin, Etienne and Busca, Nicolás G. and Cappellari, Michele and Carigi, Maria Leticia Delgado and Carlberg, Joleen K. and Rosell, Aurelio Carnero and Carrera, Ricardo and Chanover, Nancy J. and Cherinka, Brian and Cheung, Edmond and Chew, Yilen Gómez Maqueo and Chiappini, Cristina and Choi, Peter Doohyun and Chojnowski, Drew and Chuang, Chia-Hsun and Chung, Haeun and Cirolini, Rafael Fernando and Clerc, Nicolas

and Cohen, Roger E. and Comparat, Johan and Costa, Luiz da and Cousinou, Marie-Claude and Covey, Kevin and Crane, Jeffrey D. and Croft, Rupert A.C. and Cruz-Gonzalez, Irene and Cuadra, Daniel Garrido and Cunha, Katia and Damke, Guillermo J. and Darling, Jeremy and Davies, Roger and Dawson, Kyle and Macorra, Axel de la and Dell'Agli, Flavia and De Lee, Nathan and Delubac, Timothée and Di Mille, Francesco and Diamond-Stanic, Aleksandar M. and Cano-Díaz, Mariana and Donor, John and Downes, Juan José and Drory, Niv and Bourboux, Hélion du Mas des and Duckworth, Christopher J. and Dwelly, Tom and Dyer, Jamie and Ebelke, Garrett and Eigenbrot, Arthur D. and Eisenstein, Daniel J. and Emsellem, Eric and Eracleous, Mike and Escoffier, Stephanie and Evans, Michael L. and Fan, Xiaohui and Fernández-Alvar, Emma and Fernandez-Trincado, J.G. and Feuillet, Diane K. and Finoguenov, Alexis and Fleming, Scott W. and Font-Ribera, Andreu and Fredrickson, Alexander and Freischlad, Gordon and Frinchaboy, Peter M. and Fuentes, Carla E. and Galbany, Lluís and Garcia-Dias, R. and García-Hernández, D.A. and Gaulme, Patrick and Geisler, Doug and Gelfand, Joseph D. and Gil-Marín, Héctor and Gillespie, Bruce A. and Goddard, Daniel and Gonzalez-Perez, Violeta and Grabowski, Kathleen and Green, Paul J. and Grier, Catherine J. and Gunn, James E. and Guo, Hong and Guy, Julien and Hagen, Alex and Hahn, ChangHoon and Hall, Matthew and Harding, Paul and Hasselquist, Sten and Hawley, Suzanne L. and Hearty, Fred and Hernández, Jonay I. Gonzalez and Ho, Shirley and Hogg, David W. and Holley-Bockelmann, Kelly and Holtzman, Jon A. and Holzer, Parker H. and Huehnerhoff, Joseph and

Hutchinson, Timothy A. and Hwang, Ho Seong and Ibarra-Medel, Héctor J. and Ilha, Gabriele da Silva and Ivans, Inese I. and Ivory, KeShawn and Jackson, Kelly and Jensen, Trey W. and Johnson, Jennifer A. and Jones, Amy and Jönsson, Henrik and Jullo, Eric and Kamble, Vikrant and Kinemuchi, Karen and Kirkby, David and Kitaura, Francisco-Shu and Klaene, Mark and Knapp, Gillian R. and Kneib, Jean-Paul and Kollmeier, Juna A. and Lacerna, Ivan and Lane, Richard R. and Lang, Dustin and Law, David R. and Lazarz, Daniel and Lee, Youngbae and Goff, Jean-Marc Le and Liang, Fu-Heng and Li, Cheng and Li, Hongyu and Lian, Jianhui and Lima, Marcos and Lin, Lihwai and Lin, Yen-Ting and Lis, Sara Bertran de and Liu, Chao and Lizaola, Miguel Angel C. de Icaza and Long, Dan and Lucatello, Sara and Lundgren, Britt and MacDonald, Nicholas K. and Machado, Alice Deconto and MacLeod, Chelsea L. and Mahadevan, Suvrath and Maia, Marcio Antonio Geimba and Maiolino, Roberto and Majewski, Steven R. and Malanushenko, Elena and Malanushenko, Viktor and Manchado, Arturo and Mao, Shude and Maraston, Claudia and Marques-Chaves, Rui and Masseron, Thomas and Masters, Karen L. and McBride, Cameron K. and McDermid, Richard M. and McGrath, Brianne and McGreer, Ian D. and Medina Peña, Nicolás and Melendez, Matthew and Merloni, Andrea and Merrifield, Michael R. and Meszaros, Szabolcs and Meza, Andres and Minchev, Ivan and Minniti, Dante and Miyaji, Takamitsu and More, Surhud and Mulchaey, John and Müller-Sánchez, Francisco and Muna, Demitri and Munoz, Ricardo R. and Myers, Adam D. and Nair, Preethi and Nandra, Kirpal and Nascimento, Janaina Correa do and Negrete, Alenka and Ness, Melissa and

Newman, Jeffrey A. and Nichol, Robert C. and Nidever, David L. and Nitschelm, Christian and Ntelis, Pierros and O'Connell, Julia E. and Oelkers, Ryan J. and Oravetz, Audrey and Oravetz, Daniel and Pace, Zach and Padilla, Nelson and Palanque-Delabrouille, Nathalie and Palicio, Pedro Alonso and Pan, Kaike and Parejko, John K. and Parikh, Taniya and Pâris, Isabelle and Park, Changbom and Patten, Alim Y. and Peirani, Sebastien and Pellejero-Ibanez, Marcos and Penny, Samantha and Percival, Will J. and Perez-Fournon, Ismael and Petitjean, Patrick and Pieri, Matthew M. and Pinsonneault, Marc and Pisani, Alice and Poleski, Radosław and Prada, Francisco and Prakash, Abhishek and Queiroz, Anna Bárbara de Andrade and Raddick, M. Jordan and Raichoor, Anand and Rembold, Sandro Barboza and Richstein, Hannah and Riffel, Rogemar A. and Riffel, Rogério and Rix, Hans-Walter and Robin, Annie C. and Rockosi, Constance M. and Rodríguez-Torres, Sergio and Roman-Lopes, A. and Román-Zúñiga, Carlos and Rosado, Margarita and Ross, Ashley J. and Rossi, Graziano and Ruan, John and Ruggeri, Rossana and Rykoff, Eli S. and Salazar-Albornoz, Salvador and Salvato, Mara and Sánchez, Ariel G. and Aguado, D.S. and Sánchez-Gallego, José R. and Santana, Felipe A. and Santiago, Basílio Xavier and Sayres, Conor and Schiavon, Ricardo P. and Schimoia, Jaderson da Silva and Schlafly, Edward F. and Schlegel, David J. and Schneider, Donald P. and Schultheis, Mathias and Schuster, William J. and Schwope, Axel and Seo, Hee-Jong and Shao, Zhengyi and Shen, Shiyin and Shetrone, Matthew and Shull, Michael and Simon, Joshua D. and Skinner, Danielle and Skrutskie, M.F. and Slosar, Anže and Smith, Verne V. and Sobeck,

Jennifer S. and Sobreira, Flavia and Somers, Garrett and Souto, Diogo and Stark, David V. and Stassun, Keivan and Stauffer, Fritz and Steinmetz, Matthias and Storchi-Bergmann, Thaisa and Streblyanska, Alina and Stringfellow, Guy S. and Suárez, Genaro and Sun, Jing and Suzuki, Nao and Szigeti, Laszlo and Taghizadeh-Popp, Manuchehr and Tang, Baitian and Tao, Charling and Tayar, Jamie and Tembe, Mita and Teske, Johanna and Thakar, Aniruddha R. and Thomas, Daniel and Thompson, Benjamin A. and Tinker, Jeremy L. and Tissera, Patricia and Tojeiro, Rita and Toledo, Hector Hernandez and Torre, Sylvain de la and Tremonti, Christy and Troup, Nicholas W. and Valenzuela, Octavio and Valpuesta, Inma Martinez and Vargas-González, Jaime and Vargas-Magaña, Mariana and Vazquez, Jose Alberto and Villanova, Sandro and Vivek, M. and Vogt, Nicole and Wake, David and Walterbos, Rene and Wang, Yuting and Weaver, Benjamin Alan and Weijmans, Anne-Marie and Weinberg, David H. and Westfall, Kyle B. and Whelan, David G. and Wild, Vivienne and Wilson, John and Wood-Vasey, W.lM. and Wylezalek, Dominika and Xiao, Ting and Yan, Renbin and Yang, Meng and Ybarra, Jason E. and Yèche, Christophe and Zakamska, Nadia and Zamora, Olga and Zarrouk, Pauline and Zasowski, Gail and Zhang, Kai and Zhao, Gong-Bo and Zheng, Zheng and Zheng, Zheng and Zhou, Xu and Zhou, Zhi-Min and Zhu, Guangtun B. and Zoccali, Manuela and Zou, Hu (2017) Sloan Digital Sky Survey IV: mapping the Milky Way, nearby galaxies, and the distant universe. Astronomical Journal, 154 (1). 28/1-28/35. ISSN 1538-3881

Access from the University of Nottingham repository:

Sloan Digital Sky Survey IV: Mapping the Milky Way, Nearby Galaxies, and the Distant Universe

Michael R. Blanton[1], Matthew A. Bershady[2], Bela Abolfathi[3], Franco D. Albareti[4,5,123], Carlos Allende Prieto[6,7], Andres Almeida[8], Javier Alonso-García[9,10], Friedrich Anders[11], Scott F. Anderson[12], Brett Andrews[13], Erik Aquino-Ortíz[14], Alfonso Aragón-Salamanca[15], Maria Argudo-Fernández[9], Eric Armengaud[16], Eric Aubourg[17], Vladimir Avila-Reese[14], Carles Badenes[13], Stephen Bailey[18], Kathleen A. Barger[19], Jorge Barrera-Ballesteros[20], Curtis Bartosz[12], Dominic Bates[21], Falk Baumgarten[11,22], Julian Bautista[23], Rachael Beaton[24], Timothy C. Beers[25], Francesco Belfiore[26,27], Chad F. Bender[28], Andreas A. Berlind[29], Mariangela Bernardi[30], Florian Beutler[31], Jonathan C. Bird[29], Dmitry Bizyaev[32,33], Guillermo A. Blanc[24], Michael Blomqvist[34], Adam S. Bolton[23,35], Médéric Boquien[9], Jura Borissova[10,36], Remco van den Bosch[37], Jo Bovy[38,39,124], William N. Brandt[40,41,42], Jonathan Brinkmann[32], Joel R. Brownstein[23], Kevin Bundy[43,44], Adam J. Burgasser[45], Etienne Burtin[16], Nicolás G. Busca[17], Michele Cappellari[46], Maria Leticia Delgado Carigi[14], Joleen K. Carlberg[47,48,49], Aurelio Carnero Rosell[50,51], Ricardo Carrera[6,7], Nancy J. Chanover[52], Brian Cherinka[20], Edmond Cheung[43], Yilen Gómez Maqueo Chew[14], Cristina Chiappini[11], Peter Doohyun Choi[53], Drew Chojnowski[52], Chia-Hsun Chuang[11], Haeun Chung[54], Rafael Fernando Cirolini[50,55], Nicolas Clerc[56], Roger E. Cohen[57], Johan Comparat[4,56], Luiz da Costa[50,51], Marie-Claude Cousinou[58], Kevin Covey[59], Jeffrey D. Crane[24], Rupert A. C. Croft[60], Irene Cruz-Gonzalez[14], Daniel Garrido Cuadra[8], Katia Cunha[28,51], Guillermo J. Damke[8,61], Jeremy Darling[62], Roger Davies[46], Kyle Dawson[23], Axel de la Macorra[63], Flavia Dell'Agli[6,7], Nathan De Lee[64], Timothée Delubac[65], Francesco Di Mille[66], Aleks Diamond-Stanic[2,67], Mariana Cano-Díaz[68], John Donor[19], Juan José Downes[69], Niv Drory[70], Hélion du Mas des Bourboux[16], Christopher J. Duckworth[21], Tom Dwelly[56], Jamie Dyer[23], Garrett Ebelke[61], Arthur D. Eigenbrot[2], Daniel J. Eisenstein[71], Eric Emsellem[72,73], Mike Eracleous[41], Stephanie Escoffier[58], Michael L. Evans[12], Xiaohui Fan[28], Emma Fernández-Alvar[14], J. G. Fernandez-Trincado[74], Diane K. Feuillet[37], Alexis Finoguenov[56], Scott W. Fleming[47,75], Andreu Font-Ribera[18,76], Alexander Fredrickson[32], Gordon Freischlad[32], Peter M. Frinchaboy[19], Carla E. Fuentes[57], Lluís Galbany[13], R. Garcia-Dias[6,7], D. A. García-Hernández[6,7], Patrick Gaulme[32], Doug Geisler[57], Joseph D. Gelfand[1,77], Héctor Gil-Marín[78,79], Bruce A. Gillespie[32,80], Daniel Goddard[31], Violeta Gonzalez-Perez[31], Kathleen Grabowski[32], Paul J. Green[71], Catherine J. Grier[40,41], James E. Gunn[81], Hong Guo[82], Julien Guy[79], Alex Hagen[41], ChangHoon Hahn[1], Matthew Hall[61], Paul Harding[83], Sten Hasselquist[52], Suzanne L. Hawley[12], Fred Hearty[40], Jonay I. Gonzalez Hernández[6,7], Shirley Ho[18,60,84], David W. Hogg[1], Kelly Holley-Bockelmann[29], Jon A. Holtzman[52], Parker H. Holzer[23], Joseph Huehnerhoff[12], Timothy A. Hutchinson[23], Ho Seong Hwang[54], Héctor J. Ibarra-Medel[14], Gabriele da Silva Ilha[50,55], Inese I. Ivans[23], KeShawn Ivory[19,85], Kelly Jackson[19], Trey W. Jensen[1,23], Jennifer A. Johnson[86,87], Amy Jones[88], Henrik Jönsson[6,7], Eric Jullo[34], Vikrant Kamble[23], Karen Kinemuchi[32], David Kirkby[3], Francisco-Shu Kitaura[6,7], Mark Klaene[32], Gillian R. Knapp[81], Jean-Paul Kneib[34,65], Juna A. Kollmeier[24], Ivan Lacerna[89,90,91], Richard R. Lane[89], Dustin Lang[38,39], David R. Law[47], Daniel Lazarz[92], Youngbae Lee[53], Jean-Marc Le Goff[16], Fu-Heng Liang[93], Cheng Li[82,93], Hongyu Li[94], Jianhui Lian[31], Marcos Lima[50,95], Lihwai Lin[96], Yen-Ting Lin[96], Sara Bertran de Lis[6,7], Chao Liu[94], Miguel Angel C. de Icaza Lizaola[14], Dan Long[32], Sara Lucatello[97], Britt Lundgren[98], Nicholas K. MacDonald[12], Alice Deconto Machado[50,55], Chelsea L. MacLeod[71], Suvrath Mahadevan[40], Marcio Antonio Geimba Maia[50,51], Roberto Maiolino[26,27], Steven R. Majewski[61], Elena Malanushenko[32], Viktor Malanushenko[32], Arturo Manchado[6,7], Shude Mao[93,94,99], Claudia Maraston[31], Rui Marques-Chaves[6,7], Thomas Masseron[6,7], Karen L. Masters[31], Cameron K. McBride[71], Richard M. McDermid[100,101,125], Brianne McGrath[19], Ian D. McGreer[28], Nicolás Medina Peña[36], Matthew Melendez[19], Andrea Merloni[56], Michael R. Merrifield[15], Szabolcs Meszaros[102,126], Andres Meza[90], Ivan Minchev[11], Dante Minniti[10,90,103], Takamitsu Miyaji[104], Surhud More[43], John Mulchaey[24], Francisco Müller-Sánchez[62], Demitri Muna[86], Ricardo R. Munoz[105], Adam D. Myers[106], Preethi Nair[107], Kirpal Nandra[56], Janaina Correa do Nascimento[50,108], Alenka Negrete[14], Melissa Ness[37], Jeffrey A. Newman[13], Robert C. Nichol[31], David L. Nidever[35], Christian Nitschelm[9], Pierros Ntelis[17], Julia E. O'Connell[19], Ryan J. Oelkers[29], Audrey Oravetz[32], Daniel Oravetz[32], Zach Pace[2], Nelson Padilla[89], Nathalie Palanque-Delabrouille[16], Pedro Alonso Palicio[6,7], Kaike Pan[32], John K. Parejko[12], Taniya Parikh[31], Isabelle Pâris[34], Changbom Park[54], Alim Y. Patten[12], Sebastien Peirani[43,109], Marcos Pellejero-Ibanez[6,7], Samantha Penny[31], Will J. Percival[31], Ismael Perez-Fournon[6,7], Patrick Petitjean[109], Matthew M. Pieri[34], Marc Pinsonneault[86], Alice Pisani[58,109], Radosław Poleski[86], Francisco Prada[4,5], Abhishek Prakash[13], Anna Bárbara de Andrade Queiroz[50,108], M. Jordan Raddick[20], Anand Raichoor[16,65], Sandro Barboza Rembold[50,55], Hannah Richstein[19], Rogemar A. Riffel[50,55], Rogério Riffel[50,108], Hans-Walter Rix[37], Annie C. Robin[74], Constance M. Rockosi[44,110], Sergio Rodríguez-Torres[4,5,111], A. Roman-Lopes[8], Carlos Román-Zúñiga[104], Margarita Rosado[14], Ashley J. Ross[87], Graziano Rossi[53], John Ruan[12], Rossana Ruggeri[31], Eli S. Rykoff[112,113], Salvador Salazar-Albornoz[56], Mara Salvato[56], Ariel G. Sánchez[56], D. S. Aguado[6,7], José R. Sánchez-Gallego[12], Felipe A. Santana[105], Basílio Xavier Santiago[50,108], Conor Sayres[12], Ricardo P. Schiavon[114], Jaderson da Silva Schimoia[50,108], Edward F. Schlafly[18,127], David J. Schlegel[18], Donald P. Schneider[40,41], Mathias Schultheis[115], William J. Schuster[104], Axel Schwope[11], Hee-Jong Seo[116], Zhengyi Shao[82], Shiyin Shen[82], Matthew Shetrone[117], Michael Shull[62], Joshua D. Simon[25], Danielle Skinner[12], M. F. Skrutskie[61],

Anže Slosar[118], Verne V. Smith[35], Jennifer S. Sobeck[61], Flavia Sobreira[50,119], Garrett Somers[29], Diogo Souto[51], David V. Stark[43], Keivan Stassun[29], Fritz Stauffer[32], Matthias Steinmetz[11], Thaisa Storchi-Bergmann[50,108], Alina Streblyanska[6,7], Guy S. Stringfellow[62], Genaro Suárez[104], Jing Sun[19], Nao Suzuki[43], Laszlo Szigeti[102], Manuchehr Taghizadeh-Popp[20], Baitian Tang[57], Charling Tao[58,93], Jamie Tayar[86], Mita Tembe[61], Johanna Teske[24,128], Aniruddha R. Thakar[20], Daniel Thomas[31], Benjamin A. Thompson[19], Jeremy L. Tinker[1], Patricia Tissera[90], Rita Tojeiro[21], Hector Hernandez Toledo[14], Sylvain de la Torre[34], Christy Tremonti[2], Nicholas W. Troup[61], Octavio Valenzuela[14], Inma Martinez Valpuesta[6,7], Jaime Vargas-González[8], Mariana Vargas-Magaña[63], Jose Alberto Vazquez[118], Sandro Villanova[57], M. Vivek[23], Nicole Vogt[52], David Wake[98,120], Rene Walterbos[52], Yuting Wang[94], Benjamin Alan Weaver[1,35], Anne-Marie Weijmans[21], David H. Weinberg[86,87], Kyle B. Westfall[31,110], David G. Whelan[121], Vivienne Wild[21], John Wilson[61], W. M. Wood-Vasey[13], Dominika Wylezalek[20], Ting Xiao[82], Renbin Yan[92], Meng Yang[21], Jason E. Ybarra[104,122], Christophe Yèche[16], Nadia Zakamska[20], Olga Zamora[6,7], Pauline Zarrouk[16], Gail Zasowski[23,47,80], Kai Zhang[92], Gong-Bo Zhao[94], Zheng Zheng[94], Zheng Zheng[23], Xu Zhou[94], Zhi-Min Zhou[94], Guangtun B. Zhu[80,127], Manuela Zoccali[10,89], and Hu Zou[94]

[1] Center for Cosmology and Particle Physics, Department of Physics, New York University, 4 Washington Place, New York, NY 10003, USA
[2] Department of Astronomy, University of Wisconsin-Madison, 475 N. Charter St., Madison, WI 53726, USA
[3] Department of Physics and Astronomy, University of California, Irvine, Irvine, CA 92697, USA
[4] Instituto de Física Teórica (IFT) UAM/CSIC, Universidad Autónoma de Madrid, Cantoblanco, E-28049 Madrid, Spain
[5] Campus of International Excellence UAM+CSIC, Cantoblanco, E-28049 Madrid, Spain
[6] Instituto de Astrofísica de Canarias, E-38205 La Laguna, Tenerife, Spain
[7] Departamento de Astrofísica, Universidad de La Laguna (ULL), E-38206 La Laguna, Tenerife, Spain
[8] Departamento de Física, Facultad de Ciencias, Universidad de La Serena, Cisternas 1200, La Serena, Chile
[9] Unidad de Astronomía, Fac. Cs. Básicas, Universidad de Antofagasta, Avda. U. de Antofagasta 02800, Antofagasta, Chile
[10] Instituto Milenio de Astrofísica, Av. Vicuña Mackenna 4860, Macul, Santiago, Chile
[11] Leibniz-Institut für Astrophysik Potsdam (AIP), An der Sternwarte 16, D-14482 Potsdam, Germany
[12] Department of Astronomy, Box 351580, University of Washington, Seattle, WA 98195, USA
[13] PITT PACC, Department of Physics and Astronomy, University of Pittsburgh, Pittsburgh, PA 15260, USA
[14] Instituto de Astronomía, Universidad Nacional Autónoma de México, A.P. 70-264, 04510, México, D.F., México
[15] School of Physics & Astronomy, University of Nottingham, Nottingham, NG7 2RD, UK
[16] CEA, Centre de Saclay, IRFU, F-91191, Gif-sur-Yvette, France
[17] APC, University of Paris Diderot, CNRS/IN2P3, CEA/IRFU, Observatoire de Paris, Sorbonne Paris Cite, France
[18] Lawrence Berkeley National Laboratory, 1 Cyclotron Road, Berkeley, CA 94720, USA
[19] Department of Physics and Astronomy, Texas Christian University, Fort Worth, TX 76129, USA
[20] Center for Astrophysical Sciences, Department of Physics and Astronomy, Johns Hopkins University, 3400 North Charles Street, Baltimore, MD 21218, USA
[21] School of Physics and Astronomy, University of St. Andrews, North Haugh, St. Andrews, KY16 9SS, UK
[22] Humboldt-Universität zu Berlin, Institut für Physik, Newtonstrasse 15, D-12589, Berlin, Germany
[23] Department of Physics and Astronomy, University of Utah, 115 S. 1400 E., Salt Lake City, UT 84112, USA
[24] The Observatories of the Carnegie Institution for Science, 813 Santa Barbara St., Pasadena, CA 91101, USA
[25] Department of Physics and JINA Center for the Evolution of the Elements, University of Notre Dame, Notre Dame, IN 46556 USA
[26] Cavendish Laboratory, University of Cambridge, 19 J. J. Thomson Avenue, Cambridge CB3 0HE, UK
[27] Kavli Institute for Cosmology, University of Cambridge, Madingley Road, Cambridge CB3 0HA, UK
[28] Steward Observatory, The University of Arizona, 933 North Cherry Avenue, Tucson, AZ 85721-0065, USA
[29] Vanderbilt University, Department of Physics & Astronomy, 6301 Stevenson Center Ln., Nashville, TN 37235, USA
[30] Department of Physics and Astronomy, University of Pennsylvania, Philadelphia, PA 19104, USA
[31] Institute of Cosmology & Gravitation, University of Portsmouth, Dennis Sciama Building, Portsmouth, PO1 3FX, UK
[32] Apache Point Observatory, P.O. Box 59, Sunspot, NM 88349, USA
[33] Sternberg Astronomical Institute, Moscow State University, Moscow
[34] Aix Marseille Univ, CNRS, LAM, Laboratoire d'Astrophysique de Marseille, Marseille, France
[35] National Optical Astronomy Observatory, 950 North Cherry Avenue, Tucson, AZ 85719, USA
[36] Departamento de Fśica y Astronomía, Universidad de Valparaíso, Av. Gran Bretan a 1111, Playa Ancha, Casilla 5030, Valparaiso, Chile
[37] Max-Planck-Institut für Astronomie, Königstuhl 17, D-69117 Heidelberg, Germany
[38] Department of Astronomy and Astrophysics, University of Toronto, 50 St. George Street, Toronto, ON, M5S 3H4, Canada
[39] Dunlap Institute for Astronomy and Astrophysics, University of Toronto, 50 St. George Street, Toronto, Ontario M5S 3H4, Canada
[40] Department of Astronomy and Astrophysics, Eberly College of Science, The Pennsylvania State University, 525 Davey Laboratory, University Park, PA 16802, USA
[41] Institute for Gravitation and the Cosmos, The Pennsylvania State University, University Park, PA 16802, USA
[42] Department of Physics, The Pennsylvania State University, University Park, PA 16802, USA
[43] Kavli Institute for the Physics and Mathematics of the Universe, Todai Institutes for Advanced Study, the University of Tokyo, Kashiwa, 277-8583, Japan
[44] University of California Observatories, University of California, Santa Cruz, CA 95064, USA
[45] Center for Astrophysics and Space Science, University of California San Diego, La Jolla, CA 92093, USA
[46] Sub-department of Astrophysics, Department of Physics, University of Oxford, Denys Wilkinson Building, Keble Road, Oxford OX1 3RH, UK
[47] Space Telescope Science Institute, 3700 San Martin Drive, Baltimore, MD 21218, USA
[48] NASA Goddard Space Flight Center, Code 667, Greenbelt, MD 20771, USA
[49] Department of Terrestrial Magnetism, Carnegie Institution for Science, 5241 Broad Branch Road, NW, Washington, DC 20015, USA
[50] Laboratório Interinstitucional de e-Astronomia, 77 Rua General José Cristino, Rio de Janeiro, 20921-400, Brasil
[51] Observatório Nacional, Rio de Janeiro, Brazil
[52] Department of Astronomy, New Mexico State University, Box 30001, MSC 4500, Las Cruces NM 88003, USA
[53] Department of Astronomy and Space Science, Sejong University, Seoul 143-747, Korea
[54] Korea Institute for Advanced Study, 85 Hoegiro, Dongdaemun-gu, Seoul 02455, Korea

[55] Departamento de Física, CCNE, Universidade Federal de Santa Maria, 97105-900, Santa Maria, RS, Brazil
[56] Max-Planck-Institut für Extraterrestrische Physik, Gießenbachstr. 1, D-85748 Garching, Germany
[57] Department of Astronomy, Universidad de Concepción, Chile
[58] Aix Marseille Univ, CNRS/IN2P3, CPPM, Marseille, France
[59] Department of Physics and Astronomy, Western Washington University, 516 High Street, Bellingham, WA 98225, USA
[60] Department of Physics, Carnegie Mellon University, 5000 Forbes Avenue, Pittsburgh, PA 15213, USA
[61] Department of Astronomy, University of Virginia, 530 McCormick Road, Charlottesville, VA 22904-4325, USA
[62] Center for Astrophysics and Space Astronomy, Department of Astrophysical and Planetary Sciences, University of Colorado,
389 UCB, Boulder, CO 80309-0389, USA
[63] Instituto de Física, Universidad Nacional Autónoma de México, Apdo. Postal 20-364, México
[64] Department of Physics, Geology, and Engineering Tech, Northern Kentucky University, Highland Heights, KY 41099, USA
[65] Institute of Physics, Laboratory of Astrophysics, Ecole Polytechnique Fédérale de Lausanne (EPFL), Observatoire de Sauverny,
1290 Versoix, Switzerland
[66] Las Campanas Observatory, Colina El Pino Casilla 601 La Serena, Chile
[67] Department of Physics and Astronomy, Bates College, 44 Campus Avenue, Lewiston, ME 04240, USA
[68] CONACYT Research Fellow, Instituto de Astronomía, Universidad Nacional Autónoma de México,
A.P. 70-264, 04510, México, D.F., México
[69] Centro de Investigaciones de Astronomía, AP 264, Mérida 5101-A, Venezuela
[70] McDonald Observatory, The University of Texas at Austin, 1 University Station, Austin, TX 78712, USA
[71] Harvard-Smithsonian Center for Astrophysics, 60 Garden St., Cambridge, MA 02138, USA
[72] European Southern Observatory, Karl-Schwarzschild-Str. 2, D-85748 Garching, Germany
[73] Université Lyon 1, Observatoire de Lyon, Centre de Recherche Astrophysique de Lyon and Ecole Normale Supérieure de Lyon,
9 avenue Charles André, F-69230 Saint-Genis Laval, France
[74] Institut UTINAM, CNRS UMR6213, Univ. Bourgogne Franche-Comté, OSU THETA Franche-Comté-Bourgogne,
Observatoire de Besançon, BP 1615, F-25010 Besançon Cedex, France
[75] CSRA, Inc., 3700 San Martin Drive, Baltimore, MD 21218, USA
[76] Department of Physics & Astronomy, University College London, Gower Street, London, WC1E 6BT, UK
[77] NYU Abu Dhabi, P.O. Box 129188, Abu Dhabi, UAE
[78] Sorbonne Universités, Institut Lagrange de Paris (ILP), 98 bis Boulevard Arago, F-75014 Paris, France
[79] Laboratoire de Physique Nucléaire et de Hautes Energies, Université Pierre et Marie Curie, 4 Place Jussieu, F-75005 Paris, France
[80] Department of Physics and Astronomy, Johns Hopkins University, 3400 N. Charles St., Baltimore, MD 21218, USA
[81] Department of Astrophysical Sciences, Princeton University, Princeton, NJ 08544, USA
[82] Shanghai Astronomical Observatory, Chinese Academy of Science, 80 Nandan Road, Shanghai 200030, China
[83] Department of Astronomy, Case Western Reserve University, Cleveland, OH 44106, USA
[84] Berkeley Center for Cosmological Physics, UC Berkeley, Berkeley, CA 94707, USA
[85] Rice University, Department of Physics and Astronomy, 6100 Main St. MS-550, Houston, TX 77005, USA
[86] Department of Astronomy, The Ohio State University, 140 W. 18th Ave., Columbus, OH 43210, USA
[87] Center for Cosmology and AstroParticle Physics, The Ohio State University, 191 W. Woodruff Ave., Columbus, OH 43210, USA
[88] Max-Planck-Institut für Astrophysik, Karl-Schwarzschild-Str. 1, D-85748 Garching, Germany
[89] Instituto de Astrofísica, Pontificia Universidad Católica de Chile, Av. Vicuna Mackenna 4860,
782-0436 Macul, Santiago, Chile
[90] Departamento de Física, Facultad de Ciencias Exactas, Universidad Andres Bello,
Av. Fernandez Concha 700, Las Condes, Santiago, Chile
[91] Astrophysical Research Consortium, Physics/Astronomy Building, Rm C319, 3910 15th Avenue NE, Seattle, WA 98195, USA
[92] Department of Physics and Astronomy, University of Kentucky, 505 Rose St., Lexington, KY, 40506-0055, USA
[93] Tsinghua Center for Astrophysics & Department of Physics, Tsinghua University, Beijing 100084, China
[94] National Astronomical Observatories, Chinese Academy of Sciences, 20A Datun Road, Chaoyang District, Beijing 100012, China
[95] Departamento de Física Matemática, Instituto de Física, Universidade de São Paulo, CP 66318, CEP 05314-970, São Paulo, SP, Brazil
[96] Academia Sinica Institute of Astronomy and Astrophysics, P.O. Box 23-141, Taipei 10617, Taiwan
[97] Astronomical Observatory of Padova, National Institute of Astrophysics, Vicolo Osservatorio 5-35122—Padova, Italy
[98] Department of Physics, University of North Carolina Asheville, One University Heights, Asheville, NC 28804, USA
[99] Jodrell Bank Centre for Astrophysics, School of Physics and Astronomy,
The University of Manchester, Oxford Road, Manchester M13 9PL, UK
[100] Department of Physics and Astronomy, Macquarie University, Sydney NSW 2109, Australia
[101] Australian Astronomical Observatory, P.O. Box 915, Sydney NSW 1670, Australia
[102] ELTE Gothard Astrophysical Observatory, H-9704 Szombathely, Szent Imre herceg st. 112, Hungary
[103] Vatican Observatory, V00120 Vatican City State, Italy
[104] Instituto de Astronomía, Universidad Nacional Autónoma de México,
Unidad Académica en Ensenada, Ensenada BC 22860, México
[105] Universidad de Chile, Av. Libertador Bernardo O'Higgins 1058, Santiago de Chile
[106] Department of Physics and Astronomy, University of Wyoming, Laramie, WY 82071, USA
[107] University of Alabama, Tuscaloosa, AL 35487, USA
[108] Instituto de Fsica, Universidade Federal do Rio Grande do Sul, Campus do Vale, Porto Alegre,
RS, 91501-970, Brazil
[109] Université Paris 6 et CNRS, Institut dAstrophysique de Paris, 98bis blvd. Ara go, F-75014 Paris, France
[110] Department of Astronomy and Astrophysics, University of California Santa Cruz, 1156 High St., Santa Cruz, CA, 95064, USA
[111] Departamento de Fsica Teórica M8, Universidad Autonóma de Madrid (UAM), Cantoblanco, E-28049, Madrid, Spain
[112] Kavli Institute for Particle Astrophysics & Cosmology, P. O. Box 2450, Stanford University, Stanford, CA 94305, USA
[113] SLAC National Accelerator Laboratory, Menlo Park, CA 94025, USA
[114] Astrophysics Research Institute, Liverpool John Moores University, IC2,
Liverpool Science Park, 146 Brownlow Hill, Liverpool L3 5RF, UK
[115] Laboratoire Lagrange, Université Côte d'Azur, Observatoire de la Côte d'Azur, CNRS, Blvd de l'Observatoire, F-06304 Nice, France
[116] Department of Physics and Astronomy, Ohio University, Clippinger Labs, Athens, OH 45701, USA
[117] McDonald Observatory, University of Texas at Austin, 3640 Dark Sky Dr., Fort Davis, TX 79734, USA
[118] Brookhaven National Laboratory, Upton, NY 11973, USA

[119] Universidade Federal do ABC, Centro de Ciências Naturais e Humanas, Av. dos Estados, 5001, Santo André,
SP, 09210-580, Brazil
[120] Department of Physical Sciences, The Open University, Milton Keynes, MK7 6AA, UK
[121] Department of Physics, Austin College, Sherman, TX 75090, USA
[122] Department of Physics, Bridgewater College, 402 E. College St., Bridgewater, VA 22812 USA

Abstract

We describe the Sloan Digital Sky Survey IV (SDSS-IV), a project encompassing three major spectroscopic programs. The Apache Point Observatory Galactic Evolution Experiment 2 (APOGEE-2) is observing hundreds of thousands of Milky Way stars at high resolution and high signal-to-noise ratios in the near-infrared. The Mapping Nearby Galaxies at Apache Point Observatory (MaNGA) survey is obtaining spatially resolved spectroscopy for thousands of nearby galaxies (median $z \sim 0.03$). The extended Baryon Oscillation Spectroscopic Survey (eBOSS) is mapping the galaxy, quasar, and neutral gas distributions between $z \sim 0.6$ and 3.5 to constrain cosmology using baryon acoustic oscillations, redshift space distortions, and the shape of the power spectrum. Within eBOSS, we are conducting two major subprograms: the SPectroscopic IDentification of eROSITA Sources (SPIDERS), investigating X-ray AGNs and galaxies in X-ray clusters, and the Time Domain Spectroscopic Survey (TDSS), obtaining spectra of variable sources. All programs use the 2.5 m Sloan Foundation Telescope at the Apache Point Observatory; observations there began in Summer 2014. APOGEE-2 also operates a second near-infrared spectrograph at the 2.5 m du Pont Telescope at Las Campanas Observatory, with observations beginning in early 2017. Observations at both facilities are scheduled to continue through 2020. In keeping with previous SDSS policy, SDSS-IV provides regularly scheduled public data releases; the first one, Data Release 13, was made available in 2016 July.

Key words: cosmology: observations – galaxies: general – Galaxy: general – instrumentation: spectrographs – stars: general – surveys

1. Introduction

The Sloan Digital Sky Survey (SDSS; York et al. 2000) started observations in 1998 and has completed three different phases. The data collected includes optical imaging of most of the northern high Galactic latitude sky as well as optical and near-infrared spectroscopy of over 3.5 million stars, galaxies, and quasars. These observations all used the 2.5 m Sloan Foundation Telescope at Apache Point Observatory (APO; Gunn et al. 2006). This paper describes SDSS-IV, the fourth phase, and how it builds upon and extends both the infrastructure and scientific legacy of the previous generations of surveys.

1.1. The SDSS-I through SDSS-III legacy

Between 2000 April and 2005 June, as described by York et al. (2000), SDSS-I began the SDSS Legacy Survey, imaging the sky in five bandpasses (u, g, r, i, and z; Fukugita et al. 1996) using the SDSS imaging camera (Gunn et al. 1998). As part of the Legacy Survey, SDSS-I also observed spectra, mostly of galaxies and quasars,[129] using a pair of dual-channel optical fiber spectrographs fed by 640 fibers with 3″ diameters

(Smee et al. 2013). The galaxies were divided into two samples, a flux-limited Main Sample with a median redshift of $z \sim 0.1$ (Strauss et al. 2002) and a color-selected sample of Luminous Red Galaxies, which extended to $z \sim 0.5$ (Eisenstein et al. 2001). The quasar sample included both ultraviolet excess quasars out to $z \sim 2$ and a set of high-redshift quasars with redshifts beyond $z = 5$ (Richards et al. 2002).

Between 2005 July and 2008 June, SDSS-II completed the Legacy Survey with 1.3 million spectra over 8000 deg²; the area covered was a large contiguous region in the Northern Galactic Cap (NGC) and three long, thin stripes in the Southern Galactic Cap (SGC). SDSS-II also executed two new programs: The Sloan Extension for Galactic Understanding and Exploration 1 (SEGUE-1; Yanny et al. 2009) obtained around 3000 deg² of new imaging over a larger range of Galactic latitudes and spectra of 240,000 unique stars over a range of spectral types to investigate Milky Way structure. The Sloan Digital Sky Survey II Supernova Survey (Frieman et al. 2008; Sako et al. 2014) cataloged over 10,000 transient and variable sources, including 1400 SN Type Ia, over a 200 deg² region on the equatorial stripe in the SGC, referred to as Stripe 82. These two surveys primarily utilized the dark time.

Between 2008 July and 2014 June, SDSS-III conducted four surveys (Eisenstein et al. 2011). Stellar spectroscopy continued with SEGUE-2, which obtained 130,000 more stars during the first year of SDSS-III (Aihara et al. 2011). SDSS-III continued the imaging campaign, adding 2350 deg² of unique area and creating a contiguous footprint in the Southern Galactic Cap; at the end of 2009 the imaging camera was retired. In Summer 2009, for the Baryon Oscillation Spectroscopic Survey (BOSS; Dawson et al. 2013), SDSS-III upgraded the optical spectrographs to cover a larger optical range and accommodate 1000 fibers (Smee et al. 2013). By the end of SDSS-III, BOSS spectroscopically surveyed 10,338 deg², gathering 1.2 million galaxy spectra to extend the original luminous red galaxy sample from SDSS-I and SDSS-II to $z \sim 0.7$ and to increase its

---

[129] To refer to objects thought to have actively accreting supermassive black holes, we use the terms "quasar" or "active galactic nucleus (AGN)," sometimes interchangeably, throughout this paper.

sampling density at lower redshifts. It simultaneously used the Lyα forest in 140,000 spectra drawn from a sample of 180,000 observed quasars to map the fluctuations in neutral hydrogen at redshifts $2.1 < z < 3.5$. Both SEGUE-2 and BOSS were conducted using the dark time.

SDSS-III also employed the Sloan Foundation Telescope in bright time. From Fall 2008 through 2012 July, the Multi-Object APO Radial Velocity Exoplanet Large-area Survey (MARVELS; Ge et al. 2009) observed 5500 bright stars ($7.6 < V < 12$) with a 60-fiber interferometric spectrograph to measure high precision radial velocities, searching for extra-solar planets and brown dwarfs. Starting in 2011 May through 2014 June, the APO Galactic Evolution Experiment 1 (APOGEE-1; Majewski et al. 2015) observed 140,000 stars with a 300-fiber, $R \sim 22,500$, H-band spectrograph.

Because the weather efficiency of BOSS exceeded expectations, it finished its primary observations early, and during its last few months SDSS-III conducted several special programs in dark time (Alam et al. 2015a). The Sloan Extended QUasar, ELG, and LRG Survey (SEQUELS) observed 300 deg^2 using the BOSS spectrograph to obtain a dense set of quasars, emission-line galaxies (ELGs), and luminous red galaxies (LRGs), which was used to test target selection for SDSS-IV. The SDSS Reverberation Mapping program (SDSS-RM; Shen et al. 2015) observed a single field containing 849 quasars over more than 30 epochs in order to monitor quasar variability. During dark time when the inner galaxy was visible (local sidereal times 15–20 hr) the bulk of the time was allocated to the APOGEE-1 program.

Data from these surveys have been publicly released. The SDSS-I and SDSS-II Legacy, Supernova, and SEGUE-I survey data were released in a set of data releases beginning in 2001 and culminating in 2008 October with Data Release 7 (DR7; Abazajian et al. 2009). The complete SDSS-III data set was released in 2015 January in DR12 (Alam et al. 2015a).

1.2. SDSS-IV

SDSS-IV has new goals that build upon the scientific results of previous SDSS surveys in the areas of Galactic archeology, galaxy evolution, and cosmology. In so doing, SDSS-IV observations enable the detailed astrophysical study of stars and stellar systems, the interstellar and intergalactic medium, and supermassive black holes; some of the emerging science themes are described below. The primary goals of SDSS-IV are achieved in the following three core programs, two of which required new infrastructure.

1. *APO Galactic Evolution Experiment 2* (APOGEE-2; Section 4) aims to improve our understanding of the history of the Milky Way and of stellar astrophysics. It expands the APOGEE-1 probe of the Milky Way history through mapping the chemical and dynamical patterns of the Galaxy's stars via high resolution, near-infrared spectroscopy. The second-generation program has northern and southern components, APOGEE-2N and APOGEE-2S, respectively. APOGEE-2N continues at APO, with primary use of the bright time. APOGEE-2S utilizes new infrastructure and a new spectrograph now installed at the 2.5 m du Pont Telescope at Las Campanas Observatory (LCO). The pair of spectrographs at APO and LCO together target a total sample of around 400,000 stars. APOGEE-2's near-infrared observations yield

access to key regions of the Galaxy unobservable by virtually all other existing surveys of the Milky Way, which are predominantly conducted at optical wavelengths.

2. *Mapping Nearby Galaxies at APO* (MaNGA; Bundy et al. 2015; Section 5) aims to better understand the evolutionary histories of galaxies and what regulates their star formation. It provides a comprehensive census of the internal structure of nearby galaxies (median redshift $z \sim 0.03$), rendered via integral field spectroscopy (IFS) —a new observing mode for SDSS. This census includes the spatial distribution of both gas and stars, enabling assessments of the dynamics, stellar populations, and chemical abundance patterns within galaxies as a function of environment. Using half of the dark time at APO, MaNGA relies on novel fiber bundle technology to observe 17 galaxies simultaneously by feeding the fiber output of independent integral field units into the optical BOSS spectrographs. MaNGA plans to observe 10,000 nearby galaxies spanning all environments and the stellar mass range 10^9–10^{11} $M_\odot$. The MaNGA observations cover 3500 Å to 1 μm with about 65 km s^{-1} velocity resolution and 1–2 kpc spatial resolution.

3. *extended Baryon Oscillation Spectroscopic Survey* (eBOSS; Dawson et al. 2016; Section 6) aims to better understand dark matter, dark energy, the properties of neutrinos, and inflation. It pushes large-scale structure measurements into a new redshift regime ($0.6 < z < 2.2$). Using single-fiber spectroscopy, it targets galaxies in the range $0.6 < z < 1.1$ and quasars at redshifts $z > 0.9$. These samples allow an investigation of the expansion of the universe using the Baryon Acoustic Oscillation (BAO) and the growth of structure using large-scale redshift space distortions. The large-scale structure measurements also constrain the mass of the neutrino and primordial non-Gaussianity. Using half of the dark time at APO, eBOSS is to observe $\sim$250,000 new LRGs ($0.6 < z < 1.0$) and $\sim$450,000 new quasars ($0.9 < z < 3.5$) over 7500 deg^2. Using 300 plates to cover a portion of this footprint, it also aims to obtain spectra of $\sim$195,000 new ELGs ($0.7 < z < 1.1$).

There are two major subprograms executed concurrently with eBOSS, also described in Section 6.

1. *SPectroscopic IDentification of ERosita Sources* (SPI-DERS) investigates the nature of *X*-ray emitting sources, including active galactic nuclei and galaxy clusters. It uses $\sim$5% of the eBOSS fibers on sources related to X-ray emission. Most of its targets are X-ray emitting active galactic nuclei, and a portion are galaxies associated with X-ray clusters. Initially, SPIDERS targets X-ray sources detected mainly in the *ROSAT* All Sky Survey (RASS; Voges et al. 1999), which has recently been reprocessed (Boller et al. 2016). In late 2018, SPIDERS plans to begin targeting sources from the eROSITA instrument on board the Spectrum Roentgen Gamma satellite (Predehl et al. 2010; Merloni et al. 2012). Together with eBOSS, SPIDERS targets a sample of 80,000 X-ray identified sources ($\sim$57,000 X-ray cluster galaxies and 22,000 AGNs, of which around 5000 are already included in eBOSS targeting).

2. *Time Domain Spectroscopic Survey* (TDSS; Morganson et al. 2015) investigates the physical nature of time-variable sources through spectroscopy. It also uses ~5% of the eBOSS fibers, primarily on sources detected to be variable in Pan-STARRS1 data (PS1; Kaiser et al. 2010), or between SDSS and PS1 imaging. The targets identified in PS1 are a mix of quasars (about 60%) and stellar variables (about 40%). A majority of the quasars are already targeted by eBOSS. TDSS aims to produce a spectroscopic characterization of a statistically complete selection of ~200,000 variables on the sky down to $i = 21$. TDSS targets a total of around 80,000 objects not otherwise included by eBOSS targeting.

In executing these programs, we exploit several efficiencies allowed by the SDSS observing facilities. First, there is substantial common infrastructure and technology invested in the plate and cartridge hardware at APO and in the associated software. Second, the SDSS-IV survey teams closely coordinate the observing schedule on long and short timescales to maximize efficiency. Finally, MaNGA and APOGEE-2 are able to co-observe, which allows APOGEE-2 to observe a large number of halo stars during dark time and for MaNGA to create a unique optical stellar library in bright time.

In addition to these overlaps in infrastructure, there exist substantial scientific synergies between the SDSS-IV programs. These connections allow the surveys to explore a number of critical aspects of baryon processing into and out of gravitational potentials from scales of stars to galaxy clusters. We remark on two emerging themes that we expect to grow over the course of the survey. First, the science goals of APOGEE-2 and MaNGA are closely aligned in the context of understanding galaxy formation and evolution. APOGEE-2 treats the Milky Way as a detailed laboratory for asking questions about galaxy evolution similar to those MaNGA asks using a set of more distant galaxies observed in less detail. These vantage points are highly complementary because APOGEE-2 has access to chemo-dynamical structure on a star-by-star basis, while MaNGA samples all viewing angles for both gas and stars over a wide range of galaxy masses and environments. These disparate perspectives facilitate understanding the kind of galaxy we live in, and by extension, the detailed processes occurring in other galaxies.

Second, the eBOSS, TDSS, and SPIDERS programs create an unprecedentedly large and complete sample of quasars, essentially complete down to Seyfert luminosities out to nearly $z \sim 2$ (further discussion of quasar science is in Section 6.4). This sample serves as a critically important tool for understanding the evolution and decline in accretion rates of supermassive black holes, and in turn how active galactic nuclei impact the hosts in which they reside.

This paper describes the facilities that make these programs possible as well as the scientific goals, observational strategy, and management of the project and its associated collaboration. We pay particular attention to the new hardware developments of the program, which are primarily related to APOGEE-2S and MaNGA. More detail on all programs, and in particular how each survey's design addresses its high level requirements, is or will be available in existing and upcoming technical papers (Bundy et al. 2015; Morganson et al. 2015; Clerc et al. 2016; Dawson et al. 2016; Dwelly et al. 2017, and APOGEE-2 and TDSS papers in preparation).

Section 2 provides an overview of the APO and LCO facilities. Section 3 describes the imaging data utilized in SDSS-IV, which includes significant reanalysis of SDSS and *Wide-field Infrared Survey Explorer* (*WISE*) images. Sections 4 through 6 present the survey programs. Section 7 describes the data management and distribution plan for the project. Section 8 provides a summary of the education and public engagement strategies employed by the project. Section 9 describes the project management and organization of the science collaboration, including the activities associated with fostering and maintaining a healthy climate within SDSS-IV. Section 10 provides a brief summary.

2. SDSS-IV Facilities

The primary departure in SDSS-IV from previous survey generations is the expansion of our observing facilities to include telescopes in both hemispheres. In contrast to the requirements for extragalactic surveys on scales where the universe is isotropic, such as MaNGA and eBOSS, this expansion is essential for the study of the Milky Way in APOGEE-2. In particular, the south affords much more efficient access to the Galactic bulge and the inner disk, even for near-infrared surveys that can operate at high airmass; full mapping of the Milky Way, including the disk and bulge where APOGEE's near-infrared view has the greatest advantage, requires all-sky coverage.

Since its inception, SDSS has used the 2.5 m Sloan Foundation Telescope at the Apache Point Observatory (APO), located in the Sacramento Mountains of south-central New Mexico. Since the advent of APOGEE-1 in SDSS-III, the NMSU 1 m Telescope (Holtzman et al. 2010) at APO has also been used with the APOGEE spectrograph. SDSS-IV adds the 2.5 m du Pont Telescope (Bowen & Vaughan 1973) located at the Las Campanas Observatory (LCO) in the Andean foothills of Chile. On the 2.5 m Sloan Foundation Telescope, we continue to operate the BOSS spectrographs for the eBOSS and MaNGA programs during dark time, and the APOGEE spectrograph during bright time. For the 2.5 m du Pont Telescope, a second, nearly identical APOGEE spectrograph was constructed for the southern component of the APOGEE-2 survey.

2.1. Apache Point Observatory

The 2.5 m Sloan Foundation Telescope at APO is a modified two-corrector Ritchey–Chretién design, with a Gascoigne astigmatic corrector, and a highly aspheric corrector designed for spectroscopy near the focal plane. It has a $3°$ diameter usable field of view, and a focal ratio of $f/5$. Commissioned during the late 1990s, it has been acquiring survey data for the past 19 years. It performed photometric imaging through 2009; for this purpose, there was an alternative corrector near the focal plane designed for imaging mode. It has performed multi-object fiber-fed spectroscopy through the present, and is devoted to this task exclusive in SDSS-IV. The on-axis focal plane scale is nominally 217.736 mm deg^{-1}.

The telescope system is maintained and operated throughout the year by engineering and administrative staff plus a team of nine full-time observers and two to three plate-pluggers. On each night of observing, two observers are on duty. The field change operation involves the manipulation of the cartridges, which weigh 100–130 kilograms, on the telescope pier near the

telescope, in dark, often cold, and occasionally icy conditions. The presence of two observers on site is necessary to ensure instrument and personnel safety. The use of dedicated, full time employees as observers is necessary for maintaining safe working conditions and contributes to the high reliability of the system and the homogeneity of the resulting data set.

We conduct multiplexed spectroscopic observations on the Sloan Foundation Telescope in the following manner. Each day, the plugging technicians prepare a set of cartridges with aluminum plates plugged with optical fibers. Each plate corresponds to a specific field on the sky to be observed at a specific hour angle. When the cartridge is engaged on the telescope, the plate is bent to conform to the telescope focal plane in the optical. Depending on the cartridge configuration, the optical fibers feed either the BOSS optical spectrographs (Smee et al. 2013), the APOGEE spectrograph (Wilson et al. 2012), or both. The cartridges are initially staged in a bay near the telescope and allowed to equilibrate with the outside air temperature. During the night, the observers can swap the cartridges efficiently so that a number of fields can be observed throughout the night. Dawson et al. (2013) provide a detailed description of this procedure. The APO observers submit observing reports each morning and track time lost due to weather and technical problems on a monthly basis. Technical issues have led to <1% time loss overall over the past few years.

The system has 17 cartridges used for spectroscopy. Eight have 1000 fibers that emanate at two slit heads (500 fibers each). The slit heads directly interface with the two pairs of BOSS optical spectrographs. Each pair consists of a red spectrograph and a blue spectrograph that together cover the optical regime from 356 nm to 1040 nm, with $R \sim 1500$–2500. The fibers have 120 μm active cores, which subtend $2''$ on the sky.

The other nine cartridges contain 300 short fibers that are grouped in sets of 30 into harnesses and terminate in US Conec MTP fiber connectors. The 10 fiber connectors are in turn grouped into a precision gang connector that connects to a set of long ($\sim$40 m) fibers extending from the telescope into the APOGEE instrument room and terminating on the APOGEE spectrograph slit head. The APOGEE instrument has a wavelength coverage of 1.5–1.7 μm, with $R \sim 22{,}500$. As in the case of BOSS, the fibers have 120 μm active cores. Through most of SDSS-III, there were eight APOGEE-2 cartridges; in early 2014, one BOSS cartridge was converted to an APOGEE cartridge.

New in SDSS-IV, six of the nine APOGEE cartridges have an additional short fiber system for MaNGA that interfaces with the BOSS spectrographs (Drory et al. 2015). The MaNGA fiber system consists of 17 IFUs and 12 mini-IFUs, plus 92 sky fibers, for 1423 fibers in total. These fibers are spaced more densely on the spectrograph slit head, which leads to a greater degree of blending between the spectra; this blending is more tolerable in MaNGA than in BOSS because neighboring MaNGA spectra on the spectrograph are also neighboring on the sky, which reduces the dynamic range in flux between neighboring spectra. As is the case for the APOGEE and BOSS systems, all of these fibers have 120 μm active cores; however, the cladding and buffer on the fibers were reduced to increase the filling factor of the IFU. The resulting spectra have nearly the same properties of those taken with the BOSS spectrographs. These six cartridges are capable of simultaneous APOGEE

and MaNGA observations. The first MaNGA cartridge was commissioned in 2014 March, and the final one became operational in 2015 January. Section 5 describes the system and its use in more detail.

In addition to the science fibers, each cartridge contains a set of 16 coherent fiber bundles that are plugged into holes centered on bright stars and are routed to a guide camera that functions at visible wavelengths ($\sim$5500 Å). The operations software uses the guide camera feedback to control telescope position, rotator position, and focal plane scale. During APOGEE observations, the guiding software accounts for the chromatic differential refraction between visible wavelengths and APOGEE wavelengths in order to best align the APOGEE fibers with the images in the focal plane at 1.66 μm.

A special purpose fiber connection exists between the NMSU 1 m Telescope and the APOGEE spectrograph. Seven fibers are deployed in the NMSU 1 m focal plane in a fixed pattern; one fiber is used for a science target and the remainder for sky measurements. This mode can be activated when the APOGEE spectrograph is not being used by the Sloan Foundation Telescope.

A database (apodb) at APO tracks the status and location of all plates and cartridges. An automatic scheduling program (autoscheduler) determines which plates should be plugged or observed at any given time. The pluggers and observers use a web application (Petunia) to interface with the database and view autoscheduler output. Occasionally, human intervention and re-prioritization of the automatic schedule is required; this action is performed by Petunia. The observers use a graphical user interface (STUI) to send commands to and receive feedback from the operations software controlling the telescope and instruments.

SDSS-IV, APOGEE-2N, MaNGA, and eBOSS share the APO observing time from 2014 July 1 to 2020 June 30. The observatory functions all year except for the summer shutdown period, a roughly six-week hiatus for engineering and maintenance in July and August, during the season with the worst weather for observing. Major engineering work is scheduled for this period. The baseline plan for observations allocates the bright time to APOGEE-2 and splits the dark time between eBOSS and MaNGA; the exact allocations are adjusted to best achieve the overall science goals depending on progress during the survey. We describe here the baseline plan at the start of the survey. The overall number of hours available in the survey is 18,826 (excluding engineering nights, typically taken at full moon). This number (and those below) assumes uneventful recommissioning of the telescope after each summer shutdown.

APOGEE-2 uses the 8424 of those hours that are deemed bright time, because the APOGEE-2 observations are of sources typically much brighter than the sky background. We define bright time as when the moon is illuminated more than 35% and is above the horizon. For APOGEE-2, science observations occur between $8°$ twilight in the "summer" (roughly between the vernal and autumnal equinoxes) and between $12°$ twilight in the "winter," to avoid overworking the observers. In the "summer" period, APOGEE-2 also utilizes dark time in the morning twilight between $15°$ and $8°$, which eBOSS and MaNGA cannot use.

eBOSS and MaNGA use the remaining hours, when the moon is below the horizon or illuminated at less than 35%. For these dark time programs, science observations occur between

Table 1
Initial Allocations for SDSS-IV APO Programs

LST (Hours)	Time Allocated (Hours)		
	APOGEE-2	MaNGA	eBOSS
0–1	322.9	22.4	423.0
1–2	350.0	55.1	434.0
2–3	372.1	99.5	409.4
3–4	377.9	168.7	337.1
4–5	375.8	215.6	290.5
5–6	377.3	225.1	279.4
6–7	373.7	239.5	261.4
7–8	373.2	283.8	219.3
8–9	379.0	296.3	202.5
9–10	377.2	287.5	210.4
10–11	385.2	284.0	206.5
11–12	384.1	308.1	177.8
12–13	388.8	291.5	185.6
13–14	388.1	273.3	193.2
14–15	390.7	317.9	135.1
15–16	380.7	351.3	72.9
16–17	339.6	284.6	67.0
17–18	316.3	230.2	49.8
18–19	316.8	212.5	65.8
19–20	294.0	171.4	134.6
20–21	288.6	132.3	194.7
21–22	285.2	96.0	250.7
22–23	288.7	40.4	319.0
23–24	298.0	16.8	377.6

Figure 1. Model of the du Pont Telescope configuration during APOGEE-2S observations. The yellow transparent box indicates the bottom of the telescope, with the gray annulus indicating the location of the primary mirror. The scaling ring mechanism with a cartridge attached is just below the primary. A telescope fiber link connects the cartridge to a patch panel at the end of the boom. The instrument fibers travel down a movable boom to the wall of the dome, and are directed to the instrument room in the level below the telescope dome. The room on the dome level on the right side of the diagram is used for plate plugging and mapping during the night.

$15°$ twilights. Although eBOSS and MaNGA split the effective observing time in SDSS-IV, in practice, the implementation is complicated by observational limitations. MaNGA requires the bulk of its time to be spent when the NGC is observable. Because MaNGA target selection is based on the Legacy spectroscopic survey, it has available 7500 deg^2 of targeting in the NGC but only 500 deg^2 in three isolated stripes in the SGC (Abazajian et al. 2009). Providing sufficient targeting, and assuring that three-dimensional environmental information is available for each target, requires MaNGA to be NGC-focused and eBOSS to be SGC-focused. In addition, the SGC is more difficult to observe because of Galactic dust foregrounds. Therefore, in accounting for the time balance between eBOSS and MaNGA, 1.4 hr of SGC dark time is effectively equivalent to 1.0 hr of NGC dark time. As a result, eBOSS is assigned 5497 hr and MaNGA 4904 hr.

The inital time allocation for the three surveys as a function of Local Sidereal Time (LST) is shown in Table 1.

2.2. Las Campanas Observatory

The 2.5 m Irénée du Pont telescope is a modified Ritchey–Chrétien optical design held in an equatorial fork mount. With a Gascoigne corrector lens, it has a $2°.1$ diameter usable field of view (Bowen & Vaughan 1973) with a focal ratio of $f/7.5$. The on-axis focal plane scale is nominally 329.310 mm deg^{-1}. The du Pont telescope design informed a number of features of the Sloan Foundation telescope at APO (Gunn et al. 2006).

Completed in 1977, the du Pont telescope pioneered early wide-field fiber spectroscopy. Shectman (1993) describes the fiber system used for the Las Campanas Redshift Survey (LCRS, Shectman et al. 1996) that formed a basis for the design of the SDSS observing systems. Since the completion of
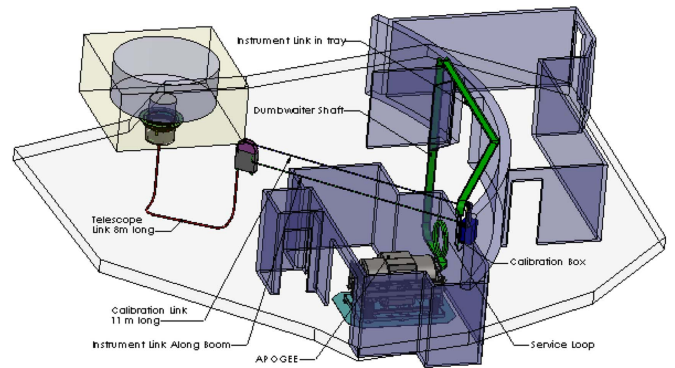
the LCRS, the du Pont telescope has not been used for wide-field spectroscopy. SDSS-IV is creating the infrastructure to return to this mode of operation with improved efficiency. The primary system upgrades include an expanded range of motion for the corrector lens (to optimize wide-field image quality in the H band), improved servo-control of the instrument rotator, and re-design of the secondary mirror mounting structure for increased stiffness and enhanced collimation and focus control. In addition, implementation of a new flat-field system is planned to optimize observing efficiency. The telescope drives, control electronics, and control software have also been recently modernized.

The SDSS-IV project is designing, fabricating and installing an optical fiber cartridge and plugging system for LCO that is similar to that at APO. We use five interchangeable cartridges with 300 short fibers that can be re-plugged throughout each night, with a plan to support observations of up to 10 plates per night. The short fibers in each cartridge are precisely connected through a fiber link (the "telescope link") to a set of long fibers that transmit light to the spectrograph on the ground floor of the telescope building. The fibers run along a long metal boom attached to the wall of the dome, and which can rotate to lie along the wall to keep the fibers safe during observations and to provide safe storage.

Each cartridge includes a plug plate mechanically bent to conform to the telescope's focal surface, which at 1.6 μm has a radius of curvature of 8800 mm. The focal plane position parallel to the optical axis varies around 6 mm between the center and edge of the field (Shectman 1993), compared to around 2 mm for the Sloan Foundation Telescope in the optical. To achieve this large flexure, the outer part of the plate is held at a fixed angle with a bending ring (as done at APO). The plate profile is verified and the profile measurements are stored in the SDSS-IV LCO database (`lcodb`).

Figure 1 shows the configuration during observations, in particular, the fiber run. The bottom of the du Pont Telescope and the primary mirror are shown as the yellow box and the inset gray annulus, respectively. The secondary focal plane is located approximately 8 feet above the dome floor when the telescope points to zenith. During APOGEE-2S operations, a focal plane scaling mechanism is attached at the secondary

Table 2
APOGEE-2 Targeting Description

Target	N or S	N_{plate}	N_{visit}	N_{star}	Abundances
Clusters	N	31	63	2340	complete
	S	63	158	8715	complete
Bulge	N	1	18	230	complete
	S	213	321	38310	complete
Inner Disk	N	116	348	20010	complete
Outer Disk	N	93	279	21390	complete
Disk	S	179	537	30470	complete
dSph	N	12	72	780	partial
	S	12	72	780	partial
Halo-NGC	N	84	504	5460	complete
	S	4	48	480	complete
Halo-SGC	N	28	87	6670	complete
	S	24	72	5520	complete
Streams-NGC	N	48	288	3840	partial
Streams-SGC	N	9	39	1410	partial
	S	2	12	345	partial
APOKASC	N	56	56	12880	complete
KOI	N	5	90	1150	complete
Halo Co-obs	N	600	600	120000	complete
LMC	S	51	153	4930	partial
SMC	S	24	78	1920	partial
SGR	S	4	30	1405	complete
RR Lyrae	S	31	31	4000	⋯
TOTALS	N	1084	2444	196160	
	S	607	1512	96875	

focus. Cartridges must latch to this scaling mechanism in order to be observed. As shown, the fibers exit the cartridge, run along a boom to the dome wall, and travel down a level to the instrument room.

The scaling mechanism allows real-time changes in plate position along the optical axis. With corresponding movement of the telescope's secondary mirror, this can be used to alter the focal plane scale to compensate for changes introduced by differential refraction, thermal expansion and contraction of the plate, and stellar aberration. The scaling mechanism is controlled by the SDSS operations software as part of the overall guiding system.

In order to implement efficient cartridge changes on the scaling mechanism, we have constructed a stable three-rope hoist system, which lifts the cartridges into place in the focal plane. The five cartridges themselves are stored on custom-built dollies so they can be maneuvered about the observing floor and plugging room. Cartridges are plugged in a room next to the dome, then placed in the dome to equilibrate with the dome temperature. When a cartridge is ready to be observed, it is rolled to the hoist, attached to the three ropes, and lifted to the focal plane. Electrical cabinets attached to the scaling ring house the motion control electronics, while a second electrical cabinet at the end of the fiber boom contains an LCD touch screen (VMI), allowing the user to control the system. The VMI communicates with the scaling ring electronics through a Bluetooth connection. A set of interlocks prevent the cartridge from being lifted in an unsafe state (e.g., not fully attached to the hoists) or from being left unsecured to the scaling mechanism.

The focal plane and its distortions are estimated using Zemax and an adjusted version of the specifications from Bowen & Vaughan (1973). From the analysis of test images the "best" focal distance is 254 mm below the rotator (993 mm from the

secondary). We have directly measured the on-axis scale and distortions at 229 mm and 279 mm below the rotator by observing star fields using a camera positioned at various radii in the focal plane. We have found that the specifications in Bowen & Vaughan (1973) do not reproduce these scales well. Their Table 1 entry of the telescope focal length does not include the contribution of the corrector. We use a Zemax model based on the surface specifications in their Table 2, including the corrector, with the curvature of the primary and secondary adjusted to be consistent with our observed scales. The resulting nominal scale and distortion is modeled with a quintic function $s = s_0\theta + s_3\theta^3 + s_5\theta^5$. Our best current estimates yield, in the H band, $s_0 = 329.342$ mm deg^{-1}, $s_3 = 2.109$ mm deg^{-3}, and $s_5 = 0.033$ mm deg^{-5}, and at the guider camera wavelength of 7600 Å, $s_0 = 329.297$ mm deg^{-1}, $s_3 = 2.168$ mm deg^{-3}, and $s_5 = 0.021$ mm deg^{-5}. These estimates may be further refined in the course of commissioning the system.

The cartridges contain guide systems similar to those used on the telescope at APO. Because the system is being solely designed for use with APOGEE-2S, we have designed a camera with effective wavelength around 7600 Å, which should increase its ability to use guide stars in the more reddened part of the Milky Way. The camera is an Andor iKon-M 394 with a 1024 × 1024 pixel CCD, with 13 μm pixels. This configuration is similar to that currently used at APO (Smee et al. 2013). The effective wavelength is defined by an Astrodon Photometrics Gen 2 Sloan i filter. The filter is mounted in the parallel beam between the two Nikon $f/1.4$ 35 mm lenses that comprise the transfer optics from the output fiber block to the CCD. The guide fibers and transfer optics preserve the telescope focal plane scale. Each 13 μm guider pixel subtends $0\overset{''}{.}142$ on the sky. The camera is operated binned 2 × 2 for guiding; thus each binned pixel subtends $0\overset{''}{.}284$ on the sky.

The plug plates for APOGEE-2S are nearly identical to those used at APO. On the du Pont telescope, we use a $1\overset{\circ}{.}9$ diameter field of view, which is similar in physical size to the Sloan Foundation Telescope. As at APO, the fibers have 120 μm diameter cores to preserve the instrumental resolution of the spectrograph. The fiber core size corresponds to $1\overset{''}{.}3$ on the sky. The smaller angular size at LCO relative to APO is appropriate for the better median seeing at LCO ($\sim 0\overset{''}{.}7$ FWHM in the H band). Relative to APO, this configuration does place stricter constraints on telescope pointing and focus (despite the slower beam of the du Pont).

The fibers feed the APOGEE-South spectrograph, a near-clone of the APOGEE spectrograph at APO. Changes in the new spectrograph are described in more detail in Section 4.

APOGEE-2S uses approximately the equivalent of 75 nights per year on the du Pont telescope starting in 2017 and continuing through 2020 June. In addition, up to 25 nights per year are available to guest observers through Carnegie Observatories and the Chilean Time Allocation Committee. All observations are conducted in ~ 10 night observing runs throughout the year. The southern APOGEE-2 program has led to a developing partnership between SDSS-IV and astronomers at seven Chilean universities that have joined the SDSS-IV project in a collaboration on the design, construction, engineering, and execution of the survey. This Chilean Participation Group is an unprecedentedly broad collaboration among Chilean universities in astronomy and dovetails with the

interest of the Chilean government in developing astronomical engineering as a national strategy in technology transfer and development of science.

2.3. Plate Drilling

The plates used at APO and LCO are produced for SDSS-IV using the same systems used in previous SDSS programs. The plates themselves are 3.2 mm thick aluminum plates, 80 cm in diameter, with a 65.2 cm diameter region in which holes can be drilled to place fibers. Each fiber or IFU is housed in a metal ferrule whose tip ranges in size from 2.154 mm to 3.25 mm in diameter. The larger diameter ferrules are employed in the MaNGA and LCO systems; all others use a 2.154 mm diameter (see Sections 4.5, 5.5, and 6.1.4 for details). The ferrules have a larger base that rests on the back side of the plate to keep the fiber tip position fixed in focus.

Each survey plans potential observations several months in advance and determines the sky coordinates and optimal Local Sidereal Times (LSTs) for a set of plates. Based on the target selection results, the potential targets in each field are assigned fibers. The fiber placements have some physical constraints, most significantly with regard to the minimum separation of fibers. Other constraints on the fiber assignment based on target type and brightness can be applied. These constraints are described below for APOGEE-2, MaNGA, and eBOSS.

Given a desired observation at a given celestial location and LST, the target coordinates are translated into observed altitude and azimuth given atmospheric refraction and the observatory location. These coordinates are translated into the physical focal plane location of each target image, based on telescope scale and distortions. Finally, the focal plane location is translated into a drilling location taking into account the relative bending of the plate and the thermal expansion of the plate due to the difference between the drill shop temperature and the estimated observing temperature.

A large format vertical milling machine (a Dah Lih MCV-2100) at the University of Washington drills each plate (Siegmund et al. 1998). During drilling, the APO plates are bent on a mandrel such that the fiber angle will be aligned with the chief ray at that position on the focal plane. The LCO plates are fixed to a flat fixture, since, for the du Pont Telescope, the chief ray is normal to the focal plane.

When observed at APO, the plates are bent to match the focal plane curvature at around 5400 Å. The H-band focal plane has a slightly smaller radius of curvature. In order for APOGEE fibers to remain near the H-band focus in the outer parts of the plate, a shallow "counterbore" is drilled on the back side of the plate, so that when the base of the ferrule rests inside this counterbore, the fiber tip extends beyond the plate surface slightly in order to reach the H-band focal plane. When observed at LCO, the plates are bent to match the focal plane in the H band, so no counterboring is necessary.

At both observatories, the bending is achieved using a center post with a 4.87 mm radius. We insert a further 1.1 mm buffer between the post and the outer diameter of any ferrule, restricting the placement of targets very near the centers of plates.

A Coordinate Measuring Machine measures a subset of holes on each plate for quality assurance purposes. The typical errors measured in hole position are $10 \, \mu$m. This error has increased somewhat over time from $7 \, \mu$m since the system was first installed in 1996. However, this contribution to the total fiber position error is subdominant. As plugged, the median fiber position offset is $13 \, \mu$m; 90% of fibers do better than $22 \, \mu$m. The most important error contribution arises from the slight "clearance" tilts induced when each fiber is plugged, because the holes are by necessity slightly larger than the ferrules.

3. SDSS-IV Imaging Data

For the purposes of the SDSS-IV survey targeting, we have undertaken the re-analysis of a variety of existing imaging data sets. We will refer to these data sets in subsequent sections describing the survey programs.

We have applied a photometric recalibration to the SDSS imaging data set. Using the PS1 photometric calibrations of Schlafly et al. (2012), Finkbeiner et al. (2016) have rederived the g, r, i, and z band zero points and the flat fields in all five SDSS bands (including u). The residual systematics are reduced to 0.9, 0.7, 0.7, and 0.8% in the $griz$ bands, respectively; several uncertain calibrations of specific imaging scans are also now much better constrained. The resulting recalibrated images and imaging catalogs are the basis for the eBOSS and MaNGA targeting. They are now included as the default imaging data set in SDSS-IV public data releases, starting in DR13.

All the targeting based on SDSS imaging in SDSS-IV uses the DR9 astrometric calibration (Pier et al. 2003; Ahn et al. 2012) for both targets and for guide stars. The SDSS-III BOSS survey used the previous DR8 astrometric calibration, which has known systematic errors. Because the systematic errors were fairly coherent over the SDSS field-of-view, the fiber flux losses due to these errors were relatively minor.

For the purposes of the MaNGA target selection, we are using the NASA-Sloan Atlas (NSA; Blanton et al. 2011), a reanalysis of the SDSS photometric data using sky subtraction and deblending better tuned for large galaxies. Relative to the originally distributed version of that catalog, we have used the new calibrations mentioned above, increased the redshift range to $z = 0.15$, and have added an elliptical aperture Petrosian measurement of flux, which MaNGA targeting is based upon.

For the purposes of eBOSS target selection, Lang et al. (2016) reanalyzed data from *WISE* (Wright et al. 2010). Using positions and galaxy profile measurements from SDSS photometry as input structural models, they constrained *WISE* band fluxes using the *WISE* imaging. These results agree with the standard *WISE* photometry to within 0.03 mag for high signal-to-noise ratio, isolated point sources in *WISE*. However, the new reductions also provide flux measurements for low signal-to-noise ratio ($<5\sigma$) objects detected in the SDSS but not in *WISE* (over 200 million objects). Despite the fact that the objects are undetected, their flux measurements are nevertheless informative to target selection, in particular, for distinguishing stars from quasars. These results have been used for eBOSS targeting and have been released in DR13.

Several additional imaging analyses have been performed for targeting SDSS-IV data; these extra sources of imaging will not necessarily be incorporated into the SDSS public data releases, although some of them have been released separately in some cases.

1. Variability analysis of Palomar Transient Factory (PTF; Law et al. 2009) catalogs to detect quasars (Palanque-Delabrouille et al. 2016; Section 6.1.3).
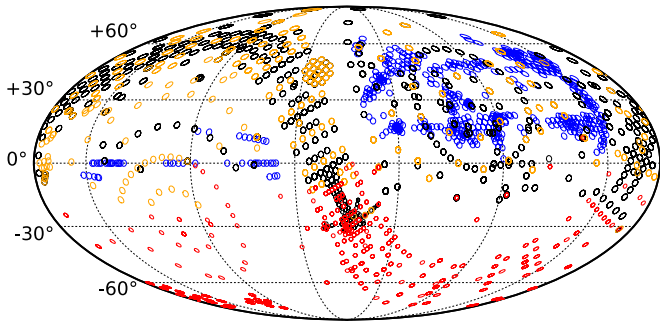
Figure 2. APOGEE-1 and planned APOGEE-2 spectroscopic footprint in equatorial coordinates, centered at $\alpha_{J2000} = 270°$, with east to the left. Black shows APOGEE-1 data, orange indicates APOGEE-2N, and red is APOGEE-2S. Blue shows projected MaNGA coverage for which APOGEE-2 can potentially have observations of stars (see also Figure 5). Because of logistical constraints and potential changes in the MaNGA plans, the final coverage of the halo may differ somewhat from this figure.

2. Selection of variable sources from PS1 (Morganson et al. 2015; Section 6.3.2).

3. Intermediate-band imaging in Washington M, T_2, and DDO 51 filters for APOGEE-2 (Majewski et al. 2000; Zasowski et al. 2013; Section 4.4).

4. Selection of emission-line galaxies from the Dark Energy Camera Legacy Survey (DECaLS), a g, r, and z band photometric survey being performed in preparation for the Dark Energy Spectroscopic Instrument (DESI; Levi et al. 2013) project.

For the purposes of eBOSS and MaNGA targeting, we correct magnitudes for Galactic extinction using the Schlegel et al. (1998) models of dust absorption. Galactic extinction coefficients have been updated as recommended by Schlafly & Finkbeiner (2011). The extinction coefficients R_u, R_g, R_r, R_i, and R_z are changed from the values used in BOSS (5.155, 3.793, 2.751, 2.086, and 1.479) to updated values (4.239, 3.303, 2.285, 1.698, and 1.263). We set $R_{W1} = 0.184$ for the WISE 3.4 μm band and $R_{W2} = 0.113$ for the 4.6 μm band (Fitzpatrick 1999).

4. APOGEE-2

4.1. APOGEE-2 Motivation

APOGEE-2 is conducting high-resolution, high signal-to-noise ratio spectroscopy in the near-infrared for a large sample of Milky Way stars. A key challenge in astrophysics is the characterization of the archeological record, chemical evolution, dynamics, and flows of mass and energy within galaxies. The Milky Way provides a unique opportunity to examine these processes in detail, star-by-star. Large spectroscopic samples are critical for mapping the Galaxy's numerous spatial, chemical, and kinematic Galactic sub-populations.

APOGEE-2 is creating a Galactic archeology sample designed to understand the history of all components of the Milky Way, including the dust-obscured ones (Figure 2), and to better understand the stellar astrophysics necessary to uncover that history. APOGEE-2 is accomplishing this goal by continuing the overall strategy of APOGEE-1 (Zasowski et al. 2013; Majewski et al. 2015), increasing to 400,000 the number of stars sampled, and expanding to cover the inner Galaxy from the Southern Hemisphere. The primary sample is a set of red giant branch stars that trace Galactic structure and

evolution. Several smaller sets of targets explore more specific aspects of Galactic and stellar astrophysics. These spectra yield precise radial velocities, stellar parameters, and abundances of at least 15 elements. The Sloan Foundation Telescope at APO and the du Pont Telescope at LCO are mapping both hemispheres of the Milky Way.

APOGEE-2 is distinguished from all other Galactic archeology experiments planned or in progress by its combination of high spectral resolution, near-infrared wavelength coverage, high signal-to-noise ratio, homogeneity, dual-hemisphere capability, and large statistical sample. It improves upon other Milky Way spectroscopic surveys that lack the combined high resolution and S/N needed by current methodology for the determination of accurate stellar parameters and chemical abundances (RAVE, Steinmetz et al. 2006; Kordopatis et al. 2013; BRAVA, Howard et al. 2008; SEGUE-1 and SEGUE-2, Yanny et al. 2009; *ARGOS*, Freeman et al. 2013; and LAMOST, Cui et al. 2012; Zhao et al. 2012). APOGEE-2 complements existing or future wide-angle, high-resolution stellar spectroscopic surveys or instruments that are single-hemisphere and are optical, experiencing heavy dust extinction at low Galactic latitudes and in the inner Galaxy (GALAH, Zucker et al. 2012; De Silva et al. 2015); *Gaia*-ESO, Gilmore et al. 2012; WEAVE (Dalton et al. 2014; 4MOST, de Jong et al. 2014). MOONS (Cirasuolo et al. 2014) is the closest analog and is complementary in ambition; it is a near-infrared instrument under construction for the Very Large Telescope in the Southern Hemisphere, with a larger number of fibers (1024) and telescope aperture size (8.2 m), but with a 20 times smaller field of view (500 arcmin^2).

Like other high-resolution surveys and instruments, APOGEE-2 complements the optical *Gaia* satellite measurements of parallax, proper motion, and spectroscopy of a much larger number of stars (Prusti et al. 2016). APOGEE-2 will benefit from the accurate measurements of distance and proper motion from *Gaia* for its stars. Our understanding of the Galactic chemical and dynamical structure will be strengthened using the APOGEE-2 information available for these stars: more precise radial velocities, more precise stellar atmospheric parameters, and more precise abundances for a larger set of elements.

4.2. APOGEE-2 Science

The combined APOGEE-1 and APOGEE-2 data sets yield multi-element chemical abundances and kinematic information for stars from the inner bulge out to the more distant halo in all longitudinal directions and include both Galactic satellites and star clusters. To effectively exploit these data, APOGEE-2 is collecting additional observations on fundamental aspects of stellar physics necessary to promote the overall understanding of the formation of the Galaxy.

Near-infrared spectra are excellent for studies of stars in the Galactic disk and bulge. The bulk of these regions suffer high extinction from foreground dust in the visible, with regions in the Galactic plane frequently yielding $A_V > 10$ (Nidever et al. 2012). With $A_H/A_V \sim 0.16$, NIR observations can peer through the dust far more efficiently than optical data. The H band is rich in stellar atomic (e.g., Fe, Ti, Si, Mg, and Ca) and molecular (e.g., CO, OH, CN) absorption lines that can be used to determine stellar properties and elemental abundances (Mészáros et al. 2013; Holtzman et al. 2015; Shetrone et al. 2015). In particular, lines in the H band are sensitive to

the most common metals in the universe, C, N, and O, which are difficult to measure in the optical. The luminous red giant branch (RGB) population dominates useful source catalogs like 2MASS, and selecting targets by H-band flux and red $J - K_s$ color yields a population relatively unbiased in age and metallicity.

As shown in APOGEE-1 (Holtzman et al. 2015) typical APOGEE-2 spectra enable measurements of at least 15 separate chemical abundances with 0.1 dex precision and high precision radial velocities (better than $100 \, \mathrm{m \, s}^{-1}$). The final spectra are the result of coadding several observations spaced up to a month or more apart; these time series data can identify radial velocity variables and detect interesting binaries and substellar companions.

APOGEE-2's magnitude and color selection criteria result in a main survey sample dominated by distant red giant, subgiant, and red clump stars, but with some contribution from nearby late-type dwarf stars. Through the inclusion of supplementary science programs, the final APOGEE-2 program also includes observations of RR Lyrae stars, high-mass and early main-sequence objects, as well as pre-main-sequence stars. Combined, these programs will address a number of topics in Galactic and stellar astrophysics.

1. Mapping of the thick and thin disk at all Galactic longitudes, including the inner disk regions, and at the full range of Galactic radii, with substantial samples at least 6 kpc from the Sun and with a significant subsample having reliably determined ages. These maps expand upon APOGEE-1 results (Anders et al. 2014; Nidever et al. 2014; Hayden et al. 2015), and further test scenarios of inside-out growth, radial migration, and the origin of the α-enriched population (Chiappini et al. 2015; Martig et al. 2015; Bovy et al. 2016b).
2. Accurate stellar ages and masses from the combination of APOGEE data with asteroseismology (e.g., Epstein et al. 2014; Chiappini et al. 2015; Martig et al. 2015), establishing critical benchmarks in the analysis of Galactic chemistry and dynamics in numerous directions sampled by *Kepler* and its subsequent K2 mission.
3. Dynamics of the disk and the Galactic rotation curve, including non-axisymmetric influences of the bar and spiral arms (e.g., Bovy et al. 2012a, 2015).
4. Three-dimensional mapping of the Galactic bulge and bar, measuring dynamics of the bar, bulge, and nuclear disk (Nidever et al. 2012; Schönrich et al. 2015; Ness et al. 2016), and their chemistry (García Pérez et al. 2013; Ness et al. 2015). Southern Hemisphere operations as well as the inclusion of standard candles such as red clump and RR Lyrae stars will make this mapping more complete and precise than APOGEE-1.
5. Chemistry and dynamics in the inner and outer halo across all Galactic longitudes, including a large area of the NGC, and sampling known halo substructure and stars reaching to at least 25 kpc.
6. Stellar populations, chemistry and dynamics of nascent star clusters, open clusters, globular clusters at various evolutionary stages, dwarf spheroidals, the Magellanic Clouds, and other important components of the Milky Way system (e.g., Frinchaboy et al. 2013; Majewski et al. 2013; Mészáros et al. 2013; Cottaar et al. 2014, 2015; Foster et al. 2015; García-Hernández et al. 2015; Mészáros et al. 2015; Bovy 2016).

7. Exoplanet host observations in *Kepler* fields to characterize host versus non-host properties and assess false positive rates (Fleming et al. 2015).
8. Detection of stellar companions of stellar, brown dwarf, and planetary mass across the Galaxy (e.g., Troup et al. 2016).
9. Mapping the interstellar medium using Diffuse Interstellar Bands (Zasowski et al. 2015a, 2015b), or dust reddening effects (Schultheis et al. 2014).

APOGEE-2 is also pursuing ancillary science programs with a small fraction of the available fibers to utilize more targeted and exploratory uses of the APOGEE instruments.

4.3. APOGEE-2 Hardware

APOGEE-2 utilizes one existing spectrograph at APO (Eisenstein et al. 2011; Wilson et al. 2012; Majewski et al. 2015) and a second instrument at LCO. Each spectrograph is fed with 300 fibers with 120 μm cores; both yield nearly complete spectral coverage between $1.51 \, \mu\mathrm{m} < \lambda < 1.70 \, \mu\mathrm{m}$, high spectral resolution ($R \sim 22{,}500$, as measured for the first spectrograph) and high S/N (>100 pixel^{-1}) for most targets (Majewski et al. 2015). The APOGEE spectrographs each utilize a large mosaic volume-phase holographic (VPH) grating. At APO, the first spectrograph's VPH grating consisted of three aligned panels on the same substrate. The spectrograph cameras consist of four monocrystalline silicon lenses and two fused silica lenses. The spectra are dispersed onto three Teledyne H2RG array detectors with 18 μm pixels, sampling three adjacent spectral ranges; all elements of each array are sampled "up-the-ramp" at 10.7 second intervals within each exposure. This procedure yields an effective detector read-noise of $\sim 10 \, e^-$ per pixel. The geometric demagnification of the camera and collimator optics delivers slightly over 2 pixels sampling of the fiber diameter in the spatial dimension, but the spectra are slightly undersampled in the blue part of the spectrum. To fully sample the spectra, the three detectors are dithered by a half pixel in the spectral dimension between exposures, which therefore are routinely taken in pairs. The measured throughput of the APOGEE-1 instrument is $20 \pm 2\%$ (Majewski et al. 2015).

At APO, the spectrograph is fed by long fibers extending from the Sloan Foundation Telescope and the NMSU 1 m Telescope, as described in Section 2.1. The NMSU 1 m Telescope is used to observe bright stars, such as previously well-characterized spectral standards and HIPPARCOS targets (Feuillet et al. 2016), when the spectrograph is not otherwise in use with the Sloan Telescope.

The APOGEE-South spectrograph at LCO is a near-clone of the APOGEE spectrograph with some slight differences. First, the mosaic VPH grating uses two panels instead of three, a simplification with negligible impact on the net instrument throughput. Nevertheless, the pair of panel exposures were not perfectly aligned; therefore, an optical wedge is added to compensate for this misalignment to optimize spectral resolution. Second, the spectrograph optical bench is mounted within the instrument cryostat with greater consideration of seismic events, given its location in Chile. Other more minor modifications in the optical bench and cryostat configuration have been adopted as well.

We anticipate that the data from the second spectrograph will be, in most respects, quite similar to those from the original. The fibers will typically have lower sky backgrounds because

they subtend a smaller angular size. In addition, the du Pont optical correctors have less loss in the H band, which is $\sim 40\%$ on the Sloan Foundation Telescope.

The APOGEE-South spectrograph was installed at the du Pont Telescope in 2017 February and survey operations are planned to start soon thereafter.

4.4. APOGEE-2 Targeting and Observing Strategy

APOGEE-2 continues much of the observational strategy for APOGEE-1 (Zasowski et al. 2013). Its standard targeting uses the 2MASS survey, selecting stars based on dereddened $J - K_s$. Additional information from the Optical Gravitational Lensing Experiment (e.g., OGLE-III and OGLE-IV; Udalski et al. 2008, 2015), Vista Variables in the Via Lactea (VVV: Minniti et al. 2010; Saito et al. 2012; Hempel et al. 2014), and the VVV Extended ESO Public Survey (VVVX) surveys are incorporated for certain subsamples. Dereddened magnitude limits range from $H = 12.2$ to 13.8 mag (depending on cohort, as explained below) for the bright-time observations, and are $H = 11.5$ during co-observing with MaNGA.

To estimate extinction in the disk and bulge, APOGEE-2 supplements 2MASS imaging with the Spitzer-IRAC Galactic Legacy Infrared Mid-Plane Survey Extraordinaire and extensions (GLIMPSE; Benjamin et al. 2003; Churchwell et al. 2009). Where GLIMPSE data are not available, APOGEE-2 uses data from the all-sky *WISE* mission (Wright et al. 2010). The reddening estimates employ the Rayleigh–Jeans Color Excess method (Zasowski et al. 2009; Majewski et al. 2011).

To efficiently separate dwarfs and giants in the stellar halo, APOGEE-2 obtained Washington M and T_2 and DDO 51 stellar photometry using the Array Camera on the 1.3 m telescope of the U.S. Naval Observatory in Flagstaff, with additional data anticipated for the Magellanic Cloud targeting in the Southern survey component. In the $(M - T_2)$ versus $(M - DDO\ 51)$ color plane, dwarfs and giants lie in distinct locations, which allows relatively clean separation of these stellar classes (Geisler 1984; Muñoz et al. 2005; Zasowski et al. 2013).

To collect sufficient signals on fainter stars while still acquiring data on large numbers of brighter stars, APOGEE-1 and APOGEE-2 employ a system of "cohorts," groups of stars observed together for the same length of time. The 3-visit cohorts correspond to the brighter magnitude limits ($H = 12.2$) and the longer cohorts correspond to deeper magnitude limits (down to $H = 13.8$). Each $3°$ diameter field on the sky is observed with one or more plate designs, each of which consists of a combination of cohorts. Stars are predominantly divided into cohorts according to brightness, and observed ("visited") long enough to obtain the required S/N goals: typically S/N ~ 100 per half-resolution element for the core programs sampling Milky Way giant stars; S/N ~ 70 for some exceptional target classes such as luminous stars in Local Group dSph and the Magellanic clouds; and S/N ~ 10 for RR Lyrae in the bulge. For example, in a 12-visit field, "short" cohort stars are observed on 3 visits, "medium" cohort stars are observed on 6 visits, and "long" cohort stars are observed on all 12 visits. Zasowski et al. (2013) provide additional examples. Each visit corresponds to 67 minutes of exposure time in nominal conditions (see Section 4.5 for further visit details), with fields visited anywhere from 3 to 24 times.

Visits per field have cadences between 3 and 25 days. This strategy is adopted to yield detections of spectroscopic
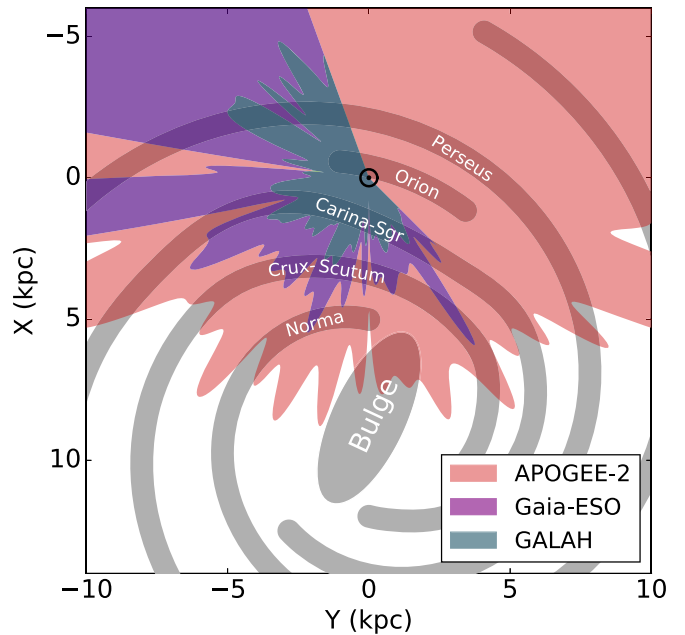

Figure 3. Map of APOGEE-1 and APOGEE-2 distance limits at $b = 0°$ within the Galactic plane, compared to other Galactic plane spectroscopic surveys. These limits assume observations of stars at the tip of the red giant branch (for solar metallicity and 2 Gyr of age) using isochrones from Bressan et al. (2012). To calculate the distance limit, we use the dust extinction prescription of Bovy et al. (2016a) and limits of $H = 12.2$ for APOGEE-2, $V = 14$ for GALAH, and $V = 19$ for *Gaia*-ESO (their faintest limit across all fields). Longer cohorts in APOGEE-2 extend correspondingly further.

variability, most commonly velocity shifts due to binary companions with a typical radial velocity precision of ~ 100–200 m s^{-1}. For stars observed more than the nominal three visits, it is possible to detect brown dwarf and planet mass companions (Fleming et al. 2015; Troup et al. 2016).

The APOGEE-2 observations are divided into northern and southern components, and each of these are sub-divided into different target classes identifying different Galactic regions or special target classes. The sky coverage is summarized in Figure 2. The target categories summarized in Table 2, providing the number of plates, visits, and stars observed in each class from respective hemispheres (N or S). All targeted stars will have observations yielding radial velocities and stellar atmospheric parameters, but, depending on the target faintness (e.g., giants in the Magellanic clouds) or type (e.g., RR Lyrae), abundance information may only be partial or unavailable, as noted.

APOGEE-2N continues observations of red giant branch (RGB) and red clump (RC) stars in the inner and outer Galactic disk, and of the stellar halo in the NGC and in the SGC. The distance limits for this sample in the Galactic plane ($b = 0°$) are shown in Figure 3. Some halo fields specifically target areas with known tidal streams; these samples are anticipated to total $\sim 58,000$ stars. Additional Galactic evolution programs target dwarf spheroidals, as well as open and globular clusters. Because it shares cartridges with MaNGA, APOGEE-2N is co-observing with MaNGA during dark time. Due to the MaNGA observing strategy, these exposures are typically three hours of integration. However, MaNGA's dithers mean a lower overall throughput (see Section 4.5) and therefore the magnitude limit in these fields is $H = 11.5$. We anticipate an additional 120,000 stars, primarily selected as red giants, in "halo" (i.e., high latitude) fields. These locations are displayed in blue in

13

Figure 2. These co-observed stars represent a substantial increase in numbers of halo stars over what was possible in APOGEE-1.

APOGEE-2 expands an ancillary APOGEE-1 program in the *Kepler* satellite Cygnus field into a main survey objective including the fields observed with the K2 mission. Two main goals focus on asteroseismology and gyrochronology targets and observations relating to *Kepler* exoplanets. The APO-KASC collaboration combines the resources of APOGEE and the *Kepler* Asteroseismology Science Consortium (KASC) to determine precise age and mass constraints on stars of a range of stellar types (Pinsonneault et al. 2014). The *Kepler* Object of Interest (KOI) program provides multi-epoch observations on five of the modules in the original *Kepler* Cygnus field, targeting KOIs to characterize planet-host versus control star properties as well as to improve our understanding of the frequency of false positives within the KOI sample. In addition to these observations of the primary *Kepler* field, APOGEE-2N is conducting a campaign of *Kepler* K2 fields, using the combined space asteroseismology/gyrochronology plus APO-GEE spectral data to determine high-quality ages for stars in a wide range of Galactic directions.

The samples listed in Table 2 complete APOGEE-2's homogeneous sampling of all Galactic regions with the RGB and RC survey. We are also targeting fainter stars from the upper RGB of the LMC, SMC, and several dSphs, and probing the chemistry of open and globular clusters. A new program observes RR Lyrae stars in the bulge from OGLE-IV and VVV to measure the detailed structure and kinematics of the ancient bulge.

Both the northern and the southern components also contain ancillary program targets with a diverse range of science goals. These programs include using low extinction windows to examine the far disk at distances of over 15 kpc in the plane, measuring Cepheid metallicities across the disk, characterizing young moving groups, determining the detailed and precision abundance trends in clusters, and studying massive AGB stars. APOGEE is also conducting an extensive cross-calibration program between APOGEE, SEGUE, GALAH, and *Gaia*-ESO, and between the APOGEE and APOGEE-South spectrographs.

4.5. APOGEE-2 Observations

APOGEE-2N utilizes the bright time at APO. Details of the division of observations across the SDSS-IV surveys at APO are given in Section 2.1. APOGEE-2S primarily utilizes the bright time at LCO, and conducts observations 75 nights each year. Section 2.2 describes the operational model; otherwise, APOGEE-2S largely employs the same observing strategies as APOGEE-2N.

Each APOGEE-2N fiber is encased in a metal ferrule whose tip is relatively narrow at 2.154 mm and is inserted fully into the plate hole, but whose base is around 3.722 mm in diameter and sits flat on the back of the plate. A buffer of 0.3 mm around each ferrule is maintained to prevent plugging difficulty. Given the plate scale on the Sloan Foundation Telescope, on the same plate no two APOGEE-2N fibers can be separate by less than 72″ on the sky. As described in Section 2.3, the APOGEE-2N holes are counterbored so that the fiber tips lie on the *H*-band focal plane.

Each APOGEE-2S fiber has a larger 3.25 mm tip and a 4.76 mm base. No buffer is used around each ferrule. Given the plate scale of the du Pont Telescope, on the same plate no two APOGEE-2S fibers can be separated by less than 52″ on the sky. Because the plate is curved to match the *H*-band focal plane at LCO, there is no counterboring of the APOGEE-2S plates.

Each plate is designed for a specific hour angle of observation. The observability window is designed such that no image falls more than 0″.3 from the fiber center during guiding. These limits on the LST of observation are slightly larger than for eBOSS because APOGEE-2 operates in the near-infrared where the refraction effects are smaller. In addition, for APOGEE-2N, we add 30 minutes on either side to ease scheduling constraints.

An APOGEE-2 visit typically consists of eight 500 s exposures taken in two ABBA sequences (a total of 66.7 minutes), where A and B are two detector dither positions in the spectral dimension described above to ensure critical sampling. Each exposure consists of 47 non-destructive detector reads spaced every 10.7 s. Each visit requires 20 minutes overhead in cartridge changes, calibrations, and field acquisition. Whereas in APOGEE-1 and the beginning of APOGEE-2, we had a fixed number of exposures per visit, starting in 2016 we have adapted the number of exposures based on the accumulated signal-to-noise ratio relative to the requirement, as eBOSS and MaNGA do. This change allows more efficient use of resources; initial estimates from the first few months indicate that the net increase in the survey completion rate is significant (roughly 15%).

During MaNGA time, APOGEE fibers are placed on APOGEE-2 targets. The MaNGA observations are dithered on the sky and their schedule constrains the APOGEE exposures to have 10% shorter exposure times than the standard APOGEE exposures. Both of these effects lead to a net throughput reduction per exposure of almost a factor of two; a reduction of about 40% due to the offset under typical seeing, and about 10% more due to the shorter exposure times. In some cases, the MaNGA-led observing yields more than the standard number of APOGEE exposures per field, but this is generally insufficient to compensate for the reduced throughput per exposure. As a result, the faint limit for targets on the MaNGA-led co-observing plates is chosen to be ∼0.7 mag brighter than it is for standard APOGEE plates (*H* < 11.5 instead of *H* < 12.2), so that the standard APOGEE signal-to-noise ratio requirement is met for targets in the MaNGA fields.

4.6. APOGEE-2 Data

The APOGEE-2 spectroscopic data consist of $R \sim 22,500$ spectra in the *H* band (1.51 μm < λ < 1.70 μm), at high signal-to-noise ratio (>100 pixel^{-1}) for most targets (Majewski et al. 2015). From these data, we determine radial velocities, stellar parameters, and abundances. García Pérez et al. (2016), Holtzman et al. (2015), and Nidever et al. (2015) describe the APOGEE data processing pipelines. The fundamentals remain unchanged for APOGEE-2, and are summarized below.

The APOGEE Quicklook pipeline (apogeeql) analyzes the observations during each exposure to estimate the signal-to-noise ratio and make decisions about continuing to subsequent exposures. The observers use these data but they are not used for scientific analysis.

Each morning, the APOGEE Reduction Pipeline (APRED) produces spectra for each new visit for the observed plates, extracting individual spectra (Horne 1986). Multiple exposures

taken on the same night are combined into "visit" spectra. In most cases, multiple visits are made to each star, sometimes with the same plate and sometimes with multiple plates. APOGEE-2 measures radial velocities from each visit spectrum, aligns the spectra in their rest frame, and creates a combined spectrum.

The APOGEE Stellar Parameters and Chemical Abundance Pipeline (ASPCAP) analyzes the combined spectrum. This pipeline divides each spectrum by a pseudo-continuum, and then performs two analyses. First, ASPCAP determines the key stellar parameters influencing the spectrum—effective temperature (T_{eff}), surface gravity ($\log g$), overall scaled-solar metal abundance [M/H], α-element abundance [α/M], carbon abundance [C/M], and nitrogen abundance [N/M]—via optimization against a set of large, multidimensional libraries of synthetic spectra (Zamora et al. 2015). ASPCAP uses the FERRE[130] code to minimize χ^2 differences between the pseudo-continuum-normalized spectrum and synthesized stellar spectra interpolated from a precomputed grid (Allende Prieto et al. 2006). The synthetic spectra used in ASPCAP are computed using the model atmospheres described by Mészáros et al. (2012) based on the ATLAS9[131] (Kurucz 1979) or MARCS[132] (Gustafsson et al. 2008) model atmospheres. These models consider variations in carbon and the α elements of ± 1 dex from the solar abundance ratios. In DR13 and DR14, the radiative transfer calculations are performed with the code Turbospectrum (Alvarez & Plez 1998; Plez 2012). This code differs from the code ASSϵT (Koesterke 2009) used in DR12, and includes an upgrade of the H-band atomic and molecular line lists presented by Shetrone et al. (2015). In the fitting, we usually tie the micro-turbulence (v_{micro}) to the surface gravity. In the models, oxygen abundance is taken to scale with α.

Second, ASPCAP performs a detailed chemical abundance determination, conducting a series of one-dimensional parameter searches for a set of 15 elements (C, N, O, Na, Mg, Al, Si, S, K, Ca, Ti, V, Mn, Fe, and Ni). For each element, a set of weighted regions of the pseudo-continuum-normalized spectrum is compared to the models (García Pérez et al. 2016). The same underlying stellar parameter grid is used for these searches as for the stellar parameter determination. In each case T_{eff}, $\log g$, and v_{micro} are fixed; only one metallicity parameter is varied. For C and N, the [C/M] and [N/M] dimensions are varied, respectively; for O, Mg, Si, S, Ca, and Ti, the [α/M] dimension is varied; for Na, Al, K, V, Mn, Fe, and Ni, the [M/H] dimension is varied. The spectroscopic windows defined by García Pérez et al. (2016) are designed such that the procedure in each case is sensitive primarily to the variation in the desired element; the precise windows have changed since DR12. Additional elemental abundances can be estimated from the spectra and ASPCAP is being developed over time to incorporate these.

The ASPCAP pipeline abundances are calibrated in several ways to minimize systematic errors both internally and with respect to other abundance scales. An internal temperature-dependent calibration of the raw abundances returned by ASPCAP is derived using the assumption that abundances within open clusters and first-generation stars in globular clusters (apart from C and N in giants) are homogeneous (De Silva et al. 2006, 2007). Some elements show temperature-

dependent abundance trends that are removed by this calibration. To improve the external accuracy, APOGEE-2 applies an external correction that sets the median abundances of solar metallicity stars ($-0.1 <$ [M/H] < 0.1) near the solar circle to have solar abundance ratios; this differs from DR12, where no external correction was applied to quantities other than [M/H]. After this calibration, most abundances have a typical precision near 0.05 dex, though uncertainties for some elements with just a few weak lines can be considerably larger; in detail, the precision is a function of effective temperature, metallicity, and signal-to-noise.

The top panel of Figure 4 displays several spectra of varying metallicities from APOGEE-2 along with the best-fit ASPCAP model. The bottom panel presents the distribution of several abundance ratios within the sample.

The first SDSS-IV data release (DR13; 2016 July) contains a rereduction of APOGEE-1 data through the latest version of the pipeline. In DR14 (summer 2017), the first two years of APOGEE-2 data will be released.

5. MaNGA

5.1. MaNGA Motivation

MaNGA is gathering two-dimensional optical spectroscopic maps (integral field spectroscopy) over a broad wavelength range for a sample of 10,000 nearby galaxies. In contrast, the original SDSS Legacy survey of the nearby galaxy population, and all similar efforts of similar scope to it, obtained single-fiber spectroscopy. Single fiber spectroscopy constrains the ionized gas content, stellar populations, and kinematics of each galaxy, but only averaged over one specific (typically central) region. These surveys revealed in broad terms how the properties of galaxies, including their stellar mass, photometric structure, dynamics, and environment, relate to their star-formation activity and its bimodal distribution. However, to fully understand how galaxy growth proceeds, how star formation ends, and how the assembly process shapes the final observed galaxy properties, detailed mapping of gas and stellar structure across the entire volume of each galaxy is required. MaNGA's integral field spectroscopic data allows study and characterization of the spatial distribution of stars and gas as well as of the detailed dynamical structure, including rotation, non-circular motions, and spatial maps of higher moments of the velocity distribution function.

MaNGA is the latest and most comprehensive of a series of integral field spectroscopic galaxy surveys of ever-increasing size. The Spectrographic Areal Unit for Research on Optical Nebulae (SAURON; de Zeeuw et al. 2002), DiskMass (Bershady et al. 2010), ATLAS^{3D} (Cappellari et al. 2011), and the Calar Alto Legacy Integral Field Area Survey (CALIFA; Sánchez et al. 2011) have created a total sample of around 1000 well-resolved galaxies. The Sydney-AAO Multi-object Integral field spectrograph (SAMI; Croom et al. 2012) survey is now operating at the Anglo-Australian Observatory and plans to observe 3400 galaxies.

MaNGA's distinguishing characteristics in this context are as follows. First, it is the largest planned survey. Relative to CALIFA and ATLAS^{3D}, the larger sample sizes of both MaNGA and SAMI are made possible through multiplexing; by having multiple, independently positionable IFUs across the telescope field of view, both surveys are able to observe more than one galaxy at once, and hence dramatically increase

---

[130] http://github.com/callendeprieto/ferre
[131] http://www.iac.es/proyecto/ATLAS-APOGEE/
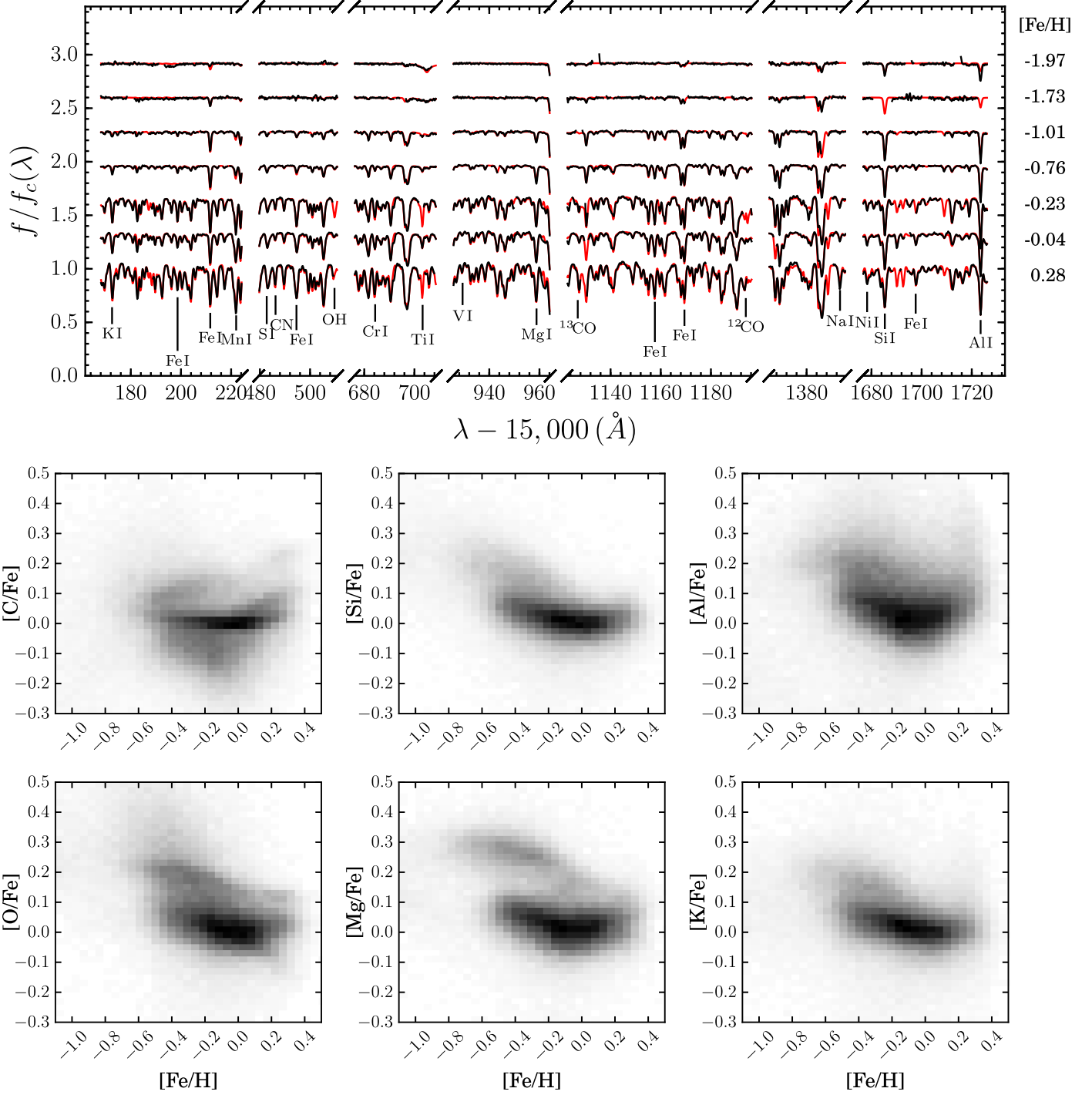[132] http://marcs.astro.uu.se

Figure 4. Top panel: several subregions of the full APOGEE spectra for seven stars of a range of metallicities, as labeled on the right (plotted using the software described in Bovy 2016). The black lines are the data; the red lines are the best-fit ASPCAP model; and the areas where the data are missing are masked due to sky contamination or other issues. Both data and model have been normalized to the pseudo-continuum $f_c(\lambda)$ (Holtzman et al. 2015). Clean, strong lines identified by Smith et al. (2013) are labeled. Bottom panels: elemental abundances relative to Fe for several of the species whose lines exist in the top panel, as a function of [Fe/H], for the APOGEE DR13 sample of 164,562 stars. APOGEE-2 can examine the major patterns as a function of Galactic location (e.g., Nidever et al. 2014; Hayden et al. 2015).

survey speed. A consequence of requiring all targets to be contained within the telescope field of view is that both MaNGA and SAMI target more distant objects than SAURON or CALIFA, and achieve lower physical resolution. Second, MaNGA uses the BOSS spectrograph, which has broader wavelength coverage than SAMI, CALIFA, or previous surveys. MaNGA is the only large integral field survey with

spectroscopic coverage out to 1 μm to allow coverage of the calcium triplet and iron hydride features informative of stellar populations, and [S III] emission lines from ionized gas. Third, MaNGA covers the radial scale of galaxies in a uniform manner regardless of mass or other characteristics; one-third of MaNGA galaxies have coverage to at least $2.5R_e$ and two-thirds have coverage to at least $1.5R_e$ (R_e is equivalent to the

half-light radius for any profile shape). Finally, MaNGA has statistically well-defined selection criteria across galaxy mass, color, environment, and redshift.

5.2. MaNGA Science

The primary science goal of MaNGA is to investigate the evolution of galaxy growth. It is designed to supply critical information for addressing four questions. (1) How are galaxy disks growing at the present day and what is the source of the gas supplying this growth? (2) What are the relative contributions of stellar accretion, major mergers, and secular evolution processes to the present-day growth of galactic bulges and ellipticals? (3) How is the shutdown of star formation regulated by internal processes within galaxies and externally driven processes that may depend on environment? (4) How is mass and angular momentum distributed among different components and how has their assembly affected the components through time?

MaNGA's resolved spectroscopy provides critical observations to address these questions. The stellar continuum of the galaxies reveals the star-formation history and stellar chemistry (e.g., Thomas et al. 2003). Nebular emission characterizes active galactic nuclei, star formation, and other processes (e.g., Osterbrock & Ferland 2006). When star formation dominates the emission, line fluxes and flux ratios indicate the rate of star formation and the metallicity of the ionized gas around the stars (e.g., Tremonti et al. 2004). Both nebular emission and stellar light provide key dynamical information related to the mass and mass profile of the galaxies (e.g., Cappellari 2008; Li et al. 2016).

The MaNGA hardware and survey are designed with the aim to constrain the distribution of physical properties of galaxies by gathering a sample large enough to probe the natural variation of these properties in the three dimensions of environment, mass, and galaxy star-formation rate. The sample size (10,000 galaxies) is justified by the desire to resolve the variation of galaxy properties in six bins in each of these three dimensions with about 50 galaxies in each bin. This number of galaxies per bin is sufficient such that differences between bins can be determined accurately.

The major areas of study for MaNGA follow from and map into the four science questions above.

1. Growth of galaxy disks, through the determination of star-formation rate surface densities and gas metallicity gradients.
2. Quenching of star formation, through star-formation rates and star-formation history gradients.
3. Assembly of bulges and spheroids, through star-formation histories and metallicity and abundance gradients.
4. The distribution and transfer of angular momentum in the stellar and gas components.
5. Weighing galaxy subcomponents, using the dynamically determined masses (from both gas and star kinematics) and the stellar masses.

The MaNGA exposure times are designed to achieve sufficient signal-to-noise ratio spectra to address these questions. The driving requirements on exposure time are the precision requirements at $1.5R_e$ on star-formation rates (0.2 dex per spatial resolution element), stellar population ages, metallicities, and α-abundances (0.12 dex when averaged over an annular ring), and dynamical mass determinations (10%).

When these goals are achieved, other precision requirements on ionized gas and stellar population properties necessary to study the above questions are typically satisfied. For the majority of galaxies in the MaNGA sample, these requirements are met by achieving the signal-to-noise ratio criteria described below (Section 5.5).

5.3. MaNGA Hardware

Drory et al. (2015) describe the MaNGA fiber bundle technology in detail. This technology allows precise hex-packed bundles of optical fibers to be fed to the BOSS spectrograph. As described in Section 2.1, for each of six cartridges there are 17 fiber bundles, 12 7-fiber minibundles used for standard stars, and 92 single fibers for sky. The 17 large bundles are normally used to target galaxies and have a range of sizes tuned to the MaNGA target galaxy distribution; there are 2 19-fiber bundles, 4 37-fiber bundles, 4 61-fiber bundles, 2 91-fiber bundles, and 5 127-fiber bundles. Each fiber has a 120 μm active core (2″ on the sky); in addition, there are 6 μm of cladding and 9 μm of buffer, for a total diameter of 150 μm, which defines the hexagonal spacing. When deployed, the fiber system has high throughput (97% ± 0.5% in lab throughput tests). Each fiber has a focal ratio degradation that is small and is equivalent to the BOSS single-fiber system. The overall throughput is improved slightly relative to BOSS through the use of antireflective coatings.

Each fiber bundle has associated sky fibers. Minibundles have a single sky fiber, 19-fiber and 37-fiber bundles have two, 61-fiber bundles have four, 91-fiber bundles have six, and 127-fiber bundles have eight. These sky fibers are constrained physically to be placed in holes within 14′ of their associated IFU. This configuration leads to sky fibers always being available close to the science fibers both on the focal plane and on the BOSS slit head (see Law et al. 2016).

5.4. MaNGA Target Selection

Wake et al. (submitted) describe the galaxy targeting strategy. The primary goals are to obtain a statistically representative sample of 10,000 galaxies with uniform spatial coverage, an approximately flat distribution in $\log M_*$, and the maximum spatial resolution and signal-to-noise ratio with these constraints. To ensure that the sample definition is simple and fully reproducible, selection functions are defined in redshift, rest-frame r-band absolute magnitude, rest-frame $g - r$ color, and (for the color-enhanced sample) rest-frame NUV $-i$ color only.

MaNGA selects galaxies from the NASA-Sloan Atlas (NSA; Blanton et al. 2011), which is based on the Main Galaxy Sample of Strauss et al. (2002) but includes a number of nearby galaxies without SDSS spectroscopy and incorporates better photometric analysis than the standard SDSS pipeline. The version of NSA used (v1_0_1) is limited to galaxies with $z < 0.15$. For selection and targeting purposes, R_e is defined in the MaNGA survey as the major-axis elliptical Petrosian radius in the r band. Galaxies are matched to IFUs of different size based on this R_e value and the effective size of the IFU.

MaNGA target selection is limited to the redshift range $0.01 < z < 0.15$. We seek an approximately flat stellar mass distribution, and to cover most galaxies out to a roughly uniform radius in terms of R_e. Achieving these goals requires targeting more luminous, and consequently intrinsically larger,
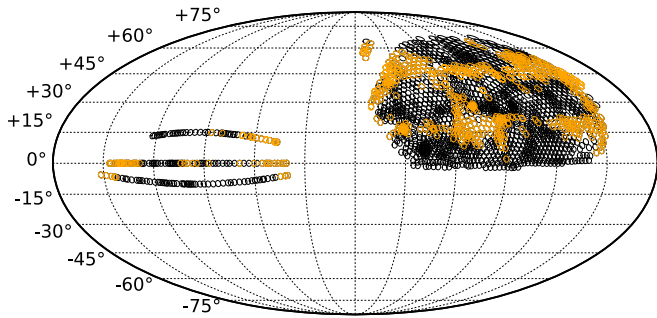
Figure 5. Planned MaNGA spectroscopic footprint in equatorial coordinates, centered at $\alpha_{J2000} = 270°$, with east to the left. Black shows the available MaNGA tiles; orange indicates example coverage for a simulated SDSS-IV MaNGA survey.

galaxies at larger redshifts. MaNGA defines three major samples across the footprint of the Main Sample of galaxies from the SDSS-II Legacy Survey; about one-third of this full sample is targeted for observation. The observed sample is to include the following.

1. 5000 Primary galaxies: selected in a narrow band of rest-frame i-band luminosity and redshift such that 80% have coverage out to $1.5R_e$.
2. 1700 Color-enhanced galaxies: selected according to i-band luminosity and redshift as for Primary, but with a well-defined upweighting as a function of NUV $-i$ color to better sample the rarer colors. The Primary and the Color-enhanced sample together are referred to as the Primary+ sample.
3. 3300 Secondary galaxies: selected in a band of rest-frame i-band luminosity and redshift, somewhat higher redshift relative to Primary, such that 80% have coverage out to $2.5R_e$.

The Primary sample has a median redshift of $\langle z \rangle \sim 0.03$, whereas the Secondary sample is at a larger median redshift $\langle z \rangle \sim 0.05$.

These targets are defined over most of the 7800 deg^2 area of the SDSS Main Galaxy Sample, which is a large contiguous region in the NGC and three $2°.5$ stripes in the SGC. Since the density of MaNGA target galaxies varies substantially over the sky, Wake et al. (submitted) have designed the potential field locations to adjust to cover the dense regions more densely, using a version of the algorithm described by Blanton et al. (2003). Figure 5 shows these potential locations as black circles (each $1°.5$ in radius). As in eBOSS, each pointing is referred to as a tile, which is typically associated with a single physical plate. MaNGA will be able to observe about one-third of the available tiles during its six years of operations. Figure 5 shows a simulated projection of this coverage (depending on weather patterns).

For each plate, minibundles are associated with standard stars, which are F stars selected similarly to those in eBOSS and are used for spectrophotometric calibration (Yan et al. 2016). The sky fibers associated with each bundle are assigned to locations that are empty in SDSS imaging.

In addition, MaNGA is targeting a set of ancillary targets observed in fields for which the above samples do not use all the bundles. These ancillary samples are described in the data release papers (e.g., for DR13 in SDSS Collaboration et al. 2016).

5.5. MaNGA Observations

MaNGA utilizes approximately 50% of the dark time at APO. Details of the division of observations across the SDSS-IV surveys are given in Section 2.1.

Each MaNGA fiber bundle is encased in a small metal ferrule 20 mm in length, which protects the bundle and contains a pin for keeping the ferrule in constant alignment on the plate. The resulting ferrule is 7 mm in diameter, larger than that for individual eBOSS or APOGEE-2 fibers. This constraint prevents two fiber bundles on the same plate from being closer than about $116''$.

The fiber bundles do not optimally sample the typical atmospheric and telescope point-spread function. To provide better sampling, each plate is observed in a set of three successive 15 minute exposures offset from each other by $1''.44$ in a triangular pattern on the sky (Law et al. 2015). Typically, these dithered exposures are all taken in succession to make sure a full set exists for each plate and night.

Each plate is designed for a specific hour angle of observation and is observable over a certain visibility window, as described in Law et al. (2015). The window is defined according to how quickly the position of the IFU shifts in sky coordinates due to differential refraction across the field (accounting for the telescope's guiding adjustments). The condition is that the maximum shift at any wavelength for an IFU at any location on the plate over an hour duration is $0''.5$ or less. If a dither set is begun within any part of the observing window, all subsequent dithers must be taken at similar hour angles in order to be combined, such that they are all within an hour of each other (the data do not have to be taken on the same night).

MaNGA requires a signal-to-noise ratio of 5 Å^{-1} fiber^{-1} in the r-band continuum at a Galactic extinction corrected r-band surface brightness of 23 mag arcsec^{-2} (AB magnitude; Oke & Gunn 1983). This goal is achieved by setting a threshold for determining whether the plate is complete as follows for the blue and red BOSS spectrograph data. We do so using the $(S/N)^2$ per spectroscopic pixel summed across exposures. A plate is deemed complete when this $(S/N)^2$ exceeds a threshold at a fiducial g_{fiber2} and i_{fiber2} (these are magnitudes from SDSS DR13 imaging (Ahn et al. 2012) within a $2''$ diameter aperture convolved with $2''$ FWHM seeing). For Galactic extinction corrected $g_{fiber2} = 22$, the threshold is $(S/N)^2 > 20$ in the blue spectrograph. For Galactic extinction corrected $i_{fiber2} = 21$, the threshold is $(S/N)^2 > 36$ in the red spectrograph. Typically three sets of dithers (nine total exposures) are required for completion; in regions of greater Galactic extinction more than three sets are required. Usually, only two sets can be taken in succession while still satisfying the hour-angle criteria described above. Observations of the same plate are therefore typically split across nights.

For some sets, if the observing conditions are changing rapidly, some dithers are good quality but others are not. The good-quality dithers in this situation are considered "orphan" exposures since they cannot be easily combined with exposures in other sets. These good exposures are processed but are not included in the reconstructed data cubes because they would lead to non-uniform images. Major changes in the reduction procedure might allow a more efficient use of these otherwise good-quality observations. Doing so is not in the pipeline development plans; nevertheless, the fully calibrated row-stacked spectra are available for such analysis.

In the mean, each plate requires 3.3 sets of 3 exposures, or about 2.5 hr of open shutter time. Each set requires 20 minutes overhead in cartridge changes, calibrations, and field acquisition. The orphaned exposures produce an additional 10% loss in efficiency.

In addition to the galaxy survey, MaNGA uses their IFUs for the development of a new optical stellar library (the MaNGA Stellar Library, or MaSTAR). Because MaNGA IFUs share cartridges with APOGEE fibers, during APOGEE-2N time the MaNGA IFUs are placed on MaSTAR targets. These observations are not dithered. The MaSTAR library provides several advantages over existing libraries. Totaling around 6000 stars, MaSTAR is several times larger than previous efforts, including those few that span a comparable spectral range, e.g., STELIB (Le Borgne et al. 2003) or INDO-US (Valdes et al. 2004). Its target selection utilizes stellar parameter estimates from APOGEE-1 (García Pérez et al. 2016), SEGUE (Allende Prieto et al. 2008), and LAMOST (Lee et al. 2015) to better cover underrepresented ranges of parameter space of effective temperature, surface gravity, metallicity, and abundance. While the Milky Way imposes certain practical limits, say, on the available dynamic range in age and abundance, there are known significant gaps in parameter coverage, e.g., at low temperatures for both dwarfs and giants, and at low metallicity, that MaSTAR is able to fill. While SEGUE (Yanny et al. 2009) sampled a large number of stars over a range of spectral types and surface gravities, their goal of broadly studying the kinematics and stellar populations of our Galaxy did not lead to an adequate sampling of some of these regions of parameter space where stars in the Milky Way are rare in the magnitude ranges probed. MaSTAR is the first stellar library of significant size with wavelength coverage from 3600 Å to beyond 1 μm. Finally, for the purposes of stellar population synthesis of MaNGA galaxies, using an empirical library with the same instrument minimizes systematics in resolution mismatch and offers significant improvements and consistency in spectrophotometry.

5.6. MaNGA Data

MaNGA spectroscopic data consists of $R \sim 2000$ spectra in the optical (approximately 3600 Å $< \lambda <$ 10350 Å), at signal-to-noise ratios of at least 5 per pixel, spatially resolved across galaxies at $\sim 2\farcs5$ resolution FWHM, from which we create maps of velocities, velocity dispersion, line emission, and stellar population indicators. MaNGA data are processed using a pipeline derived from and similar to that used for eBOSS, and utilizing similar infrastructure.

MaNGA data are processed through a quicklook pipeline (Daughter Of Spectro; DOS) during each observation to estimate the signal-to-noise ratio in real time and make decisions about continuing to subsequent exposures. Quality assurance plots are studied each day to identify unexpected failures of the observing system or pipelines.

A Data Reduction Pipeline (DRP; Law et al. 2016) reduces the single fibers in each exposure into individual spectra using optimal extraction. This pipeline is similar to and shares a code base with the pipeline that processes BOSS spectrograph data (Bolton et al. 2012). There is a subtle difference in the sky estimation. As in BOSS and eBOSS, all fibers are used to define the model sky spectrum; however, this model spectrum can be scaled in the DRP to match the local sky background near each IFU. A second and more fundamental difference is

the spectrophotometric calibration procedure. An important factor in the single-fiber eBOSS spectrophotometric calibration is the wavelength-dependent loss due to atmospheric differential refraction (ADR; for a detailed discussion, see Margala et al. 2016). However, for MaNGA, this effect is better interpreted as a variation with wavelength of the effective location of the fiber center on the sky; i.e., the blue light samples a slightly different part of the galaxy than the red light. Loosely speaking, light is no longer "lost" from a given fiber due to ADR, but instead shifted toward a neighboring fiber. Thus, the spectrophotometric correction should not include ADR losses. As Yan et al. (2016) describe, the correction is performed using standard stars observed through 7-fiber minibundles, which allow for the geometric effects to be disentangled from the effective throughput of the system. The DRP produces a set of wavelength and flux calibrated "row-stacked spectra" for each exposure.

In the second stage of processing, the DRP associates each fiber in a given exposure with its effective on-sky location using the as-measured fiber bundle metrology in combination with the known dither offsets and a model for the ADR and guider corrections. This astrometry is further refined on a per-exposure basis by comparing the fiber fluxes to reference broadband imaging in order to correct small rotations and/or offsets in the fiber bundle location from the intended position. The DRP then uses a flux-conserving variation of Shepard's method (Sánchez et al. 2012) to interpolate the row-stacked spectra onto a three-dimensional data cube with regularly spaced dimensions, one in wavelength and two Cartesian spatial dimensions. Details on the DRP can be found in Law et al. (2016).

Based on the row-stacked spectra and data cubes, a Data Analysis Pipeline (DAP) calculates maps of derived quantities such as Lick indices (e.g., Worthey et al. 1994), emission-line fluxes, and kinematic quantities such as gas velocity, stellar velocity, and stellar velocity dispersion. The list of calculated quantities remains under development. Future plans for DAP include deriving high-level quantities such as stellar mass and abundance maps, metallicity maps, and kinematic models.

Figure 6 shows some typical MaNGA data for UGC 02705, for which observations through a 127-fiber bundle finished on 2014 October 26.

The first SDSS-IV data release (DR13; 2016 July) contains MaNGA results data taken through 2015 July. In DR14, the MaNGA data through 2016 May will be released.

6. eBOSS, TDSS, and Spiders

eBOSS, TDSS, and SPIDERS are three surveys conducted simultaneously at APO on the 2.5 m telescope during dark time using the 1000 single-fiber configuration with the BOSS spectrograph. The overall survey strategy is driven by eBOSS, which is the largest program. TDSS and SPIDERS each use approximately 5% of the fibers on each eBOSS plate. Table 3 summarizes the three programs.

6.1. eBOSS

6.1.1. eBOSS Motivation

eBOSS is conducting cosmological measurements of dark matter, dark energy, and the gravitational growth of structure. Current data from other large-scale structure measurements, Supernovae Type Ia, and the cosmic microwave background
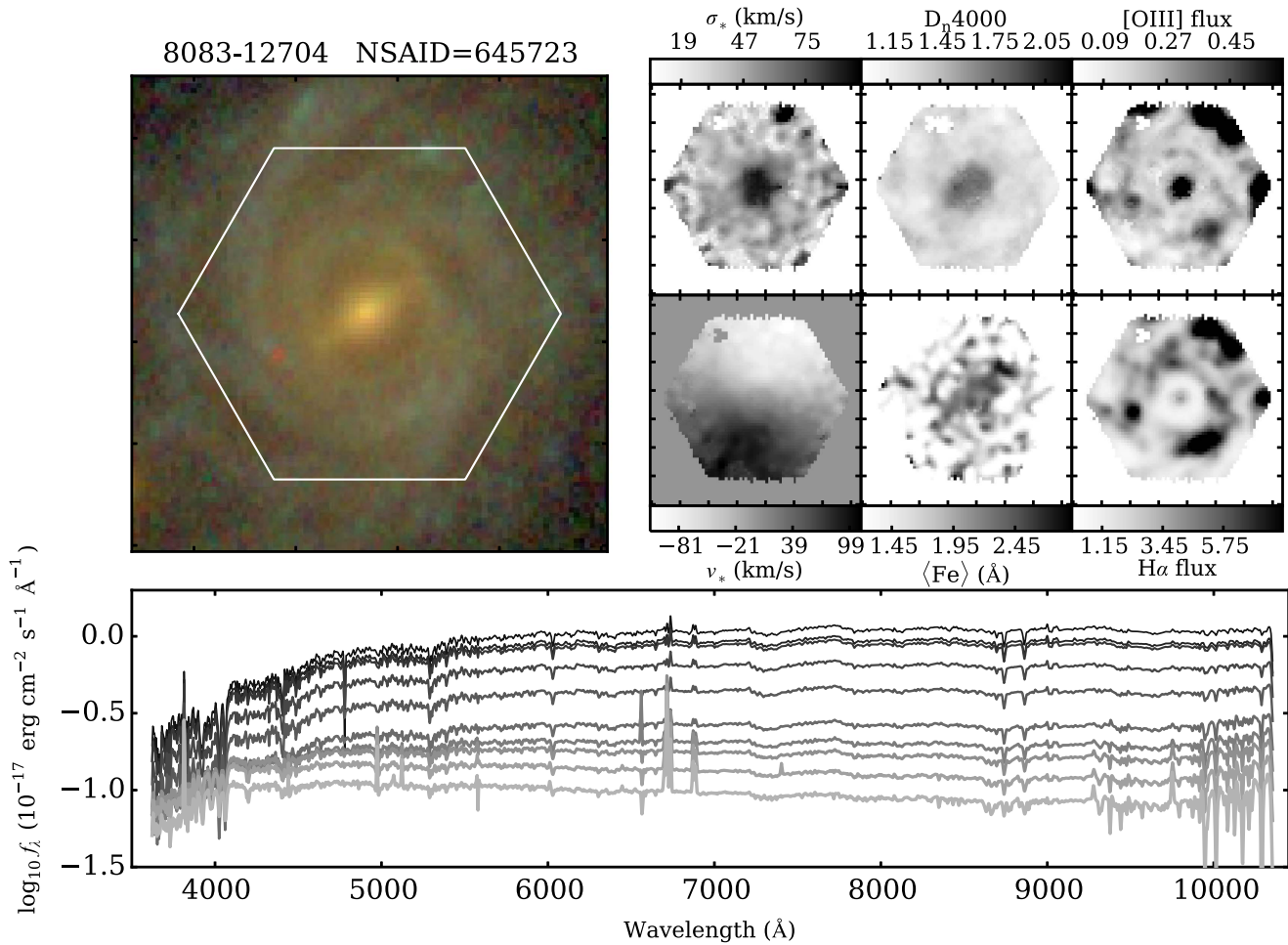
8083-12704   NSAID=645723

Figure 6. Top left: image of a MaNGA target (UGC 02705) from SDSS, with MaNGA 127-fiber bundle footprint overlaid ($37'' \times 37''$). Top right: maps of derived quantities from the DAP pipeline: stellar velocity dispersion σ_*, stellar mean velocity v_*, the stellar population age indicator D_n4000, the metallicity indicator $\langle Fe \rangle = 0.5(Fe5270 + Fe5335)$, the [O III] $\lambda 5007$ flux in 10^{-17} erg cm^{-2} s^{-1}, and the Hα flux in the same units. Bottom: sum of MaNGA spectra in elliptical annuli of increasing radii.

Table 3
Target Classes in eBOSS, TDSS, and SPIDERS

Program	Target Class	Area (deg^2)	Spectra
eBOSS	LRG	7500	266,000
eBOSS	New Quasar tracers	7500	400,000
eBOSS	Total Quasar tracers	7500	500,000
eBOSS	New Lyα quasars	7500	60,000
eBOSS	Repeat Lyα quasars	7500	60,000
eBOSS	ELG	1000–1500	200,000
eBOSS	"Contaminants"[a]	7500	320,000
TDSS	PS1/SDSS Variables (total)	7500	200,000
TDSS	Few-epoch spectra	7500	10,000
TDSS	Repeat quasar spectra	1000–1500	16,000
SPIDERS	Point sources (total)	7500	22,000
SPIDERS	Cluster galaxies (total)	7500	60,000

Note.
[a] High-quality redshifts outside the range of interest.

are consistent with a spatially flat cold dark matter model and a cosmological constant (ΛCDM; Weinberg et al. 2013; Aubourg et al. 2015). The cosmological constant or some other mechanism is required due to the observed late-time

acceleration in the cosmic expansion (e.g., Riess et al. 1998; Perlmutter et al. 1999).

The cosmological constant can be generated through a nonzero, but very small, vacuum energy density; however, the particle physics mechanism to generate this level of vacuum energy is unknown. The acceleration could also be caused by some more general fluid with negative pressure, referred to typically as "dark energy;" the equation of state of this fluid is constrained to be fairly similar to that of the vacuum energy. Alternatively, the acceleration may be caused due to modifications of general relativity that affect gravity at large scales (e.g., Randall & Sundrum 1999; Dvali et al. 2000; Sahni & Shtanov 2003; Sotiriou & Faraoni 2010; Battye & Pearson 2012). Many of these explanations of the acceleration are theoretically plausible, and the challenge is to observationally bound the possibilities. One critical constraint arises from precisely measuring the rate of expansion and gravitational growth of structure throughout all cosmic epochs.

eBOSS is creating the largest volume map of the universe usable for large-scale structure to date. This data set will allow exploration of dark energy and other phenomena in epochs where no precision cosmological measurements currently exist, pursuing four key goals: BAO measurements of the Hubble parameter and distance as a function of redshift, redshift space

Table 4
Cosmological Precision in eBOSS

Target Class	z	σ_H/H	σ_{D_A}/D_A	σ_R/R	$\sigma_{f\sigma_8}/f\sigma_8$ [a]
LRG [b]	0.71	0.025	0.016	0.010	0.025
ELG [c]	0.86	0.050	0.035	0.022	0.034
Quasar	1.37	0.033	0.025	0.016	0.028
Lyα	2.54	0.014	0.017	…	…

Notes. Results derived from Zhao et al. (2016).
[a] $f\sigma_8$ forecasts use assumptions similar to the model-independent constraints cited in Section 6.1.2, holding other cosmological parameters fixed.
[b] Includes LRGs observed in SDSS-III within the overlapping redshift range.
[c] Numbers correspond to the "high density" ELG sample in Zhao et al. (2016), which is close to the current plan.

distortion measurements of the gravitational growth of structure, constraints on and possible detection of the neutrino mass sum, and constraints on inflation through measurements of non-Gaussianity.

Among currently operating experiments, only the Hobby-Eberly Telescope Dark Energy Experiment (HETDEX; Hill et al. 2008) and the Dark Energy Survey (DES; Abbott et al. 2016) will measure the universe's expansion history at comparable precision and accuracy. HETDEX is a wide-field integral field spectrograph survey that will map Lyα emitting objects at $z \sim$ 2–3. DES is an imaging survey that will measure BAO as a function of redshift using angular clustering and photometric redshifts. Future spectroscopic experiments are planned that will exceed the precision in measuring expansion of any current program. These experiments include DESI (Levi et al. 2013) and the Prime Focus Spectrograph at *Subaru* (PFS; Takada et al. 2014). eBOSS's large-scale structure results precede the beginning of either of these experiments and is poised to deliver the first accurate measurements of expansion in the redshift range $1 < z < 2$.

6.1.2. eBOSS Science

The primary cosmological constraints from eBOSS are BAO measurements of the angular diameter distance $D_A(z)$ relative to that of the CMB, and the Hubble parameter $H(z)$ as a function of redshift. Weinberg et al. (2013) includes a recent review of this technique. The LRG, ELG, and low-redshift quasar samples are used as tracers to measure BAO in large-scale structure; the high-redshift quasar sample is used for Lyα forest measurements of BAO in the neutral gas clustering. These measurements in real and redshift space yield constraints on the Hubble parameter $H(z)$ and the angular diameter distance $D_A(z)$, which can be combined into a constraint on a combined distance $R(z)$. Full details on the definition of these quantities, and projections regarding the precision on BAO from eBOSS can be found in Dawson et al. (2016) and Zhao et al. (2016). Table 4 summarizes the expected precision from the LRG, ELG, quasar, and Lyα samples. In terms of the Dark Energy Task Force (DETF) Figure of Merit (FoM; Albrecht et al. 2006), the eBOSS sample improves the FoM over the existing constraints to date by a factor of three. These projections assume only measurements of the BAO feature itself. Addition of the broadband power spectrum, redshift space distortions, and geometric distortions is expected to produce a further increase in the FoM (McDonald & Roy 2009), though with greater theoretical systematics.

Redshift space surveys, as opposed to imaging surveys, yield a unique additional constraint on cosmology; since galaxy motions reflect the gravitational growth of structure, measuring the anisotropic distortion they produce in clustering yields constraints on cosmological parameters and general relativity (GR) (Weinberg et al. 2013). In the context of cosmic acceleration, clustering measurements can distinguish between models for acceleration that rely on dark energy and those that require modified gravity (Huterer et al. 2015). This measurement yields $f\sigma_8$, where f measures the growth rate and σ_8 measures the amplitude of matter fluctuations. Currently the most robust constraints on $f\sigma_8$ are from BOSS, with large-scale model-independent constraints of $\sim$6% (9% when marginalizing over other parameters; Beutler et al. 2014; Samushia et al. 2014; Alam et al. 2015b) and model-dependent constraints on smaller scales of 2.5% (Reid et al. 2014). These critical tests distinguishing dark energy and modified gravity models are possible only with a spectroscopic redshift program such as eBOSS.

The fundamental properties of neutrinos are imprinted in the distribution of galaxies. eBOSS's large volume permits tight new constraints on, and perhaps finally allows for a measure of, the neutrino mass. Flavor oscillation measurements place lower limits on the neutrino masses of 0.05–0.10 eV depending on the model (Fogli et al. 2012). Cosmological observations place upper limits on the sum of neutrino flavor masses, due to the suppression of power by the neutrino component in fluctuations at scales smaller than 100 Mpc. The best existing cosmological constraint is that $\sum m_\nu < 0.23$ eV (95% confidence, when assuming zero curvature; Collaboration et al. 2014), from CMB measurements and BAO. Adding eBOSS constraints from the LRG, ELG, and $z < 2.2$ quasars improves this limit to $\sum m_\nu < 0.108$ eV, close to the minimum allowed neutrino mass in conventional particle physics theories. eBOSS clustering data therefore have a significant chance of measuring the neutrino mass sum, which would be a major breakthrough in fundamental physics.

eBOSS pioneers tests of cosmic inflation through the measurement of very-large-scale fluctuations. Departures from the standard inflationary scenario commonly yield small deviations from Gaussian fluctuations, quantifiable by f_{NL} (=0 for Gaussian). A natural form of non-Gaussianity (the "local" form; Wands 2010) can be tested using two-point statistics at >200 Mpc (Dalal et al. 2008). eBOSS yields the only constraints ($\sigma_{fnl} = 12$) comparable in precision to (but completely independent of) current Planck limits (local $f_{NL} = 2.5 \pm 5.7$; Planck Collaboration et al. 2016). Furthermore, galaxy bispectrum measurements have the potential to improve eBOSS constraints dramatically. Future improvements will likely be best achieved with redshift surveys such as eBOSS.

eBOSS yields the largest existing statistical sample available for a broad array of other science topics.

1. Galaxy formation and evolution through interpretation of the small-scale correlation functions (Zheng et al. 2007; Leauthaud et al. 2012; Guo et al. 2013).
2. Evolution of the most luminous galaxies out to $z \sim 1$ (e.g., Maraston et al. 2013; Bundy et al. 2015; Montero-Dorta et al. 2016).
3. Nature of the circumgalactic medium through statistical absorption studies (Steidel et al. 2010; Zhu et al. 2014, 2015).
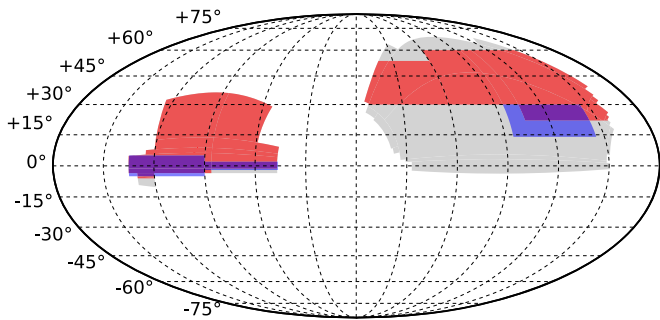
Figure 7. Planned eBOSS spectroscopic footprint in equatorial coordinates, centered at $\alpha_{J2000} = 270°$, with east to the left. Gray areas are the BOSS spectroscopic footprint, and for eBOSS red represents the planned LRG and quasar sample footprint, and blue shows the planned ELG footprint.

4. Calibration of photometric redshifts through cross-correlation; eBOSS provides this calibration for DES and validates this method for use in future surveys such as LSST (Newman et al. 2015).

5. Nature of the intergalactic medium in the range $2 < z < 3.5$, using the damped Lyα systems, Lyman limit systems , and the Lyα and Lyman-β forests and their cross-correlations with other tracers of structure. (e.g., Becker et al. 2013; Pieri et al. 2014; Lee et al. 2015). These techniques can reveal signatures of He II reionization, the clustering of ionizing sources, and can potentially detect Lyα emission.

We will discuss the quasar science in more detail in Section 6.4.

6.1.3. eBOSS Targeting Strategy

Dawson et al. (2016) presents an overview of the eBOSS targeting strategy, which aims primarily at surveying a large volume of the universe. The eBOSS footprint covers 7500 deg^2, with approximately 4500 deg^2 in the North Galactic Cap (NGC) and 3000 deg^2 in the South Galactic Cap (SGC). Luminous red galaxies (LRGs) and quasars are targeted over the full eBOSS footprint. An emission-line galaxy (ELG) sample is targeted over 1000–1500 square degrees starting in Fall 2016. A 466 deg^2 pilot program was conducted in SDSS-III and early SDSS-IV, designated the Sloan Extended Quasar, ELG, and LRG Survey (SEQUELS; Dawson et al. 2016; Alam et al. 2015a). SEQUELS tested these target selection techniques. Figure 7 shows the the currently planned eBOSS footprint, and Table 4 summarizes the planned eBOSS samples and the resulting cosmological constraints.

The targeting strategy is driven by a desire to fill the existing gap in cosmological large-scale structure measurements between $z \sim 0.6$ and $z \sim 2.5$, which is the transition from cosmic deceleration to acceleration. With existing facilities, this range cannot be covered over wide fields using a single tracer. Thus, we adopt a multi-tracer strategy: extend the BOSS LRG sample to $z \sim 0.8$, introduce an emission-line galaxy sample, which can be selected and successfully observed to $z \sim 1.1$, conduct a dense survey of quasars to $z \sim 2.2$, and enhance the BOSS quasar sample at $z > 2.2$.

The full quasar sample is designed to cover $0.9 < z < 3.5$. The quasars at redshifts $z < 2.2$ are utilized as tracers of large-scale structure themselves. The quasars at $z > 2.1$ are utilized as backlights for Lyα absorption, which measures the density
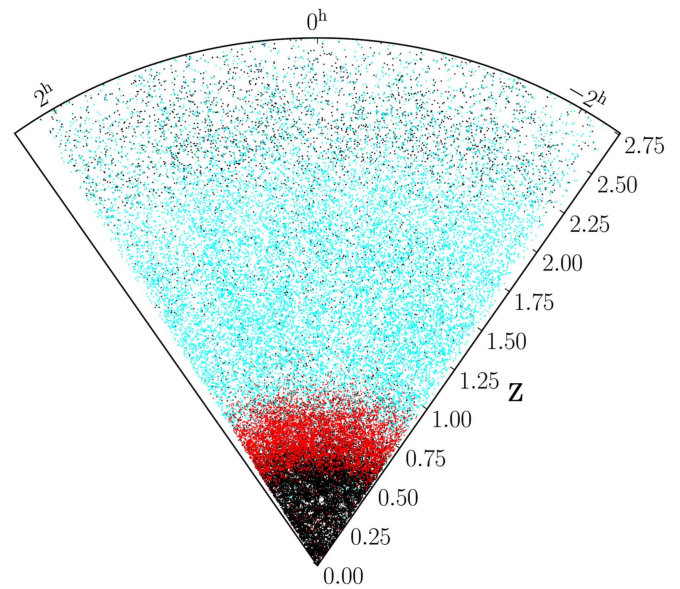

Figure 8. Slice along right ascension through the eBOSS redshift sample, 5° wide in declination and centered at $\delta = +22°$. Black points indicate previously known redshifts from SDSS-I through SDSS-III. Cyan points show eBOSS quasars and red points represent eBOSS LRGs, each category is selected as described in Section 6.1.3.

of neutral gas along the line of sight at those redshifts. The core quasar target selection is described by Myers et al. (2015), utilizing a redshift-binned version of the Extreme Deconvolution (XD) algorithm applied to quasars (XDQSOz; Bovy et al. 2011, 2012b). In the SDSS-IV case, we apply XD on the SDSS photometry and its associated uncertainties to select quasars, and then consult *WISE* photometry to veto sources likely to be stars. We do not observe quasars at $z < 2.1$ that were spectroscopically classified in prior SDSS surveys (which have a density $\sim$13 deg^{-2}), but these are included in clustering analyses. eBOSS re-observes the fainter quasars at $z > 2.1$ to improve the signal-to-noise ratio in the Lyα forest by a factor of 1.4.

The LRG sample is designed to cover $0.6 < z < 1.0$, with a median $z \sim 0.71$. eBOSS achieves this selection using a combination of SDSS r, i, and z photometry and *WISE* 3.4 μm photometry, as described by Prakash et al. (2015). The sample is limited at $z < 19.95$ (using Galactic extinction corrected SDSS model magnitudes).

The ELG sample is designed to cover $0.7 < z < 1.1$, with a median $z \sim 0.86$ (Comparat et al. 2016; Jouvel et al. 2015). The selection uses the deep g, r, and z band imaging from the Dark Energy Camera (DECam; Flaugher et al. 2012). The imaging is primarily drawn from a combination of DES imaging and of the DECam Legacy Survey (DECaLS[133]), a wide footprint extragalactic imaging survey being conducted in preparation for DESI. The ELG targets are observed at a high density ($>$180 deg^{-2}) over 1000–1500 deg^2 split about equally between the SGC and NGC. Because of the available imaging depth, the target density in the SGC is high ($\sim$240 deg^{-2}) and the efficiency of selecting ELGs in the desired redshift range is around 80%, whereas the density ($\sim$190 deg^{-2}) and efficiency (75%) are lower in the NGC. In both regions, the median redshift is similar. These targets are observed on separate plates from the LRG and quasar cosmological surveys. These plates

---

[133] http://legacysurvey.org

do not contain SPIDERS targets, but, as described in Section 6.3, they do include Repeat Quasar Spectroscopy targets. ELG observations began in Fall 2016. A future paper will describe the exact selection function, its redshift distribution, as well as systematic weights to be applied for large-scale structure analysis.

The eBOSS team also considered the use of other imaging data sets. In SEQUELS, Comparat et al. (2015) drew ELG targets from the South Galactic Cap U-band Sky Survey (SCUSS; Zou et al. 2015) and SDSS. In the last round of tests before the ELG program was finalized, Comparat et al. (2016) and Raichoor et al. (2016) combined *WISE* (Wright et al. 2010), SCUSS, and SDSS to select ELG targets. The final selection functions are nearly as efficient as the DECaLS targeting but yielded a lower effective redshift.

For the LRG, ELG, and quasar clustering samples, eBOSS aims to create uniform target selection with a maximum absolute variation (peak to peak) of 15% in the expected target number density. The expected target number density is defined with respect to its estimated dependence on imaging survey sensitivity, calibration errors, stellar density, and Galactic extinction (Myers et al. 2015; Prakash et al. 2015; Dawson et al. 2016).

The targets are assigned to plates using a descendant of the tiling algorithm adopted in the Legacy and BOSS surveys (Blanton et al. 2003). The eBOSS pointings are designed to cover large contiguous areas in the NGC and SGC. Each pointing is referred to as a tile, which typically (but not always) is associated with a single physical plate. Of the 1000 available fibers, 80 are assigned to estimate the sky and 20 are assigned to bright *F* stars used as standard sources. The TDSS and SPIDERS programs are included in the tiling assignments and observed on the same plates as the eBOSS targets.

eBOSS adopted a tiered-priority system for assigning survey targets to plates, which leads to an efficient assignment of fibers and a satisfactory level of completeness. All non-LRG targets receive maximal priority and the tiling solution must achieve 100% tiling completeness for a set of all non-LRG targets that do not collide with each other (a "decollided" set; see Blanton et al. 2003). For LRGs, eBOSS does not require full decollided completeness. Rather, the density of LRG targets intentionally oversubscribes the remaining fiber budget. The average density of LRGs assigned to fibers spectra is about 50 deg^{-2}. In areas of lower density in non-LRG targets, the LRGs can be observed up to a density of about 60 deg^{-2}. In areas of higher density in non-LRG targets, the LRGs can be incomplete; however, eBOSS does require that the total completeness of the decollided LRG targets be greater than 95%. This layered tiling scheme allows 8% more area to be covered than otherwise would, at the cost of the variable completeness of LRGs.

In the first round of fiber assignments—the non-LRG targets—eBOSS specifies the priority for fiber assignments when fiber collisions occur. Because the quasar targets have significantly higher density than TDSS and SPIDERS targets, quasar-TDSS/SPIDERS collisions are fractionally more common for TDSS/SPIDERS target classes. Collisions are resolved in the following order (highest to lowest priority): SPIDERS, TDSS, reobservation of known quasars, clustering quasars, and variability-selected quasars. Quasars found in the FIRST survey (Becker et al. 1995) and white dwarf stars that can be used as possible calibration standards are given the lowest priorities for resolving fiber collisions.

Dawson et al. (2016) summarizes the overall expected numbers of spectra. Nominal weather performance provides completion of ~1800 plates, which would yield 1.62 million object spectra including about 180,000 unique TDSS and SPIDERS targets. Table 3 lists the numbers of confirmed quasars at $z < 2.1$, new and repeated BOSS quasars at $z > 2.2$, confirmed LRGs, and confirmed ELGs, assuming our estimated efficiencies and redshift success rates. The spectra that are contaminants to the eBOSS cosmological sample are primarily blue stars for quasar targeting and M stars for LRG targeting.

6.1.4. eBOSS Observations

eBOSS utilizes approximately 50% of the dark time at APO. Details of the division of observations across the SDSS-IV surveys are given in Section 2.1.

Each BOSS fiber is encased in a metal ferrule whose tip is relatively narrow (2.154 mm) and is inserted fully into the plate hole, but whose base is 3.722 mm in diameter and sits flat on the back of the plate. Two fibers on the same plate therefore cannot be placed more closely than 62″ from each other on the sky. Thus, except where two tiles overlap, only one of such a pair can be observed; these fiber collisions affect both the small- and large-scale clustering signal from the sample and must be accounted for in the analysis (e.g., Guo et al. 2012).

Each plate is designed for a specific hour angle of observation. The observability window is designed such that no image falls more than 0″3 from the fiber center during guiding. This restriction limits the range of LSTs in which a plate is observable.

eBOSS is designed for LRGs, ELGs, and quasars with $z < 1.5$ to have a redshift accuracy <300 km s^{-1} (root mean squared) at all redshifts. Larger redshift errors have the potential to damp the BAO feature in the radial direction, thus diluting the precision achievable on $H(z)$. We require catastrophic errors (defined as redshift errors exceeding 1000 km s^{-1} that are not flagged) to be <1%. At higher redshifts, we aim for quasars to have a redshift measurement accuracy $<300 + 400(z - 1.5)$ km s^{-1}. The increase at higher redshift reflects the expected rising difficulty of accurate redshift measurement. A small number of repeat spectra are obtained where fibers are available, which allow an estimate of the uncertainties in the redshifts.

To achieve these goals, eBOSS observations are designed to obtain median *i*-band $(S/N)^2 > 22$ per pixel at a fiducial target magnitude $i_{fiber2} = 21$ and median *g*-band $(S/N)^2 > 10$ per pixel at a fiducial target magnitude $g_{fiber2} = 22$. The dispersion of the BOSS spectrographs delivers roughly 1 Å per pixel. Plates are exposed until they satisfy this signal-to-noise ratio requirement. First year data indicate that plates require 4.7 15-minute exposures to exceed these requirements; during the first year, we slightly exceeded the requirements and averaged 5.3 exposures per plate. The mean overhead per completed plate is around 22 minutes (this time averages over cases where a plate was observed on multiple nights). These thresholds are designed to satisfy the above requirements on redshift accuracy. The observing depths are also established to achieve a reliable classification of all targets, whereby catastrophic errors are required to occur at a rate of less than 1% for all target classes.
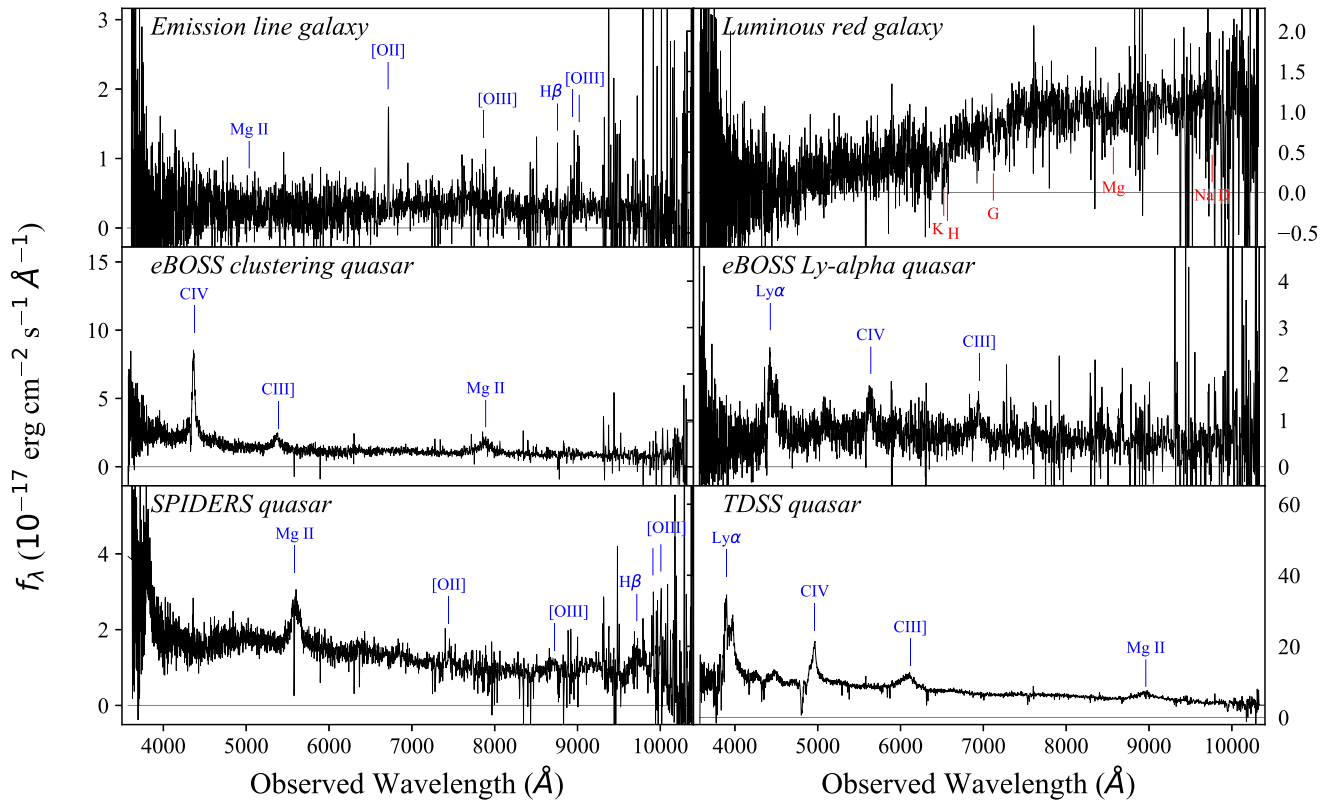
Figure 9. Six representative eBOSS spectra, showing an emission-line galaxy, a luminous red galaxy, a quasar from the core "cosmological" sample, a quasar selected at $z > 2.2$ for Lyα forest studies, an X-ray emitting quasar selected by SPIDERS, and a TDSS-selected variable broad absorption line quasar (listed left-to-right, and top-to-bottom). The locations of emission lines are labeled in blue, and for the luminous red galaxy, those of absorption features are labeled in red.

6.1.5. eBOSS Data

eBOSS spectroscopic data consists of single-fiber $R \sim 2000$ spectra in the optical (approximately 3600 Å $< \lambda <$ 10350 Å), at signal-to-noise ratios of $\sim$2–4 per pixel for most targets, from which we determine redshifts and classifications. The eBOSS pipeline is a slightly modified version of the BOSS pipeline described by Bolton et al. (2012). Figure 8 shows the redshift and right ascension for a subsample of the eBOSS sample. Figure 9 displays six example spectra from the first year of eBOSS, processed through a preliminary version of the eBOSS pipeline.

eBOSS data are processed through a quicklook pipeline (Son Of Spectro, SOS) during each observation to estimate the signal-to-noise ratio in real time and inform decisions about continuing to subsequent exposures. Quality assurance plots are examined each day to identify unexpected failures of the observing system or pipelines.

Each morning following a night of eBOSS observations the data are processed by the pipeline and made available for the collaboration. The pipeline extracts the individual spectra using optimal extraction (Horne 1986), and builds a spatially dependent model of the sky spectrum from the 80 sky fibers and subtracts that model from each object fiber. It determines the spectrophotometric calibration, which includes the telluric line correction, using a set of 20 calibrator standard stars observed on each plate, selected to have colors similar to F stars and in the magnitude range $16 < r_{\mathrm{fiber2}} < 18$. Redshifts are determined using a set of templates, with separate sets for stars, galaxies, and quasars. For stars, the templates consist of individual archetypes; for galaxies and quasars, the templates

consist of Principal Component Analysis (PCA) basis sets that are linearly combined to fit the data at each potential redshift. The best redshift and classification (star, galaxy, or quasar) is determined based on the χ^2 differences between the models and the data. For galaxies, the pipeline also fits the velocity dispersion of the galaxy, by comparing the spectra with linear combinations of a set of high-resolution stellar templates. The pipeline conducts emission-line flux and equivalent width measurements as well for a number of major emission lines.

The pipeline undergoes continuous improvement as problems are identified and repaired. Future versions will benefit from ongoing efforts to improve sky subtraction and spectrophotometric calibration. A new procedure and set of templates for fitting redshifts is being developed to handle better the lower signal-to-noise ratio of the fainter eBOSS targets. Specifically, quasars and galaxies will use a large number of fixed archetypes rather than a PCA basis set (Hutchinson et al. 2016).

The eBOSS pipeline has been applied to all SDSS-III BOSS data as well, which were taken with the same instrument. We do not have plans to reanalyze the previous SDSS-I and SDSS-II data from the SDSS spectrographs.

The first SDSS-IV data release (DR13; 2016 July) contains a rereduction of BOSS data through the latest version of the pipeline and includes plates from SDSS-IV completing the SEQUELS sample. In DR14, the first two years of eBOSS data will be released.

The quasar science team within eBOSS plans to continue to maintain the SDSS quasar catalog, the latest version of which is DR12Q (Pâris et al. 2014). This catalog includes visually vetted redshifts and classifications and has greater reliability

than the standard pipeline results. In DR12Q, all quasar spectra were inspected visually by at least two people. However, in eBOSS a greater amount of automatic vetting reduces the number of quasars that need to be inspected visually.

6.2. SPIDERS

6.2.1. SPIDERS Motivation

Within the main eBOSS program of quasars and LRGs, an average of 50 fibers per plate are allocated to sources associated with X-ray emission, primarily AGNs and cluster galaxies. The goal of these observations are twofold: first, to obtain a statistically complete sample of X-ray emitting accreting black holes to better understand quasar evolution and physics; second, to obtain redshifts and velocity dispersions for a large sample of X-ray clusters. The samples are defined using the *ROSAT* All-Sky Survey (RASS; Voges et al. 1999; Boller et al. 2016), the XMM Slew Survey (XMMSL; Warwick et al. 2012), and the upcoming eROSITA instrument (Merloni et al. 2012). In total, 22,000 spectra of X-ray emitting AGN will be acquired, about 25% of which will be targets in common with the eBOSS cosmological program, and redshifts of about 58,000 galaxies in 5000 galaxy clusters.

SPIDERS uses this X-ray census of AGNs to better understand the relationships among the growth of galaxies, the growth of their central black holes, and the growth of their dark matter halos; Section 6.4 describes these goals in more detail. The SPIDERS cluster sample better establishes cluster scaling relations and their evolution, and to use them to constrain cosmological parameters through the evolution of the cluster mass function (Allen et al. 2011; Weinberg et al. 2013). For all of these science goals, the existing statistically complete X-ray selected samples are too small; they consist primarily of the sample of RASS sources observed in SDSS-I and -II (Anderson et al. 2003) and of much narrower field of view and deeper observations in, for example, COSMOS (Cappelluti et al. 2009; Civano et al. 2016), AEGIS (Laird et al. 2009; Nandra et al. 2015), CDFS (Luo et al. 2008; Xue et al. 2011), and XBoötes (Kenter et al. 2005; Murray et al. 2005). Systematic, moderate resolution spectroscopic follow-up of large area X-ray surveys, which sample massive galaxy clusters and the bright end of the AGN luminosity function, are currently lacking, and can yield important insights into demographics, evolution, and physical characteristics of galaxies in the densest large-scale structure environments, and of AGNs, including the obscured populations.

6.2.2. SPIDERS Target Selection

eROSITA's planned launch is in early 2018 and data will become available in Fall 2018. The satellite will observe the whole sky every six months, and over four years will produce a series of eight successively deeper eROSITA All Sky X-ray Survey catalogs (eRASS:1 through eRASS:8). Given this timeline, the targeting strategy for SPIDERS is divided into several tiers depending on the available data at the time of observation.

1. *Tier 0*: Prior to the availability of eRASS data, SPIDERS targets RASS and XMMSL targets.
2. *Tier 1*: SPIDERS will begin targeting eROSITA data with eRASS:1, which will be a factor of four to five times deeper than RASS (for point sources). eRASS:1 data is

planned to be available in Fall 2018 and SDSS-IV observations can begin in early 2019.
3. *Tier 2*: eRASS:3 is planned to be available mid-2019, and SPIDERS will target it beginning late 2019.

SDSS-IV does not observe eRASS sources over the entire sky. The survey only has access to sources in the half of the sky defined in Galactic coordinates ($180° < l < 360°$). This hemisphere is accessible to the eROSITA-DE consortium, with which SDSS-IV has a data sharing agreement. Under current plans, the other half of the sky is accessible only to the Russian eROSITA consortium.

For Tier 0 point sources, RASS identifies on average $3 \deg^{-2}$, of which about $0.8 \deg^{-2}$ are not previously observed spectroscopically and not too bright to observe within an eBOSS exposure (which means, typically, $r > 17$). The uncertainty in the coordinates of each point source is about $20''$–$30''$, making the identification of optical counterparts challenging. The match to the optical counterpart is performed in two steps: (1) the *WISE* counterparts are found using a Bayesian method based on that of Budavari et al. (2009), taking into account priors in color–magnitude space; (2) counterparts in the SDSS DR9 imaging data are determined with a simple positional match to the *WISE* coordinates. XMMSL covers about 50% of the eBOSS area and provides an additional $0.2 \deg^{-2}$ new point sources on average. The selection of the RASS and XMMSL point sources is limited at $r = 22$ (Galactic extinction corrected). Details of the targeting scheme for Tier 0 AGN will be described in Dwelly et al. (2017).

For Tier 0 extended sources, the Constrain Dark Energy with X-ray Clusters (CODEX) team has identified photon overdensities in RASS that correspond to galaxy clusters (Finoguenov et al. 2012). These clusters, plus Planck-detected clusters, have been matched to likely cluster members using SDSS DR9 imaging, specifically using the red-sequence Matched-filter Probabilistic Percolation method (redMaPPer; Rykoff et al. 2014). There are about 5000 such clusters within the eBOSS footprint. In addition, ~300 clusters are identified serendipitously by XMM and also matched to DR9 (XCLASS; Clerc et al. 2012; Sadibekova et al. 2014). SPIDERS targets cluster galaxies down to $i_{\mathrm{fiber}} = 21$ (Galactic extinction corrected). From these cluster samples, there is a target density of up to $20 \deg^{-2}$ on average; because these targets are concentrated in dense clusters and are subject to fiber collisions, only $7–8 \deg^{-2}$ are assigned fibers. When including previous SDSS legacy spectroscopic observations, SPIDERS reaches a median of approximately 10 galaxies per cluster with spectroscopic redshifts. Details of the clusters targeting algorithms and of the analysis steps are presented in Clerc et al. (2016).

For Tiers 1 and 2 point sources (AGN), eRASS:1 and eRASS:3 will be matched to SDSS DR9 imaging. We will target AGNs with $17 < r < 22$. In the eROSITA-DE sky area, this procedure will yield about 4000 targets in eRASS:1 and 7000 in eRASS:3 that are not already targeted by eBOSS. Including both eBOSS and SPIDERS, there will be ~15,000 eROSITA-detected AGNs with optical spectra from SDSS-IV.

For Tiers 1 and 2 extended sources (clusters), member galaxies will be identified using the same methods as for CODEX and XCLASS, but the improved spatial resolution and depth of eRASS relative to RASS will allow the targeting of intrinsically less massive and/or more distant clusters. The number of galaxies assigned fibers per cluster range from 1 to

10 depending on distance and cluster richness. Based on estimated cluster counts in eROSITA simulations, SPIDERS expects target densities of 7 deg^{-2} in eRASS:1 and 10 deg^{-2} in eRASS:3.

SPIDERS data are processed through the same pipeline that processes eBOSS data. Figure 9 shows an example spectrum from the first year of SPIDERS: an AGN selected as an X-ray emitter in RASS.

6.3. TDSS

6.3.1. TDSS Motivation

The variable sky is the focus of many recent and upcoming large-scale photometric surveys. For example, the SDSS Supernova program included 100 epochs of *ugriz* imaging on a 2°.5 wide region on the Celestial Equator in the SGC (Stripe 82; Sesar et al. 2007). Recently concluded and ongoing surveys include Pan-STARRS1 (PS1; Kaiser et al. 2010), the Catalina Real-Team Transient Survey (CRTS; Drake et al. 2009), and the Palomar Transient Factory (PTF; Law et al. 2009), to be followed by the Zwicky Transient Factory (ZTF; Bellm 2014; Smith et al. 2014). In the 2020s, the Large Synoptic Survey Telescope (LSST; LSST Science Collaborations & LSST Project 2009) will provide an unprecedented number of transients and variable stars and quasars. The study of variable sources will improve our understanding of fundamental processes regarding the evolution of astrophysical objects. Accreting supermassive black holes, manifesting themselves as active galactic nuclei, quasars, and blazars, often vary by tens of percent or more in the optical on month- to year-long timescales. Stellar variability reveals magnetic activity on stellar surfaces, interactions between members of binaries, and pulsations.

To physically characterize the variable objects in these surveys, a number of targeted programs have conducted spectroscopy on selected variable types such as quasars, RR Lyrae stars, subdwarfs, white dwarfs, and binaries (e.g., Geier et al. 2011; Palanque-Delabrouille et al. 2011; Rebassa-Mansergas et al. 2011; Badenes et al. 2013; Drake et al. 2013). The aim of TDSS is to conduct a large-scale, statistically complete survey of all variable types, without an imposed bias to either color or specific light-curve character. This survey provides critical information necessary to map photometric variability properties onto physical classifications for currently ongoing projects, and future endeavors such as LSST.

TDSS is creating a sample of single-epoch spectroscopy of 200,000 variable sources selected from PS1 over the 7500 deg^2 of eBOSS; about 140,000 of these are selected already for eBOSS or have had spectra in SDSS-I/II/III. For a subset of selected objects ($\sim$10,000), TDSS is conducting few-epoch spectroscopy (two to three visits over the duration of SDSS-IV) to use spectroscopic variability to characterize the objects.

6.3.2. TDSS Target Selection

Morganson et al. (2015) describes the target selection for TDSS single-epoch spectroscopy, and Ruan et al. (2016) and describes early spectroscopic results. In brief, *griz* imaging is used to select targets from SDSS DR9 and PS1. SDSS data were taken between 1998 and 2009, with typically only one epoch per observation. The PS1 3π survey acquired 10–15 epochs of imaging between 2010 and 2013. TDSS uses the SDSS-PS1 comparison as a measure of long-term variability,

and the variation among PS1 epochs as a measure of short-term variability. Adopting the Stripe 82 database as a testbed, Morganson et al. (2015) developed an estimator E related to the probability of a specific source being variable based on the short- and long-term variability, and the apparent magnitude. This estimate is applied to a set of isolated point sources with $17 < i < 22$ and defined a threshold E above which to select objects as likely variables. Across most of the sky (80%) TDSS randomly selects 10 targets per deg^2 that pass this threshold and are not already eBOSS quasar targets. In the remaining sky (20%), there are fewer than 10 unique targets that pass the threshold, and TDSS selects some targets at lower E.

About 10% of the fibers devoted to TDSS are dedicated to repeat spectroscopy of previously known objects already having at least one extant SDSS spectrum in the archive, and which are anticipated to reveal astrophysically interesting spectral variablity with an additional epoch or two of further spectroscopy. This few-epoch spectroscopy was initially conducted in eight planned programs. The subjects of these programs are: radial velocities of dwarf carbon stars; M-dwarf/white dwarf binaries; active ultracool dwarfs; highly variable ($>$0.2 mag) stars; broad absorption line quasars (Grier et al. 2016); Balmer-line variability in bright quasars (Runnoe et al. 2016); double-peaked broad emission-line quasars; and Mg II velocity variability in quasars.

TDSS data is processed through the same pipeline that processes eBOSS observations. Figure 9 displays an example spectrum from the first year of TDSS: a variable broad absorption line quasar selected for few-epoch spectroscopy.

6.4. Quasar Science with eBOSS, SPIDERS, and TDSS

eBOSS, TDSS, and SPIDERS together select more than half a million quasar targets. This enormous quasar catalog (tripling the world's number of quasar spectra) includes objects targeted by optical and mid-IR (*WISE*) colors, variability (TDSS), radio (FIRST), and X-ray emission (SPIDERS). Combined with previous SDSS and BOSS observations, the catalog spans a factor of more than $\sim$1000 in accretion luminosity from $z = 0$ to $z = 5$. Whereas previous surveys have sampled different quasar luminosity classes at different redshifts, the SDSS-IV sample enables an understanding of individual classes of quasars across epochs and better trace the full history of active BH growth since $z \approx 3$. Figure 10 shows the increased density of quasars in SDSS-IV relative to previous SDSS surveys, as well as its extension to fainter luminosities in the range $1 < z < 2$.

The best measurements of the Type I quasar luminosity function at $z < 2$ from optical survey data come from 10,000 quasars compiled by the 2dF-SDSS LRG and QSO (2SLAQ) survey (Croom et al. 2009); using deeper data, previous SDSS programs have extended to higher redshifts but have not probed these lower redshifts as densely (Palanque-Delabrouille et al. 2013). This survey targeted quasars to a similar depth as eBOSS (though the eBOSS limit of $r < 22$ reaches many more quasars than the 2SLAQ limit of $g < 21.85$), but over an area $\sim$40 times smaller. The statistical power provided by the large—and highly complete—eBOSS sample provides a powerful new probe of the evolution of the faint-end slope of the luminosity function over the interval from $z = 1$ to $z = 2$, strongly constraining feedback models for black hole growth (e.g., Hopkins et al. 2007).
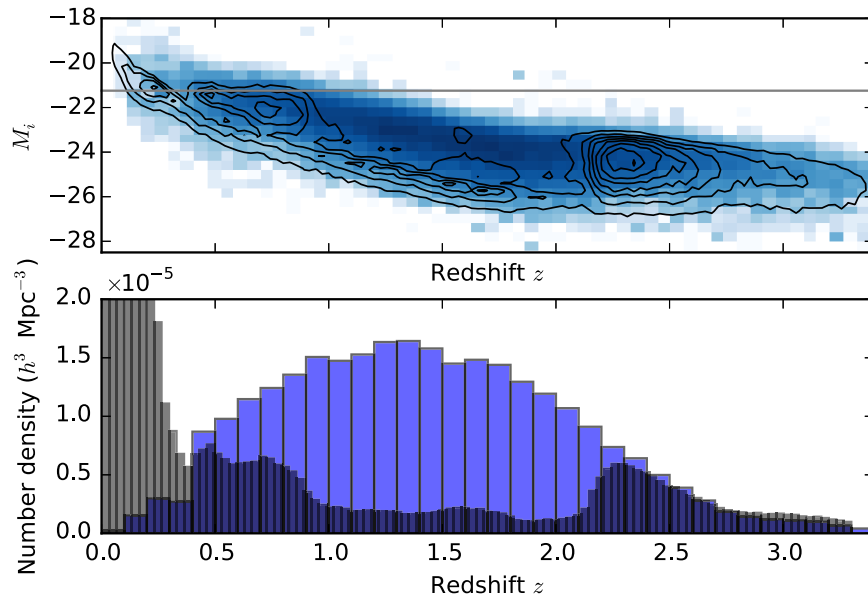
Figure 10. Distribution of quasars in redshift and rest-frame *i*-band absolute magnitude. Top panel: contours show the density of Legacy and BOSS quasars in this plane from SDSS-I through SDSS-III. The grayscale represents the density of eBOSS, TDSS, and SPIDERS quasars from SDSS-IV from the first year results. In the range $1 < z < 2$, the SDSS-IV quasars probe much lower luminosities than previous SDSS samples. The gray horizontal line corresponds to M_* for galaxies (Blanton et al. 2005); the SDSS-IV quasars out to $z \sim 2$ approach the faintness of Seyfert galaxies in optical luminosity. Bottom panel: each histogram shows the density of quasars as a function of redshift. The gray histogram is for Legacy and BOSS quasars from SDSS-I through SDSS-III. The blue histogram shows the estimated density of eBOSS quasars from the first year results. In the range $1 < z < 2$, the eBOSS sample represents an increase in density by factors of 5–10.

Combining measurements of the faint end of the luminosity function with precision probes of quasar clustering constrains models for quasar lifetimes, the typical halos hosting quasars, the co-evolution of quasars and spheroidal galaxies, and the evolution in black hole mass of active quasars (using virial mass estimators). Within the redshift range $1 < z < 2$, the mass of black holes powering quasars is expected to decrease with increasing redshift by an order of magnitude, perhaps symptomatic of the characteristic fueling mechanism shifting from major mergers to secular processes (Hopkins & Hernquist 2006). This prediction can be robustly tested with eBOSS's measurements of the luminosity dependence of quasar clustering. Finally, cross-correlation analyses of eBOSS galaxies and quasars at redshifts where samples overlap provides unique insight into the connection between quasars and galaxies (both quenched and star-forming).

Selecting quasars using several different techniques within eBOSS, TDSS, and SPIDERS allows SDSS-IV to account for the selection biases that affect any individual quasar selection technique. For example, the SDSS-iV data enables the comparison of high-redshift quasars with lower luminosity, X-ray selected AGNs at low redshift that may represent their descendants. A further advantage provided by SDSS-IV is the ability to tie together the faint quasar population at optical (eBOSS) and X-ray (SPIDERS) wavelengths within the same survey. Reaching the optically fainter quasar population provides access to a much larger number of significantly reddened quasars, yielding a more complete census of narrow-line and reddened broad-line AGNs.

Large quasar samples are useful not only for demographic studies, but also for yielding rare phenomena. Repeat spectroscopy of known quasars through TDSS captures changes in the absorption profiles of clouds along the line of sight to quasar nuclear regions (e.g., Filiz et al. 2013), rare state changes when the nuclear emission effectively vanishes (so-called "changing-look" quasars; LaMassa et al. 2015; Runnoe

et al. 2016), and a variety of other time-dependent phenomena traced by multi-epoch quasar spectroscopy. The unprecedented density of quasar targeting within SDSS-IV, particularly when considering that most known quasars will not be re-targeted and thus can have nearby objects targeted within the fiber collision radius, probes the environments of quasars through small-scale clustering with far greater numbers and more uniformity than achieved even by dedicated surveys of quasar pairs (e.g., Hennawi et al. 2006). Combining small-scale quasar pairs with the large-scale clustering sample from eBOSS constrains halo occupation models of quasars over a wide range of both luminosity and spatial scales and permit detailed examination of the relationship between quasar triggering and environment.

There are three quasar programs that SDSS-IV is executing to enhance quasar science: a complete sample of AGNs on Stripe 82, a continuation of the SDSS-RM program, and a program for repeat quasar spectroscopy.

First, "Stripe82X" provides a focused effort to build a complete sample of AGNs with SDSS-IV spectroscopy, with a set of six spectroscopic plates dedicated to AGN targets. The plates span a footprint of $\sim$35 deg^2 within the SDSS Stripe 82 region, bounding the area defined by the Stripe 82 X-ray survey of LaMassa et al. (2016) between $\alpha_{J2000} = 14°$ and $\alpha_{J2000} = 28°$. X-ray sources drawn from LaMassa et al. (2016) with optical counterparts having $r < 22.5$ provide the primary target class for the Stripe82X survey, totaling nearly 900 objects. The remaining fibers on each plate are primarily assigned to *WISE*-selected AGNs (using the R75 color criteria of Assef et al. 2013) and variability-selected quasars (Peters et al. 2015; Palanque-Delabrouille et al. 2016). A small number of high-redshift quasar candidates and repeat observations of "changing look" and related quasar candidates using TDSS selection criteria are also included. The tiling includes roughly 5000 AGN targets. The primary goals of the Stripe82X program are (1) to better characterize AGN bolometric

corrections by combining the spectroscopy with the extensive multiwavelength photometry available on Stripe 82; (2) to explore and compare the diverse classes of AGNs selected by different wavelength regimes; and (3) to construct a bolometric AGN luminosity function from a highly complete, faint AGN sample.

Second, during dark time, SDSS-IV is continuing the SDSS-RM program (Shen et al. 2015) initiated during the last observing semester of SDSS-III in 2014 (Alam et al. 2015a). SDSS-RM monitors a sample of 849 quasars within a single $7\,\mathrm{deg}^2$ field with BOSS spectroscopy and accompanying photometry to measure quasar broad-line time lags with the reverberation mapping technique (e.g., Blandford & McKee 1982; Peterson et al. 1993). In eBOSS, the SDSS-RM spectroscopy has a cadence of 2 epochs (similar depth to eBOSS) per month (12 epochs/year) since 2015, and provides an extended temporal baseline to detect broad-line lags on multi-year timescales in high-redshift quasars when combined with earlier SDSS-RM data.

Third, a Repeat Quasar Spectroscopy (RQS) program emphasizing known quasars is being observed in the eBOSS ELG region discussed in Section 6.1.3, supplementing the TDSS few-epoch spectroscopy. In this $\sim 10^3\,\mathrm{deg}^2$ region, TDSS is also obtaining a new epoch of spectroscopy for previously known SDSS quasars. In this region, we include quasars with $17 < i < 21$ (also including morphologically extended AGNs) from the DR7 or DR12 quasar catalogs, or SDSS-IV objects with spectro-pipeline class "QSO" that have been vetted as quasars/AGNs by our own visual inspection of the spectra. As part of the ELG plates, TDSS observes a total of $\sim 10^4$ known quasars/AGNs for an additional epoch of spectroscopy, including the bulk of all known SDSS quasars in this region to $i < 19.1$, as well as filling additional available fibers for RQS with either: known SDSS quasars extending to $i < 20.5$ already having more than one extant epoch of on-hand spectroscopy; and/or additional of the most highly variable known SDSS quasars in the ELG region, as determined from a reduced chi-squared measure of their photometric variability in SDSS and PS1 imaging. Details of RQS target selection will be reported in a future publication (C. MacLeod et al. 2017, in preparation).

SDSS-IV maintains the tradition established by the previous incarnations of the survey to publicly release quasar catalogs (e.g., Schneider et al. 2010; Pâris et al. 2014) associated with each release of new spectroscopic data. In SDSS-III, starting from the output of the the SDSS pipeline (Bolton et al. 2012), the spectrum of each quasar target was visually inspected to confirm both its identification and redshift. This procedure ensured the high purity of the catalog content and contributed to improvements in the SDSS pipeline. The quasar target density of SDSS-IV is approximately three times larger than in SDSS-III. This increase combined with the amount of time required to perform a systematic visual inspection of all quasar targets forces us to adapt our strategy to construct quasar catalogs. Hence, we developed a semi-automated scheme: starting from the output of the SDSS pipeline, we identify spectra for which the identification and/or redshift produced by the automated pipeline are questionable. The spectra of these objects ($\sim$7% of the targets) are then visually inspected. This automated strategy was tested against a fully visually inspected sample drawn from the SDSS-IV pilot survey performed at the end of SDSS-III and its design delivers a quasar catalog with a

purity larger than 99% and a loss of less than 1% of actual quasars (see Dawson et al. 2016 for more details).

The content of the SDSS-IV quasar catalog is similar to the previous ones. Multiwavelength information is provided when available along with spectroscopic properties such as emission-line fitting, presence of broad absorption lines and improved redshift estimates. At the conclusion of SDSS-IV, the photometric and spectroscopic properties of about a million quasars will be released.

7. Data Management

SDSS-IV data management encompasses the transfer of data among survey facilities, long-term archiving of data and metadata, documentation, and distribution to the collaboration and the public. We build on the data distribution systems developed for SDSS-I through SDSS-III.

The central data system for SDSS-IV is the Science Archive Server (SAS) hosted by the University of Utah Center for High Performance Computing. The SAS serves as a data repository with all survey targeting data, raw data, and reduced data on disk, and has associated computing to perform reductions and other critical operations. It has a current capacity of around 1 petabyte, in order to accommodate the variety of necessary imaging data sets and spectroscopic reduction versions produced during the survey. A Science Archive Mirror (SAM) at a separate location contains a copy of all the archived data; the SAM is housed by the National Energy Research Scientific Computing Center (NERSC) at the Lawrence Berkeley National Laboratory during the lifetime of the survey. In addition, the archived data are backed up on long-term tape storage at the High Performance Storage System (HPSS) at NERSC. The SAS system also contains the project wiki, used for documentation and internal communication, and a `subversion` server used for software version control. These systems are also backed up at the SAM.

Survey targeting data, plate design data, and other data associated with the observational planning are stored on the SAS and information is distributed from there to the University of Washington plate drilling facility and to APO and LCO as necessary for conducting operations. Data and metadata from the plate drilling quality assurance process are backed up to the SAS. At APO, the plate-plugging metadata, observing logs, telescope telemetry, and the raw data are transferred each day from the previous night's observing to the SAS (Weaver et al. 2015) and backed up on the SAM and HPSS. A similar system is installed at LCO.

The eBOSS, MaNGA, and APOGEE-2 pipelines are run automatically on each night's data as they arrive. For eBOSS, this process consists of the full pipeline through the production of 1D calibrated spectra, redshifts, and other parameters, for each completed plate. For MaNGA, this process consists of the Data Reduction Pipeline executed for each completed plate. However, currently the Data Analysis Pipeline is experiencing more development and is not run automatically; it is instead run periodically based on accumulated data and progress in DAP development. For APOGEE-2, the visit spectrum reductions and radial velocity determinations are performed automatically. However, because the combined spectra require multiple visits and because of its computational expense, the ASPCAP analysis is performed periodically on large sets of plates, again based on accumulated data and progress in ASPCAP development.

Table 5
SDSS-IV Data Releases

Name	Release Date	Data Through	eBOSS	MaNGA	APOGEE-2N	APOGEE-2S
DR13	2016 Jul	2015 Jul	SEQUELS[a]	New data and products[b]	New products	⋯
DR14	2017 Jul	2016 Jul	New data	New data	New data	⋯
DR15	2018 Jul	2017 Jul	⋯	New data and products[c]	⋯	⋯
DR16	2019 Jul	2018 Jul	New data	New data	New data	New data
DR17	2020 Dec	2019 Jul	New data	New data	New data	New data

Notes. The timing of the last two data releases will be based on available funding. "New data" means that new data are being released. "New products" means that new types of data analysis are being released.
[a] DR13 contains the remainder of the SEQUELS program, begun in SDSS-III and completed in SDSS-IV, and new reductions for BOSS data, but no new eBOSS data.
[b] DR13 and DR14 contain MaNGA Data Release Pipeline results; these are calibrated spectral data cubes.
[c] DR15 contains MaNGA Data Analysis Pipeline results; these include maps of derived quantities from the spectral data cubes.

The primary point of data access for collaboration members is the SAS. Collaboration members can access data on the SAS through ssh connections. SAS also provides http, rsync, and Globus access to the data files. These methods are available also to the astronomical community for publicly released data both for the SAS and SAM. We provide a web interface and an application program interface (API) on SAS to the eBOSS and APOGEE. A similar set of interfaces is being developed for MaNGA called Marvin, which will additionally have a Python module for interaction with the API. The data directory structure and file format documentation is provided as a "data model."[134]

Public data releases incorporate both the SAS data interface and the Catalog Archive Server (CAS), hosted at Johns Hopkins University. The CAS contains catalog data from the SDSS imaging and spectroscopic survey; it does not currently include images or spectra (other than JPEG and PNG versions, respectively, for visual browsing). The total database size is approximately 12 Tb, which is dominated by SDSS imaging catalogs. The CAS provides web browser-based access in synchronous mode via the SkyServer web application[135] and in asynchronous mode with the CASJobs batch query service.[136]

The SkyServer (Szalay et al. 2002) supports multiple levels of data access ranging from simple form-based queries aimed at novice users to raw SQL queries for expert users. The SkyServer includes interfaces displaying the SDSS and 2MASS imaging and the locations of SDSS spectroscopic and imaging catalog entries, as well as an Explore tool for each object showing the spectra and listing key parameters.

CASJobs (Li & Thakar 2008) gives each user their own server-side database called MyDB, along with the ability to submit arbitrarily complex SQL queries in batch mode and redirect the output to their MyDB. Users may import their own data to cross-match with the SDSS data. There is a Groups feature to allow users to share their data with collaborators. CASJobs also supports a command-line mode of query submission. For SDSS-IV, SkyServer and CASJobs are integrated into the SciServer collaborative data-driven science framework[137] with seamless single sign-on access to several new services such as Compute, SciDrive, SciScript, and SkyQuery. Compute includes a Jupyter notebook server that has fast server-side access to CASJobs and other data sets.

The SDSS data distribution system is heavily used. The CASJobs system has approximately 2000 unique users each year. The SkyServer system experiences tens sf millions of queries each year. The SAS system is used to download tens of terabytes of data per year by public users. The SDSS help desk email account fields around 500 inquiries per year.

We plan to release data on regular intervals. The released data include targeting data, raw and reduced spectroscopic data including of calibrations, derived quantities of several varieties, and value-added catalogs provided by collaboration members. All metadata and intermediate data are included and documented. Table 5 shows our nominal data release plans. The data releases include not just SDSS-IV data but also data from previous phases of SDSS, and the services host all previous data releases. New types of analysis or increments of new data may be added based on availability. Because of funding uncertainty, the timing of the last two data releases remains unclear; nevertheless, SDSS-IV is committed to a final public release of all of its data.

8. Education and Public Engagement

The mission statement of education and public engagement for SDSS-IV is to make the engineering and scientific results of all SDSS surveys accessible to the public through formal education, citizen science, news, and social media. SDSS-IV will continue and expand upon the activities in these areas of its predecessors. SDSS public outreach activities are based on real astronomical data accessed through the same databases as used by professionals. These activities expand the user base of SDSS data and thus its scientific reach, both through training and directly through investigations made possible with these scientific tools.

These activities include the public distribution of data, the development of inquiry-led education material suitable for middle school and above, the distribution of SDSS plates to educational venues to support engagement with SDSS data in the classroom, development of new citizen science projects through collaboration with the Zooniverse[138] (building on the success of Galaxy Zoo[139]), regular blogging,[140] and increased social media engagement, including multi-lingual activity.[141] These activities are coordinated by co-Chairs of a Committee

---

[134] http://data.sdss.org/datamodel
[135] http://skyserver.sdss.org/
[136] http://skyserver.sdss.org/casjobs/
[137] http://sciserver.org/

[138] http://www.zooniverse.org
[139] http://www.galaxyzoo.org
[140] http://blog.sdss.org
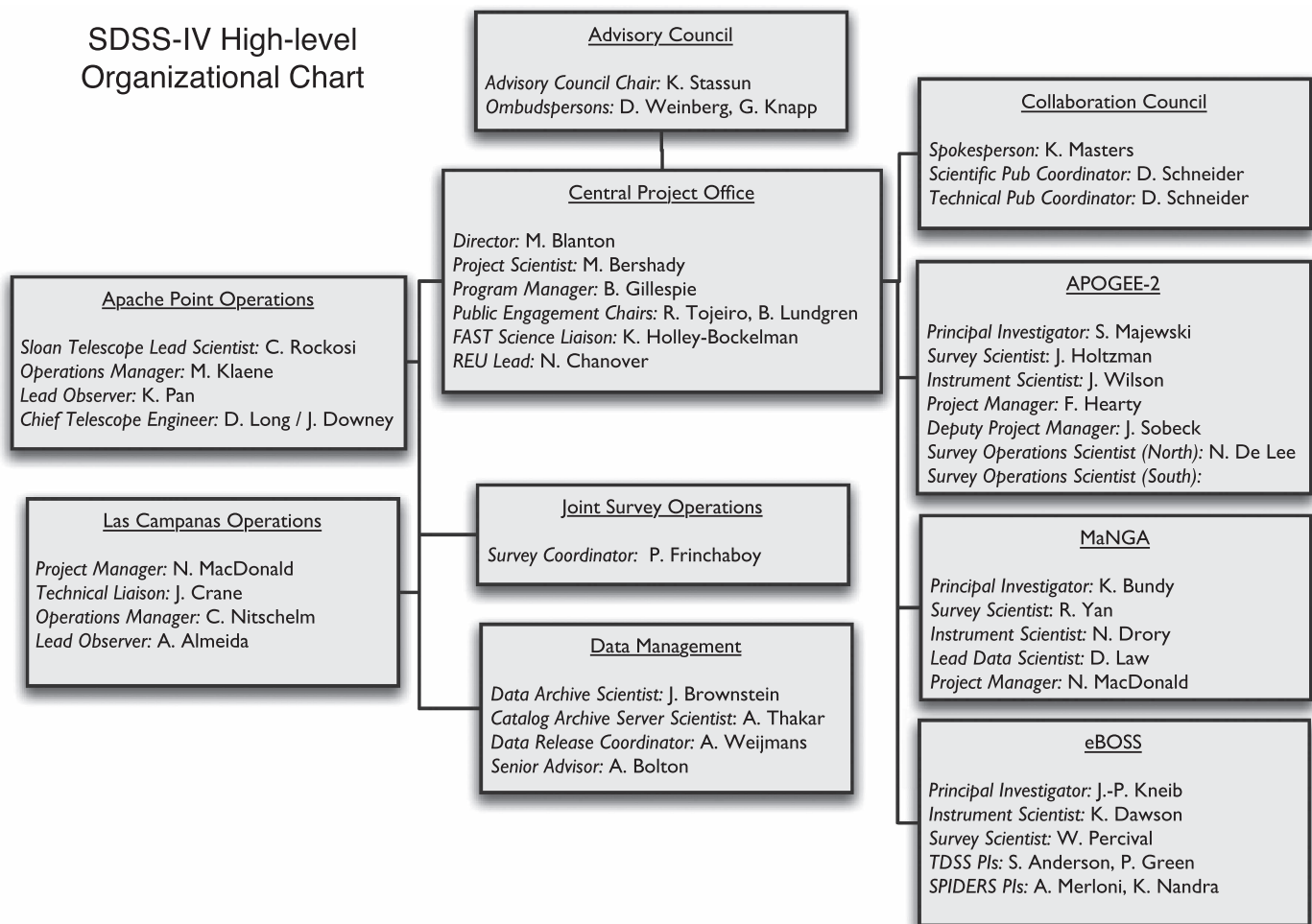[141] http://www.facebook.com/SDSSurveys; https://twitter.com/sdssurveys

Figure 11. High-level organizational chart for SDSS-IV, as of 2017 February. Positions have rotated somewhat during the project and will continue to do so.

on Education and Public Engagement, and are partly funded by the SDSS-IV project and partly the result of voluntary activities by collaboration members.

The SkyServer contains material, tutorials, and activities designed for outreach and education. Based on SkyServer tools, SDSS Voyages[142] is created for educators for designing curricula around astronomical data from the SDSS. The activities on the site range from very short to extended projects, aimed at middle and high school students. We have begun a program associated with the SDSS Voyages activities of distributing to teachers used plug plates, which so far has reached 32 schools.

9. Management and Collaboration

9.1. Project Management

The governance and management structure of SDSS-IV continues the highly successful structure developed over its previous phases. SDSS-IV is ultimately overseen by the Astrophysical Research Consortium (ARC) and its Board of Governors. The ARC Board has established a set of SDSS-IV Principles of Operations,[143] which provides the governance and management structure of the project.

Institutions join the collaboration via contributions, both technical and financial, committed to through Memoranda of Understanding (MOUs). Scientists at these institutions have data rights to all of the SDSS-IV surveys. "Full membership" yields data rights for all employees at an institution. "Associate membership," which requires a smaller contribution, yields data rights for a limited number of scientists. Technical contributions must directly address items in the survey budget.

The ARC Board has established an Advisory Council (AC) that oversees the Director and the project. The AC consists of representatives from the member institutions. It approves each new MOU and has authority over significant changes in policy, changes in the project scope, and fundraising activities.

Figure 11 shows the high-level organizational chart. The management structure is designed to unify decision-making and establish clear lines of authority for the allocation of resources by the Central Project Office.

The Central Project Office contains the Director, the Project Scientist, the Program Manager, and the Project Spokesperson. The Director makes spending, budget, and fundraising decisions, and resolves decision-making conflicts. The Project Scientist's role is to ensure the scientific quality and integrity of the project, through reviews of the scientific plans and products. The Program Manager is the full-time manager of the project, tracking the schedule and project personnel issues.

The co-Chairs of Education and Public Engagement and the FAST Science Liaison are part of the Central Project.

The Project Spokesperson is the leader of the Science Collaboration and represents SDSS-IV to the scientific community. The Science Collaboration is described more fully in the next subsection.

The leadership teams of each core program in SDSS-IV (APOGEE-2, eBOSS, MaNGA) have a common structure. Each program has a Principal Investigator (PI), a Survey Scientist, and an Instrument Scientist. The PI is responsible for leading each survey, both scientifically and in terms of its management. The Survey Scientist is responsible for the proper execution of the survey. The particular focus of the Survey Scientist differs from survey to survey, and ranges from overall scientific strategy to pipeline development. The Instrument Scientist is responsible for the development and maintenance of the instrument. For eBOSS, the instrument is stable and not under development; in this case, the Instrument Scientist takes on many of the operational tasks. For MaNGA and APOGEE-2, which have major hardware upgrades and development, the instrument scientists are much more focused on that development. For the same reason, MaNGA and APOGEE-2 have Project Managers to lead the hardware construction. SPIDERS and TDSS each have PIs but not the other leadership positions.

Several positions exist to support common goals and coordination. The Data Management team leads the data management and distribution. A Survey Coordinator plans and monitors the survey observational strategy. The co-Chairs of Education and Public Engagement lead a committee coordinating the development of educational materials and public engagement activities.

At APO, the Sloan Telescope Lead Scientist manages the infrastructure development and maintenance of the telescope and the APO Operations Manager manages the day-to-day operations, including site maintenance. At LCO, the LCO Project Manager leads the hardware development and the LCO Operations Manager manages the day-to-day survey operations. The LCO site maintenance and telescope maintenance is handled by the Observatories of the Carnegie Institution for Science.

Logistical responsibility for handling scientific, technical, and data release papers rests with the Scientific Publications Coordinator (SPC), Technical Publications Coordinator (TPC), and Scientific Spokesperson, respectively. Publications Coordinators ensure that publications follow standard survey publication processes, and they maintain a common electronic web-based archive of all scientific, technical, and data release publications of the SDSS-IV, accessible to collaboration members. The TPC coordinates the publication of technical papers, ensuring that the technical documentation of the project is disseminated efficiently and promptly. The SPC is responsible for tracking SDSS-IV scientific papers through the publication policy process and assuring that all SDSS-IV papers (scientific, technical, and data release) reference the appropriate technical papers. The Scientific Spokesperson has overall responsibility for the Publications Archive, and coordinates the publication of the data release papers.

The individuals filling these roles and the teams they lead are geographically distributed at over 20 institutions. Each team communicates through email lists, weekly phone meetings, and periodic in-person meetings. A Management Committee consisting of individuals in the positions listed here meets weekly to monitor the project progress.

9.2. Science Collaboration

The Science Collaboration is led by the Project Spokesperson, who is elected for a three-year term by the collaboration. A Collaboration Council consisting of representatives from the participating institutions advises the Spokesperson. The Spokesperson and the Collaboration Council developed the Publication Policy for SDSS-IV.

Following previous SDSS collaborations, the Publication Policy's guiding principle is that all participants can pursue any project so long as they notify the entire collaboration of their plans and update the collaboration as projects progress. Groups pursuing similar science projects are encouraged to collaborate, but they are not required to do so. There is no binding internal refereeing process. Instead, draft publications using non-public data must be posted to the whole collaboration for a review period of at least three weeks prior to submission to any journal or online archive. Participants outside of the core analysis team may request co-authorship on a paper if they played a significant role in producing the data or analysis tools that enabled it. Scientists who have contributed at least one year of effort to SDSS-IV infrastructure development or operations can request "Architect" status, which entitles them to request co-authorship on any science publications for those surveys to which they contributed. All SDSS-IV authorship requests are expected to comply with the professional guidelines of the American Physical Society.

Each of the SDSS-IV programs has Science Working Groups to coordinate and promote scientific collaboration within the team. These working groups overlap and interact with the SDSS-IV project personnel but are more focused on science analysis. The working groups communicate and collaborate through archived e-mail lists, wiki pages, regular teleconferences, and in-person meetings. Importantly, the science activities of these working groups are not funded by the SDSS-IV project.

The policies of SDSS-IV allow limited proprietary data rights to astronomers outside the collaboration under specific conditions that fall into two categories. First, when an SDSS-IV member leaves for a non-SDSS institution. The member can ask the Collaboration Council and Management Committee for "Continuing External Collaborator" status to complete a defined scientific investigation that had been substantially started before the change in institutions. Second, if crucial skills to complete science of interest to SDSS-IV members are not available within the SDSS-IV collaboration, due to either personnel or time constraints, SDSS-IV members can ask the collaboration, with approval from the Collaboration Council and Management Committee, for "External Collaborator" status for non-SDSS members to work on specific aspects of declared projects. The collaboration evaluates whether the contributions of the non-members are unique and necessary to produce cutting-edge science from the SDSS collaboration for a limited number of papers.

The projects, publications, and other activities are tracked in a central database as part of the SDSS-IV data system. Collaboration members use a web application to interact with this internal database. This system lends clarity to the status of approvals and decisions with regard to internal collaboration activities.

9.3. Broadening Collaboration Participation

The past success of the SDSS collaboration has hinged on tapping into a diverse talent base. We have worked and continue to work within SDSS-IV on this issue. Other collaborations may find the SDSS-IV experience described here informative as they configure their policies or face similar situations.

The SDSS-IV organization does not directly hire any of the staff, so all recruitment of staff paid on contracts to institutions from ARC also must go through each institution's human resources process. Similarly, in cases of personnel issues, each institution has its own policies on workplace environment. The interleaving of SDSS-IV processes with institutional policies represents an interesting complication to international, multi-institutional organizations such as the SDSS.

As discussed in Lundgren et al. (2015), SDSS-IV identified early a disparity in the gender balance of its leadership structure. In order to identify the causes of, monitor, and address this issue, we created a Committee on the Participation of Women in the SDSS (CPWS). The CPWS initiated regular demographic surveys of the SDSS in order to monitor the make up of the collaboration and the project over time. The CPWS also compiled information on how the project leadership recruitment proceeded. Near the beginning of SDSS-IV, and in previous phases of the project, the recruitment for survey positions such as those in Figure 11 or others such as working group chairs, was conducted informally and in a relatively federated manner across the project.

In 2013, SDSS-IV began to implement an early recommendation of the CPWS to formalize the recruitment process. SDSS-IV policy is that open project leadership roles are defined and necessary qualifications discussed prior to searching for candidates. Roles now usually are defined with fixed duration to allow rotation and to mitigate the level of commitment required. We publicly advertise for candidates within the collaboration. Once candidates are identified, the slate of candidates is reviewed by the Central Project; at this point, if there is a paucity of female candidates, the reasons for this are explored and an attempt is made to redress the issue by encouraging qualified female candidates to apply. The process is tracked by the Central Project, which needs to approve all appointments. Lundgren et al. (2015) represents an initial attempt to assess the effectiveness of this process in increasing participation of women in the survey leadership; the results are as yet unclear for SDSS-IV.

In the same year, SDSS-IV formed a Committee on the Participation of Minorities in SDSS (CPMS) to address the underrepresentation of minorities in the survey. While the goal of the CPWS was to ensure gender balance in SDSS leadership, the CPMS was faced with the more fundamental goal of recruiting and retaining underrepresented minority talent in the collaboration at all. CPWS identified a lack of resources, training, and contact with the SDSS collaboration that is a barrier to full participation of minorities in the survey. In response, SDSS-IV implemented two immediate and strategic programs to have the most meaningful impact: the Faculty And Student Team (FAST) program deliberately focuses on building serious, long-term research relationships between faculty/student teams and SDSS partners; the distributed SDSS REU program targets talented minority students at the under-graduate level, and can be used as a recruitment tool into graduate school in astronomy.

The FAST program has been independently funded by the Sloan Foundation for an initial three-year period. It actively recruits and trains underrepresented minority (URM) talent to participate in SDSS science. To qualify for FAST, at least one team member is expected to be a URM and/or to have a track record serving URM scholars. FAST scholar teams are matched with established SDSS partners to work on a research project of mutual interest and receive specialized training, mentoring, and financial support in order to introduce teams to SDSS science and to cement their participation within the collaboration. FAST team faculty become full members of the SDSS collaboration, with all data rights, access to centralized computing, and ability to lead projects that this implies. We selected our first FAST cohort of three teams in 2015 and recruited five FAST teams in 2016. The distributed SDSS REU program has also been funded by the Sloan Foundation for one pilot summer in 2016, with six students at four institutions.

With regard to the climate of the SDSS-IV collaboration, the global nature of the survey poses unique challenges in developing an effective and positive work environment. Project personnel and science collaboration are distributed at dozens of institutions, in a number of countries. Opportunities for in-person interaction are often limited, with most communication happening through email and phone conversations. There is no central institution recruiting the leadership and personnel; in addition, a number of project personnel work on a voluntary basis or for "in-kind" credit for their technical work. Recognizing the potential issues that could arise in this environment, we requested that an advisory committee from the American Physical Society conduct a site visit at the 2014 collaboration meeting. There were numerous comments and suggestions from the visiting committee. In 2015, CPWS crafted these suggestions into a set of specific recommendations for the project to prioritize in order to maintain and improve the quality of the climate in the collaboration.

The CPWS and CPMS have now been combined into a single Committee on Inclusion in the SDSS (COINS) with the mandate of both original committees.

In order to address specific issues that may arise within the collaboration or other problems, the ARC Board has appointed two Ombudspersons for SDSS-IV that can be consulted to mediate problems within the collaboration. The position of Ombudsperson is particularly designed for cases where handling the matter through formal project channels would lead to a conflict of interest or cases where anonymity is desired. In addition, SDSS-IV is in the process of developing a formal Code of Conduct.

10. Summary

We have described SDSS-IV, which began operations in 2014 July, with plans to continue until mid-2020. The collaboration has over 1000 participating astronomers from over 50 institutions worldwide. Three major programs (APOGEE-2, MaNGA, and eBOSS) and two subprograms (TDSS and SPIDERS) will address a number of key scientific topics using dual-hemisphere wide-field spectroscopic facilities. The major elements of this science program are as follows.

1. Milky Way formation history and evolution, using chemical and dynamical mapping of all of its stellar components with APOGEE-2.
2. Stellar astrophysics, using APOGEE-2 infrared spectra alone and in combination with asteroseismology, using TDSS's optical observations of variable stars, and using MaNGA's bright-time optical stellar library.
3. Formation history and evolution of the diverse array of galaxy types, using chemical and dynamical mapping of stars and gas with MaNGA integral field spectroscopy, using the distant galaxy populations in the eBOSS LRG and ELG programs, and the cluster galaxies in SPIDERS.
4. Quasar properties and evolution using the massive sample of quasars in eBOSS, reaching nearly down to Seyfert galaxy luminosities out to $z \sim 2$, complemented with quasars selected via variability (TDSS) and X-ray emission (SPIDERS).
5. The most powerful cosmological constraints to date from large-scale structure, precisely investigating the Hubble diagram and the growth of structure in the redshift range $1 < z < 2$ for the first time, using the largest volume cosmological large-scale structure survey to date from eBOSS.

The science program is coupled to a robust education and public engagement program. All of the raw and reduced data will be released on a well-defined schedule using innovative public interfaces.

References

Abazajian, K. N., Adelman-McCarthy, J. K., Agüeros, M. A., et al. 2009, ApJS, 182, 543
Abbott, T., Abdalla, F. B., Aleksić, J., et al. 2016, MNRAS, 460, 1270
Planck Collaboration, Ade, P. A. R., Aghanim, N., et al. 2016, A&A, 594, A17
Ahn, C. P., Alexandroff, R., Allende Prieto, C., et al. 2012, ApJS, 203, 21
Aihara, H., Allende Prieto, C., An, D., et al. 2011, ApJS, 193, 29
Alam, S., Albareti, F. D., Allende Prieto, C., et al. 2015a, ApJS, 219, 12
Alam, S., Ho, S., Vargas-Magaña, M., & Schneider, D. P. 2015b, MNRAS, 453, 1754
Albrecht, A., Bernstein, G., Cahn, R., et al. 2006, arXiv:astro-ph/0609501
Allen, S. W., Evrard, A. E., & Mantz, A. B. 2011, ARA&A, 49, 409
Allende Prieto, C., Beers, T. C., Wilhelm, R., et al. 2006, ApJ, 636, 804
Allende Prieto, C., Sivarani, T., Beers, T. C., et al. 2008, AJ, 136, 2070
Alvarez, R., & Plez, B. 1998, A&A, 330, 1109
Anders, F., Chiappini, C., Santiago, B. X., et al. 2014, A&A, 564, A115
Anderson, S. F., Voges, W., Margon, B., et al. 2003, AJ, 126, 2209
Assef, R. J., Stern, D., Kochanek, C. S., et al. 2013, ApJ, 772, 26
Badenes, C., van Kerkwijk, M. H., Kilic, M., et al. 2013, MNRAS, 429, 3596
Aubourg, É., Bailey, S., Bautista, J. E., et al. 2015, PhRvD, 92, 123516
Battye, R. A., & Pearson, J. A. 2012, JCAP, 07, 019
Becker, G. D., Hewett, P. C., Worseck, G., & Prochaska, J. X. 2013, MNRAS, 430, 2067
Becker, R. H., White, R. L., & Helfand, D. J. 1995, ApJ, 450, 559
Bellm, E. 2014, in The Third Hot-wiring the Transient Universe Workshop (HTU-III), ed. P. R. Wozniak et al., 27
Benjamin, R. A., Churchwell, E., Babler, B. L., et al. 2003, PASP, 115, 953
Bershady, M. A., Verheijen, M. A. W., Swaters, R. A., et al. 2010, ApJ, 716, 198
Beutler, F., Saito, S., Seo, H.-J., et al. 2014, MNRAS, 443, 1065
Blandford, R. D., & McKee, C. F. 1982, ApJ, 255, 419
Blanton, M. R., Kazin, E., Muna, D., Weaver, B. A., & Price-Whelan, A. 2011, AJ, 142, 31
Blanton, M. R., Lin, H., Lupton, R. H., et al. 2003, AJ, 125, 2276
Blanton, M. R., Lupton, R. H., Schlegel, D. J., et al. 2005, ApJ, 631, 208
Boller, T., Freyberg, M. J., Trümper, J., et al. 2016, A&A, 588, A103
Bolton, A. S., Schlegel, D. J., Aubourg, É., et al. 2012, AJ, 144, 144
Bovy, J. 2016, ApJ, 817, 49
Bovy, J., Allende Prieto, C., Beers, T. C., et al. 2012a, ApJ, 759, 131
Bovy, J., Bird, J. C., García Pérez, A. E., et al. 2015, ApJ, 800, 83
Bovy, J., Hennawi, J. F., Hogg, D. W., et al. 2011, ApJ, 729, 141
Bovy, J., Myers, A. D., Hennawi, J. F., et al. 2012b, ApJ, 749, 41
Bovy, J., Rix, H.-W., Green, G. M., Schlafly, E. F., & Finkbeiner, D. P. 2016a, ApJ, 818, 130
Bovy, J., Rix, H.-W., Schlafly, E. F., et al. 2016b, ApJ, 823, 30
Bowen, I. S., & Vaughan, A. H., Jr 1973, ApOpt, 12, 1430
Bressan, A., Marigo, P., Girardi, L., et al. 2012, MNRAS, 427, 127
Budavari, T., Heinis, S., Szalay, A. S., et al. 2009, ApJ, 694, 1281
Bundy, K., Bershady, M. A., Law, D. R., et al. 2015, ApJ, 798, 7
Bundy, K., Leauthaud, A., Saito, S., et al. 2015, ApJS, 221, 15
Cappellari, M. 2008, MNRAS, 390, 71
Cappellari, M., Emsellem, E., Krajnović, D., et al. 2011, MNRAS, 416, 1680
Cappelluti, N., Brusa, M., Hasinger, G., et al. 2009, A&A, 497, 635
Chiappini, C., Anders, F., Rodrigues, T. S., et al. 2015, A&A, 576, L12
Churchwell, E., Babler, B. L., Meade, M. R., et al. 2009, PASP, 121, 213
Cirasuolo, M., Afonso, J., Carollo, M., et al. 2014, Proc. SPIE, 9147, 91470N
Civano, F., Marchesi, S., Comastri, A., et al. 2016, ApJ, 819, 62
Clerc, N., Merloni, A., Zhang, Y.-Y., et al. 2016, MNRAS, 463, 4490
Clerc, N., Sadibekova, T., Pierre, M., et al. 2012, yCat, 742, 33561
Collaboration, P., Ade, P. A. R., Aghanim, N., et al. 2014, A&A, 571, A16
Comparat, J., Delubac, T., Jouvel, S., et al. 2016, A&A, 592, A121
Comparat, J., Richard, J., Kneib, J.-P., et al. 2015, A&A, 575, A40
Cottaar, M., Covey, K. R., Foster, J. B., et al. 2015, ApJ, 807, 27
Cottaar, M., Covey, K. R., Meyer, M. R., et al. 2014, ApJ, 794, 125
Croom, S. M., Lawrence, J. S., Bland-Hawthorn, J., et al. 2012, MNRAS, 421, 872
Croom, S. M., Richards, G. T., Shanks, T., et al. 2009, MNRAS, 399, 1755
Cui, X.-Q., Zhao, Y.-H., Chu, Y.-Q., et al. 2012, RAA, 12, 1197
Dalal, N., Doré, O., Huterer, D., & Shirokov, A. 2008, PhRvD, 77, 123514
Dalton, G., Trager, S., Abrams, D. C., et al. 2014, Proc. SPIE, 9147, 91470L
Dawson, K. S., Kneib, J.-P., Percival, W. J., et al. 2016, AJ, 151, 44
Dawson, K. S., Schlegel, D. J., Ahn, C. P., et al. 2013, AJ, 145, 10
de Jong, R. S., Barden, S., Bellido-Tirado, O., et al. 2014, Proc. SPIE, 9147, 91470M

De Silva, G. M., Freeman, K. C., Asplund, M., et al. 2007, AJ, 133, 1161
De Silva, G. M., Freeman, K. C., Bland-Hawthorn, J., et al. 2015, MNRAS, 449, 2604
De Silva, G. M., Sneden, C., Paulson, D. B., et al. 2006, AJ, 131, 455
de Zeeuw, P. T., Bureau, M., Emsellem, E., et al. 2002, MNRAS, 329, 513
Drake, A. J., Catelan, M., Djorgovski, S. G., et al. 2013, ApJ, 763, 32
Drake, A. J., Djorgovski, S. G., Mahabal, A., et al. 2009, ApJ, 696, 870
Drory, N., MacDonald, N., Bershady, M. A., et al. 2015, AJ, 149, 77
Dvali, G., Gabadadze, G., & Porrati, M. 2000, PhLB, 485, 208
Dwelly, T., Salvato, M., Merloni, A., et al. 2017, MNRAS, 469, 1065
Eisenstein, D. J., Weinberg, D. H., Agol, E., et al. 2011, AJ, 142, 72
Eisenstein, D. J., et al. 2001, AJ, 122, 2267
Epstein, C. R., Elsworth, Y. P., Johnson, J. A., et al. 2014, ApJL, 785, L28
Feuillet, D. K., Bovy, J., Holtzman, J., et al. 2016, ApJ, 817, 40
Filiz, A. N., Brandt, W. N., Hall, P. B., et al. 2013, ApJ, 777, 168
Finkbeiner, D. P., Schlafly, E. F., Schlegel, D. J., et al. 2016, ApJ, 822, 66
Finoguenov, A., Watson, M. G., Tanaka, M., et al. 2012, yCat, 740, 32063
Fitzpatrick, E. L. 1999, PASP, 111, 63
Flaugher, B. L., Abbott, T. M. C., Angstadt, R., et al. 2012, Proc. SPIE, 8446, 11
Fleming, S. W., Mahadevan, S., Deshpande, R., et al. 2015, AJ, 149, 143
Fogli, G. L., Lisi, E., Marrone, A., et al. 2012, PhRvD, 86, 013012
Foster, J. B., Cottaar, M., Covey, K. R., et al. 2015, ApJ, 799, 136
Freeman, K., Ness, M., Wylie-de Boer, E., et al. 2013, MNRAS, 428, 3660
Frieman, J. A., Bassett, B., Becker, A., et al. 2008, AJ, 135, 338
Frinchaboy, P. M., Thompson, B., Jackson, K. M., et al. 2013, ApJL, 777, L1
Fukugita, M., Ichikawa, T., Gunn, J. E., et al. 1996, AJ, 111, 1748
García Pérez, A. E., Allende Prieto, C., Holtzman, J. A., et al. 2016, AJ, 151, 144
García Pérez, A. E., Cunha, K., Shetrone, M., et al. 2013, ApJL, 767, L9
García-Hernández, D. A., Mészáros, S., Monelli, M., et al. 2015, ApJL, 815, L4
Ge, J., Lee, B., de Lee, N., et al. 2009, Proc. SPIE, 7440, 74400L
Geier, S., Hirsch, H., Tillich, A., et al. 2011, A&A, 530, A28
Geisler, D. 1984, PASP, 96, 723
Gilmore, G., Randich, S., Asplund, M., et al. 2012, Msngr, 147, 25
Grier, C. J., Brandt, W. N., Hall, P. B., et al. 2016, ApJ, 824, 130
Gunn, J. E., Carr, M., Rockosi, C., et al. 1998, AJ, 116, 3040
Gunn, J. E., et al. 2006, AJ, 131, 2332
Guo, H., Zehavi, I., & Zheng, Z. 2012, ApJ, 756, 127
Guo, H., Zehavi, I., Zheng, Z., et al. 2013, ApJ, 767, 122
Gustafsson, B., Edvardsson, B., Eriksson, K., et al. 2008, A&A, 486, 951
Hayden, M. R., Bovy, J., Holtzman, J. A., et al. 2015, ApJ, 808, 132
Hempel, M., Minniti, D., Dékány, I., et al. 2014, Msngr, 155, 24
Hennawi, J. F., Strauss, M. A., Oguri, M., et al. 2006, AJ, 131, 1
Hill, G. J., Gebhardt, K., Komatsu, E., et al. 2008, in ASP Conf. Ser. 399, Panoramic Views of Galaxy Formation and Evolution, ed. T. Kodama, T. Yamada, & K. Aoki (San Francisco, CA: ASP), 115
Holtzman, J. A., Harrison, T. E., & Coughlin, J. L. 2010, AdAst, 2010, 1
Holtzman, J. A., Shetrone, M., Johnson, J. A., et al. 2015, AJ, 150, 148
Hopkins, P. F., & Hernquist, L. 2006, ApJS, 166, 1
Hopkins, P. F., Richards, G. T., & Hernquist, L. 2007, ApJ, 654, 731
Horne, K. 1986, in ASP 98 (San Francisco, CA: ASP), 609
Howard, C. D., Rich, R. M., Reitzel, D. B., et al. 2008, ApJ, 688, 1060
Hutchinson, T. A., Bolton, A. S., Dawson, K. S., et al. 2016, AJ, 152, 205
Huterer, D., Kirkby, D., Bean, R., et al. 2015, APh, 63, 23
Jouvel, S., Delubac, T., Comparat, J., et al. 2015, arXiv:1509.07121
Kaiser, N., Burgett, W., Chambers, K., et al. 2010, Proc. SPIE, 7733, 77330E
Kenter, A., Murray, S. S., Forman, W. R., et al. 2005, ApJS, 161, 9
Koesterke, L. 2009, in AIP Conf. Proc., Vol. 1171, Recent Directions in Astrophysical Quantitative Spectroscopy and Radiation Hydrodynamics: Proc. Int. Conf. in Honor of Dimitri Mihalas for His Lifetime Scientific Contributions on the Occasion of His 70th Birthday (Melville, NY: AIP), 73
Kordopatis, G., Gilmore, G., Steinmetz, M., et al. 2013, AJ, 146, 134
Kurucz, R. L. 1979, ApJS, 40, 1
Laird, E. S., Nandra, K., Georgakakis, A., et al. 2009, ApJS, 180, 102
LaMassa, S. M., Cales, S., Moran, E. C., et al. 2015, ApJ, 800, 144
LaMassa, S. M., Urry, C. M., Cappelluti, N., et al. 2016, ApJ, 817, 172
Lang, D., Hogg, D. W., & Schlegel, D. J. 2016, AJ, 151, 36
Law, D. R., Cherinka, B., Yan, R., et al. 2016, AJ, 152, 83
Law, D. R., Yan, R., Bershady, M. A., et al. 2015, AJ, 150, 19
Law, N. M., Kulkarni, S. R., Dekany, R. G., et al. 2009, PASP, 121, 1395
Le Borgne, J.-F., Bruzual, G., Pelló, R., et al. 2003, A&A, 402, 433
Leauthaud, A., Tinker, J., Bundy, K., et al. 2012, ApJ, 744, 159
Lee, K.-G., Hennawi, J. F., Spergel, D. N., et al. 2015, ApJ, 799, 196
Lee, Y. S., Beers, T. C., Carlin, J. L., et al. 2015, AJ, 150, 187

Levi, M., Bebek, C., Beers, T., et al. 2013, arXiv:1308.0847
Li, H., Li, R., Mao, S., et al. 2016, MNRAS, 455, 3680
Li, N., & Thakar, A. R. 2008, CSE, 10, 18
LSST Science Collaborations and LSST Project, 2009, arXiv:0912.0201
Lundgren, B., Kinemuchi, K., Zasowski, G., et al. 2015, PASP, 127, 776
Luo, B., Bauer, F. E., Brandt, W. N., et al. 2008, ApJS, 179, 19
Majewski, S. R., Hasselquist, S., Łokas, E. L., et al. 2013, ApJL, 777, L13
Majewski, S. R., Ostheimer, J. C., Kunkel, W. E., & Patterson, R. J. 2000, AJ, 120, 2550
Majewski, S. R., Schiavon, R. P., Frinchaboy, P. M., et al. 2015, arXiv:1509.05420
Majewski, S. R., Zasowski, G., & Nidever, D. L. 2011, ApJ, 739, 25
Maraston, C., Pforr, J., Henriques, B. M., et al. 2013, MNRAS, 435, 2764
Margala, D., Kirkby, D., Dawson, K., et al. 2016, ApJ, 831, 157
Martig, M., Rix, H.-W., Aguirre, V. S., et al. 2015, MNRAS, 451, 2230
McDonald, P., & Roy, A. 2009, JCAP, 08, 020
Merloni, A., Predehl, P., Becker, W., et al. 2012, arXiv:1209.3114
Mészáros, S., Allende Prieto, C., Edvardsson, B., et al. 2012, AJ, 144, 120
Mészáros, S., Holtzman, J., García Pérez, A. E., et al. 2013, AJ, 146, 133
Mészáros, S., Martell, S. L., Shetrone, M., et al. 2015, AJ, 149, 153
Minniti, D., Lucas, P. W., Emerson, J. P., et al. 2010, NewA, 15, 433
Montero-Dorta, A. D., Shu, Y., Bolton, A. S., Brownstein, J. R., & Weiner, B. J. 2016, MNRAS, 456, 3265
Morganson, E., Green, P. J., Anderson, S. F., et al. 2015, ApJ, 806, 244
Muñoz, R. R., Frinchaboy, P. M., Majewski, S. R., et al. 2005, ApJL, 631, L137
Murray, S. S., Kenter, A., Forman, W. R., et al. 2005, ApJS, 161, 1
Myers, A. D., Palanque-Delabrouille, N., Prakash, A., et al. 2015, ApJS, 221, 27
Nandra, K., Laird, E. S., Aird, J. A., et al. 2015, ApJS, 220, 10
Ness, M., Hogg, D. W., Rix, H. W., Ho, A. Y. Q., & Zasowski, G. 2015, ApJ, 808, 16
Ness, M., Zasowski, G., Johnson, J. A., et al. 2016, ApJ, 819, 2
Newman, J. A., Abate, A., Abdalla, F. B., et al. 2015, APh, 63, 81
Nidever, D. L., Bovy, J., Bird, J. C., et al. 2014, ApJ, 796, 38
Nidever, D. L., Holtzman, J. A., Allende Prieto, C., et al. 2015, AJ, 150, 173
Nidever, D. L., Zasowski, G., & Majewski, S. R. 2012, ApJS, 201, 35
Oke, J. B., & Gunn, J. E. 1983, ApJ, 266, 713
Osterbrock, D. E., & Ferland, G. J. 2006, Astrophysics of Gaseous Nebulae and Active Galactic Nuclei (Mill Valley, C: Univ. Science Books)
Palanque-Delabrouille, N., Magneville, C., Yèche, C., et al. 2013, A&A, 551, A29
Palanque-Delabrouille, N., Magneville, C., Yèche, C., et al. 2016, A&A, 587, A41
Palanque-Delabrouille, N., Yeche, C., Myers, A. D., et al. 2011, A&A, 530, A122
Pâris, I., Petitjean, P., Aubourg, É, et al. 2014, A&A, 563, A54
Perlmutter, S., Aldering, G., Goldhaber, G., et al. 1999, ApJ, 517, 565
Peters, C. M., Richards, G. T., Myers, A. D., et al. 2015, ApJ, 811, 95
Peterson, B. M., Ali, B., Horne, K., et al. 1993, ApJ, 402, 469
Pier, J. R., Munn, J. A., Hindsley, R. B., et al. 2003, AJ, 125, 1559
Pieri, M. M., Mortonson, M. J., Frank, S., et al. 2014, MNRAS, 441, 1718
Pinsonneault, M. H., Elsworth, Y., Epstein, C., et al. 2014, ApJS, 215, 19
Plez, B. 2012, Turbospectrum: Code for Spectral Synthesis, Astrophysics Source Code Library, ascl:1205.004
Prakash, A., Licquia, T. C., Newman, J. A., & Rao, S. M. 2015, ApJ, 803, 105
Predehl, P., Böhringer, H., Brunner, H., et al. 2010, in AIP Conf. Proc., Vol. 1248, X-ray Astronomy 2009; Present Status, Multi-Wavelength Approach and Future Perspectives (Melville, NY: AIP), 543
Prusti, T., de Bruijne, J. H. J., Brown, A. G. A., et al. 2016, A&A, 595, A1
Raichoor, A., Comparat, J., Delubac, T., et al. 2016, A&A, 585, A50
Randall, L., & Sundrum, R. 1999, PhRvL, 83, 3370
Rebassa-Mansergas, A., Nebot Gómez-Morán, A., Schreiber, M. R., Girven, J., & Gänsicke, B. T. 2011, MNRAS, 413, 1121
Reid, B. A., Seo, H.-J., Leauthaud, A., Tinker, J. L., & White, M. 2014, MNRAS, 444, 476
Richards, G. T., Fan, X., Newberg, H. J., et al. 2002, AJ, 123, 2945
Riess, A. G., Filippenko, A. V., Challis, P., et al. 1998, AJ, 116, 1009
Ruan, J. J., Anderson, S. F., Green, P. J., et al. 2016, ApJ, 825, 137
Runnoe, J. C., Cales, S., Ruan, J. J., et al. 2016, MNRAS, 455, 1691
Rykoff, E. S., Rozo, E., Busha, M. T., et al. 2014, ApJ, 785, 104
Sadibekova, T., Pierre, M., Clerc, N., et al. 2014, A&A, 571, A87
Sahni, V., & Shtanov, Y. 2003, JCAP, 11, 014
Saito, R. K., Hempel, M., Minniti, D., et al. 2012, A&A, 537, A107
Sako, M., Bassett, B., Becker, A. C., et al. 2014, arXiv:1401.3317
Samushia, L., Reid, B. A., White, M., et al. 2014, MNRAS, 439, 3504

Sánchez, S. F., Kennicutt, R. C., Gil de Paz, A., et al. 2011, in Highlights of Spanish Astrophysics VI, Proc. IX Scientific Meeting of the Spanish Astronomical Society (SEA), ed. M. R. Zapatero Osorio et al., 339

Sánchez, S. F., Kennicutt, R. C., Gil de Paz, A., et al. 2012, A&A, 538, A8

Schlafly, E. F., & Finkbeiner, D. P. 2011, ApJ, 737, 103

Schlafly, E. F., Finkbeiner, D. P., Jurić, M., et al. 2012, ApJ, 756, 158

Schlegel, D. J., Finkbeiner, D. P., & Davis, M. 1998, ApJ, 500, 525

Schneider, D. P., et al. 2010, AJ, 139, 2360

Schönrich, R., Aumer, M., & Sale, S. E. 2015, ApJL, 812, L21

Schultheis, M., Zasowski, G., Allende-Prieto, C., et al. 2014, AJ, 148, 24

SDSS Collaboration, Albareti, F. D., Allende Prieto, C., et al. 2016, arXiv:1608.02013

Sesar, B., Ivezić, Ž, Lupton, R. H., et al. 2007, AJ, 134, 2236

Shectman, S. A. 1993, in ASP Conf. Ser. 37, Fiber Optics in Astronomy II, ed. P. M. Gray (San Francisco, CA: ASP), 26

Shectman, S. A., Landy, S. D., Oemler, A., et al. 1996, ApJ, 470, 172

Shen, Y., Brandt, W. N., Dawson, K. S., et al. 2015, ApJS, 216, 4

Shetrone, M., Bizyaev, D., Lawler, J. E., et al. 2015, ApJS, 221, 24

Siegmund, W. A., Owen, R. E., Granderson, J., et al. 1998, in ASP Conf. Ser. 152, Fiber Optics in Astronomy III, ed. S. Arribas, E. Mediavilla, & F. Watson (San Francisco, CA: ASP), 92

Smee, S. A., Gunn, J. E., Uomoto, A., et al. 2013, AJ, 146, 32

Smith, R. M., Dekany, R. G., Bebek, C., et al. 2014, Proc. SPIE, 9147, 914779

Smith, V. V., Cunha, K., Shetrone, M. D., et al. 2013, ApJ, 765, 16

Sotiriou, T. P., & Faraoni, V. 2010, RvMP, 82, 451

Steidel, C. C., Erb, D. K., Shapley, A. E., et al. 2010, ApJ, 717, 289

Steinmetz, M., Zwitter, T., Siebert, A., et al. 2006, AJ, 132, 1645

Strauss, M. A., et al. 2002, AJ, 124, 1810

Szalay, A. S., Gray, J., Thakar, A. R., et al. 2002, arXiv:cs/0202013

Takada, M., Ellis, R. S., Chiba, M., et al. 2014, PASJ, 66, R1

Thomas, D., Maraston, C., & Bender, R. 2003, MNRAS, 339, 897

Tremonti, C. A., et al. 2004, ApJ, 613, 898

Troup, N. W., Nidever, D. L., De Lee, N., et al. 2016, AJ, 151, 85

Udalski, A., Szymanski, M. K., Soszynski, I., & Poleski, R. 2008, AcA, 58, 69

Udalski, A., Szymanski, M. K., & Szymański, G. 2015, AcA, 65, 1

Valdes, F., Gupta, R., Rose, J. A., Singh, H. P., & Bell, D. J. 2004, ApJS, 152, 251

Voges, W., Aschenbach, B., Boller, T., et al. 1999, A&A, 349, 389

Wands, D. 2010, CQGra, 27, 124002

Warwick, R. S., Saxton, R. D., & Read, A. M. 2012, A&A, 548, A99

Weaver, B. A., Blanton, M. R., Brinkmann, J., brownstein, J. R., & Stauffer, F. 2015, PASP, 127, 397

Weinberg, D. H., Mortonson, M. J., Eisenstein, D. J., et al. 2013, PhR, 530, 87

Wilson, J. C., Hearty, F., Skrutskie, M. F., et al. 2012, Proc. SPIE, 8446, 84460H

Worthey, G., Faber, S. M., Gonzalez, J. J., & Burstein, D. 1994, ApJS, 94, 687

Wright, E. L., Eisenhardt, P. R. M., Mainzer, A. K., et al. 2010, AJ, 140, 1868

Xue, Y. Q., Luo, B., Brandt, W. N., et al. 2011, ApJS, 195, 10

Yan, R., Tremonti, C., Bershady, M. A., et al. 2016, AJ, 151, 8

Yanny, B., Rockosi, C., Newberg, H. J., et al. 2009, AJ, 137, 4377

York, D. G., et al. 2000, AJ, 120, 1579

Zamora, O., García-Hernández, D. A., Allende Prieto, C., et al. 2015, AJ, 149, 181

Zasowski, G., Chojnowski, S. D., Whelan, D. G., et al. 2015a, ApJ, 811, 119

Zasowski, G., Johnson, J. A., Frinchaboy, P. M., et al. 2013, AJ, 146, 81

Zasowski, G., Majewski, S. R., Indebetouw, R., et al. 2009, ApJ, 707, 510

Zasowski, G., Ménard, B., Bizyaev, D., et al. 2015b, ApJ, 798, 35

Zhao, G., Zhao, Y.-H., Chu, Y.-Q., Jing, Y.-P., & Deng, L.-C. 2012, RAA, 12, 723

Zhao, G.-B., Wang, Y., Ross, A. J., et al. 2016, MNRAS, 457, 2377

Zheng, Z., Coil, A. L., & Zehavi, I. 2007, ApJ, 667, 760

Zhu, G., Ménard, B., Bizyaev, D., et al. 2014, MNRAS, 439, 3139

Zhu, G. B., Comparat, J., Kneib, J.-P., et al. 2015, ApJ, 815, 48

Zou, H., Jiang, Z., Zhou, X., et al. 2015, AJ, 150, 104

Zucker, D. B., de Silva, G., Freeman, K., Bland-Hawthorn, J., & Team, H. 2012, in ASP Conf. Ser. 458, Galactic Archaeology: Near-Field Cosmology and the Formation of the Milky Way, ed. W. Aoki et al. (San Francisco, CA: ASP), 421